2015

Shock wave induced freeform technique (SWIFT) for manufacturing of diamond micro-tools

Cheng Deng
Iowa State University

Shock wave induced freeform technique (SWIFT) for manufacturing of diamond micro-tools

by

Cheng Deng

A dissertation submitted to the graduate faculty

in partial fulfillment of the requirements for the degree of

DOCTOR OF PHILOSOPHY

Major: Mechanical Engineering

Program of Study Committee:
Xinwei Wang, Major Professor
Abhijit Chandra
Matthew Charles Frank
Shan Hu
Thomas J. Rudolphi

Iowa State University

Ames, Iowa

2015

DEDICATION

This thesis is dedicated to my family and everybody who cared about my development, without them I wouldn’t be here today. Thank you for your love, guidance, and support that you have always given me, helping me to succeed and instilling in me the confidence that I am capable of doing anything I put my mind to. Thank you both for always being there!

TABLE OF CONTENTS

LIST OF FIGURES

LIST OF TABLES

ACKNOWLEDGMENTS

I would like to take this opportunity to express my thanks to those who helped me with various aspects of conducting research and the writing of this thesis, first and foremost, Dr. Xinwei Wang and Dr. Pal. Molian for their guidance, patience and support throughout this research and the writing of this thesis. Their insights and words of encouragement have often inspired me and renewed my hopes for completing my graduate education.

I would also like to thank my committee members for their efforts and contributions to this work: Dr. Abhijit Chandra, Matthew Charles Frank, Shan Hu and Dr. Thomas J. Rudolphi.

Thank you to Larry Jones and Wyman Martinek for allowing me to use their facilities and providing assistance to produce and test my samples.

ABSTRACT

Diamond exhibits many attractive properties including extreme hardness, high thermal conductivity, high Young's modulus, low coefficient of friction, low wear rate, biocompatibility and chemical inertness the Institutional Repository. Therefore, diamond tools have attracted number of applications in manufacturing of various microdevices and ductile machining of brittle materials. However, just because of these special features, manufacturing of diamond tools is very complex, time consuming and high cost. Laser shock wave induced freeform technique (SWIFT) can be considered as an innovative technique for manufacturing of diamond microtools that employing laser induced shock waves to mechanically sinter nanodiamond powders. Laser shocks can impart desirable dislocation structures and compressive residual stresses into material to improve the relative density and generate residual stress to enhance the fatigue strength. In this work, multiscale models based on laser-material interaction, high pressure sintering of nanodiamond powders and interface effects are utilized to explore the physics underlying this technique. Finite element simulation is applied to analyze the mechanical deformations induced by laser shock wave sintering. Scanning electron microscopy, optical profilometery, raman spectroscopy and micro-indentation are employed to characterize the microstructure evolution, phase transition, and hardness improvement. Tool wear test is carried out to investigate the product final performance.

CHAPTER 1. GENERAL INTRODUCTION

1. Introduction

In recent years, diamond micro-tools are increasingly used in micro-end milling, micro-turning, micro-drilling of a variety of micro-devices such as micro-optics, comb structures, precision biomedical components, micro-propellers, micro-fluidic devices, micro-heat sinks, micro-heat exchangers, X-ray lithography masks, micro-channels for lab-on-chips, fuel cells, gas turbines and micro-molds [1-9]. Diamond is able to overcome several challenges when scaling down the cutting tools from conventional to microscopic sizes. High flexural stiffness, high strength and low friction of diamond enable to minimize bending; prevent catastrophic failure; and eliminate chip adherence of the small tools [4-9]. Diamond micro-tools meet the high demands of form accuracy, surface quality and low sub-surface damage in ductile machining of brittle materials [10]. All types of diamond - chemical vapor deposited (CVD), single crystalline and polycrystalline - are used for micro-tools although single crystalline diamond is preferred. The attractive properties of diamonds include extreme hardness, high thermal conductivity, high Young's Modulus, low coefficient of friction, low wear rate, biocompatibility and chemical inertness. Microcrystalline CVD diamond (MCD) is used in the form of coating [11-19], however, the MCD is too thick (>2 μm) and possess rough texture thus creating the problem of blunting the micro-tools which have a typical edge radius of ~1.5 μm. In addition, MCD has inferior strength [20] and much higher friction [21] than nano-crystalline diamond (NCD). Thus, there is a push towards moving from MCD to NCD for micro-end mills [22]. Despite such exciting developments in CVD diamond, micro-tools from bulk diamonds are mostly preferred by the industry.

Historically diamond micro-tools are fabricated by polishing and grinding of natural diamonds on a rotating metal disc covered with a fluid containing small diamond particles; however this process has shortcomings such as long duration, labor intensive, lack of reproducibility and limited shape fabrication. Diamond polishing and hot iron oxidation have been attempted [23, 24] but are severely limited by the low material removal rates (MRR). Consequently many new processes have emerged including laser, micro-electrical discharge machining (EDM), focused ion beam and lithography [25-39]. Although lasers have excellent prospects for micromachining diamond, the central issues are phase transition of diamond to graphite and low MRR. It appears that the femtosecond laser, the best laser source available for diamond ablation, is well suited for finishing rather than machining. Non-contact μEDM has been used to fabricate micro-end mills and drills with sharp protrusions around 1 μm in polycrystalline diamonds [33, 34]; such tools were then used to carve out grooves in soda-lime glass and pockets in ultra-low expansion glass. However the MRR in μEDM remained low. A hybrid process using EDM combined with electrodeposition of Ni-diamond composites improved the MRR [35]. Focused-ion beam (FIB) was an effective tool for the fabrication of micro-tools although it also suffers from low MRR [36-38]. Advantages of FIB are complex shapes, high feature resolution, maskless processing, rapid prototyping, and adaptability to various materials and geometries. Finally, photolithography techniques were presented for diamond micro-milling tools based on CVD-diamond film on silicon substrate with high contour accuracy, reproducibility and unlimited shape [39].

Different from the above described competing subtractive methods, the manufacturing cost for diamond micro-tool by synthesis of nano size diamond particles and

powders is expected to be lower due to 1) the additive process would be materials savings and less requirements of tooling and 2) nanodiamond (ND) is inexpensive compared to bulk diamond in large size. For example, ND sells at typical cost of several dollars per gram (Nanodiamond.com) and 1mm layer requires only 0.3 grams per square centimeter. However, there are still no effective ways to manufacture ND tools by powder sintering. Rather than traditional sintering and manufacturing of ND tools from powders under high temperature and high pressure, laser shock wave induced freeform technique (SWIFT) can be considered as an innovative and viable one. This novel SWIFT process employs laser-induced shock waves to mechanically sinter ND powders through layer-by-layer additive manufacturing. Laser shocks can impart desirable dislocation structures and compressive residual stresses into metals through compression to improve fatigue strength and hardness [40]. By laser shocking, the peak pressure can reach as high as several gigapascals; under such conditions and due to large surface area of nanoparticles, the nanodiamond powders can be compacted without a need for high temperatures.

2. Literature Review

Here nanodiamond and its special properties are introduced, physics and basic mechanisms of laser shock wave sintering process are mentioned as well in brief.

It is well known that nanocrystalline CVD diamond offers improved surface finish, lower friction, higher wear and abrasion resistance and fewer tendencies for cracking over their micro-crystalline counterparts [20-22]. Similar results can be expected from nanodiamond powders. In addition, sintering of nanoscale powders requires much lower energies than microscale powders. Nanodiamond (ND), also called nanocrystalline diamond

(NCD) powder, or ultra-dispersed diamond (UDD) having a particle size range of 2-20 nm, is considered a promising material for various applications, including abrasives for the semiconductor and optical industries, durable and hard coatings, additives to lubricants for engines and moving gears, polymer reinforcements, protein adsorbents, and even medicinal drugs. ND powders are mass produced by the detonation of explosives (e.g. TNT and RDX mixture) in a closed chamber during less than a microsecond when both pressure and temperature are high, i.e. over 20 GPa and 3000°C. ND powders with different grades and varying purity have been commercially available in Russia and Ukraine (sinta1@yandex.ru) for over 10 years. ND particles exhibit a very narrow size distribution, i.e. from about 4 nm to about 8 nm. Moreover, these nanodiamonds contain carbon onions, bucky balls (C60), layered shells and amorphous carbon [41-46]. ND has superior properties over single and polycrystalline diamonds due to its large surface area-to-volume ratio and unique electronic structure. Unlike single crystalline diamond, ND is extremely hard without sharp corners. Because carbon atoms are very small, any given surface area of a ND particle can include many more atoms than other nanoparticles of the same size. As a result, ND particles can readily bond to and effectively absorb a variety of species. In fact, ND particles are hydrophilic and functionalized with several groups.

Among various solid freeform fabrication processes, selective laser sintering (SLS) of powder materials is a dominant process to produce direct tooling. In SLS, a laser beam is used to thermally sinter microscale powder in layer-by-layer fashion to produce three-dimensional parts directly from a computer aided design (CAD) model. Laser micro-sintering (LMS) is a scaled down version of SLS that has been developed by two research groups to produce high resolution functional micro-parts with hollow profiles and undercuts [47-50].

The first group used essentially sub-micrometer powders of metals and ceramics, a cylindrical coating blade and a Q-switched solid-state laser in LMS to improve the resolution and surface roughness of micro-parts by more than an order of magnitude than those achieved by SLS [47-49]. The second group used an ultrasonic device to deposit micron powder particles to form thin pattern on the substrate and then sintered selectively by a micro-sized fiber laser beam [50]. According to this group, the main differences between SLS and LMS are the powder feeding method and type of laser system.

High power pulsed lasers (above 1GW/cm^2) are the best among the shock generators to induce high amplitude pressures in extremely short time (Fig.1.1). A thin layer of sacrificial material (paint, Al foil etc.) with low heat of vaporization is necessary for the generation of high-amplitude stress waves (Fig.1.2). In addition, a transparent overlay is required to confine the shock waves. Essentially, the plasma formed from the laser ablation of sacrificial material is trapped between the specimen and overlay and then expanded upon further laser energy absorption, leading to extreme pressure waves propagating through the specimen. The presence of overlay increases the ablation pressure by a factor 5 to 10 and an increase of shock duration by a factor of 2 to 3 compared to direct ablation [51]. However, the pressure may saturate above a threshold power density depending on the overlay medium, wavelength and pulse width [52]. The applications of laser shock waves are primarily in cleaning, hardening (to improve fatigue strength), sheet metal bending and changing the surface microstructure and stress state and morphology of materials and parts [52-54]. For example, Yao's group reported microscale effects of laser shock waves to obtain the desired residual stress patterns in micro-components such as MEMS micro-gears [55, 56]. Laser

shock wave is less cumbersome and much safer than explosive shock processing that uses dangerous explosives and plate acceleration to consolidate the powders.

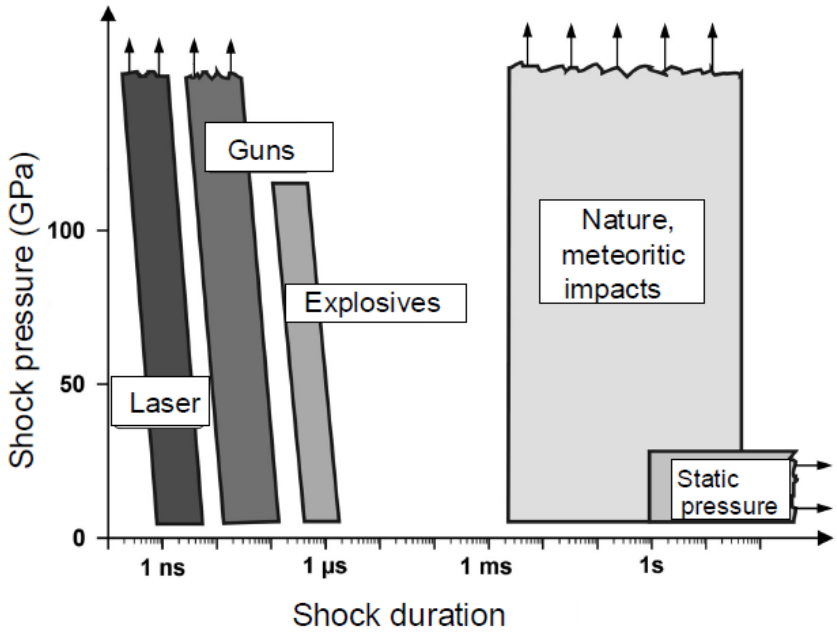

Figure 1.1. Shock generators

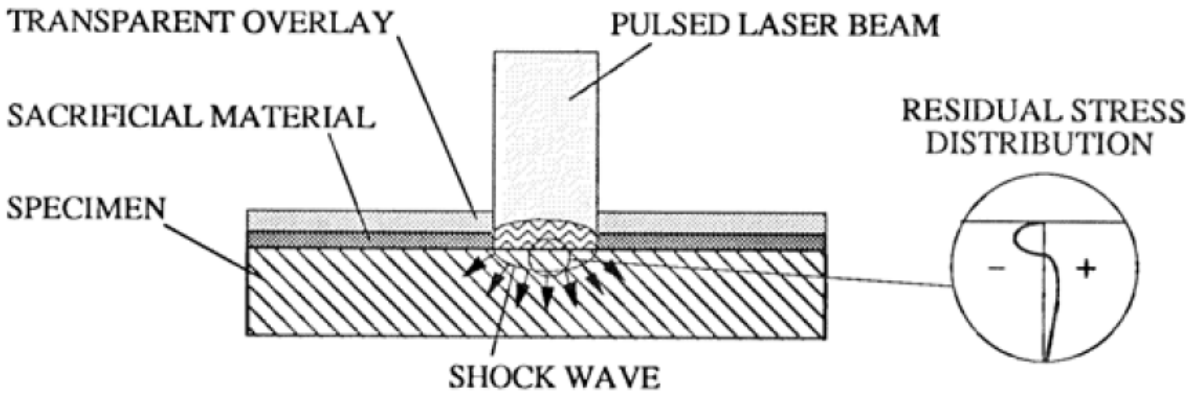

Figure 1.2 Schematic of generation of laser shock waves

3. Motivation and Proposed work

The motivation for the proposed work stems from the current and future demands for high-performance diamond micro-tools in the area of micro/nanomachining of optics, MEMS

and medical devices such as microscale probes and surgical tools. The proposed laser shock wave induced freeform technique (SWIFT) has strong potential to transform the way diamond microtools are currently fabricated and can make quantum leap advances in the state-of-the art microscale solid freeform fabrication process. Additive SWIFT will outperform the existing subtractive processes including diamond polishing, microEDM, focused ion-beam, femtosecond laser and hot iron oxidation which are used to produce both single and polycrystalline diamond microtools but are inherently limited by the low material removal rates and high cost of synthetic diamonds. The proposed SWIFT uses nanodiamond (4-8 nm) with low cost and novel properties which are comparable to or better than synthetic diamonds. On the science front, this multi-scale modeling will provide an improved fundamental understanding of laser shock waves to bind nanoparticles and cause phase transition. On the technology front, the SWIFT innovations will offer simplicity and robustness for layer sintering of nanodiamond at room temperature.

The following tasks are proposed to achieve the specified objectives:

1. Develop multiscale models and conduct systematic simulation of laser-material interaction, shockwave sintering, phase transition and interface effects in layer-by-layer buildup of detonation nanodiamonds to understand the working principles of SWIFT.

2. Conduct laser shock wave sintering of nanodiamond powders to produce 3D microtools in various geometries such as square, triangle and rhombus in freeform. The simulation results are expected to provide the crucial knowledge base for fabrication optimization in terms of throughput and quality.

3. Characterize the structure and properties of the layers through Raman spectroscopy, scanning electron microscopy and micro/nanoindentation tests. The structure data will be compared with the multi-scale modeling to validate and refine the multi-physics model.

4. Benchmark the SWIFT tools with other manufacturing produced good performance diamond tools or carbide tools.

4. Thesis Organization

The remainder of the thesis is divided into seven chapters. In chapter two, preliminary experimental work that laser shock wave treatment of polycrystalline diamond (PCD) materials was investigated, also additive manufacturing of nanodiamond powder compact via laser shock wave sintering was explored. In chapter three, subtractive manufacturing process that coated nanodiamond powders in polycrystalline cubic boron nitride (PcBN) through laser shock wave sintering (LSS) was systematically investigated. In chapter four, finite element simulation (FEM) was applied to explore the physics and mechanicsm of LSS. In chapter five, tool wear test was employed to examine the final product performance. In chapter six, summary and disscusion were presented. In final chapter seven, future work was introduced.

CHAPTER 2. LASER SHOCK WAVE TREATMENT OF POLYCRYSTALLINE DIAMOND TOOL AND NANO-DIAMOND POWDER COMPACT

A paper published in International Journal of Advanced Manufacturing Technology

Cheng Deng[1,2] and Pal Molian[1,3]

Abstract

Laser shock processing (LSP) of polycrystalline diamond (PCD) tools and nanodiamond powder compacts was conducted using a 1064 nm Q-switched Nd:YAG laser at peak power densities in the range of 4 to 18 GW/cm^2 and pulse repetition rates of 1 to 10 Hz. The PCD tools were directly procured from the tool manufacturer while ND powder compacts were prepared in the laboratory by cold die press forming and annealing using a powder mixture of nanodiamond, 8 wt% cobalt, and 10 wt% agar-agar as the binder. The samples were characterized by Raman spectroscopy, scanning electron microscopy, micro-indentation and optical profilometer. Results indicate that LSP induced diamond purification, inhomogeneity of phases in PCD, densification in nanodiamond compact, phase transition to various amounts of sp^3 and sp^2 carbon forms, and an increase in hardness and surface roughness.

1. Introduction

In recent years, diamond tools are increasingly used in manufacturing of various micro-devices as well as in ductile machining of brittle materials. For example, the rapidly

---

[1]Graduate student and Professor, respectively,
Department of Mechanical Engineering, Iowa State University.
[2]Primary researcher and author.
[3]Author for correspondence

growing micro-end milling is a beneficiary of diamond tools with applications in the production of precision biomedical components, micro-propellers, micro-fluidic devices, micro-heat sinks, micro-heat exchangers and X-ray lithography masks. Single crystalline and polycrystalline diamonds (PCD) as well as chemical vapor deposited (CVD) diamonds are used due to diamond's attractive properties that include extreme hardness, superior abrasion resistance, high thermal conductivity, high Young's Modulus, low coefficient of friction, and chemical inertness [1,57-59]. Such properties of diamond enabled to minimize bending, catastrophic failure and chip adherence of the tools as well as meet the high demands of form accuracy, surface quality and low subsurface damage of workpiece.

There is a huge interest in using nano-crystalline CVD diamond for tools as it offers improved surface finish, lower friction, higher wear and abrasion resistance and fewer tendencies for cracking over their micro-crystalline counterparts [20-22]. Similar results can be expected from the tools made by sintering nanodiamond powders. Nanodiamond, also called nano-crystalline diamond powder, or ultra-dispersed diamond having a particle size range of 2-20 nm, is considered as a promising material for various applications, including abrasives for the semiconductor and optical industries, durable and hard coatings, additives to lubricants for engines and moving gears, polymer reinforcements, protein adsorbents, and even medicinal drugs.

PCD tools have exceptional tool life. Composed of interlocking fine grains, PCD can be considered as an extremely tough composite material formed by sintering diamond particles into a metal matrix (typically cobalt) under high-temperature and high-pressure [60]. Fine grain diamond (<5 μm) tools are used to produce a fine surface finish on softer materials such as pure metals, wood composites, and plastics; medium grain diamond (5-10

μm) tools are effective in general purpose machining; and coarse grain diamond (20-25 μm) tools are accepted for rough machining of extremely hard abrasive materials such as aluminum alloys, sintered ceramic, and carbides. The metal matrix, along with randomly orientated diamond particles, greatly aids in improving the toughness of PCD.

Unlike PCD, nanodiamond tools are not yet produced from powders due to the difficulties involved in sintering. For example, sintering performed for 3 min at 4.5–7 GPa of quasi-hydrostatic pressure at 1400^{o}C resulted in a porous structure that can be used only as a fine abrasive powder [45]. Similarly a plasma pressure compaction technique used to sinter nanodiamond for 1 min at temperatures between 700 and 1200°C, and for 1–10 min at 900°C under 65 MPa pressure resulted in 50% porous pellets [43]. Even if nanodiamond sintering would have been successful, it is still difficult to fabricate specific tool shapes by machining due to their unique properties such as extreme hardness.

In this paper, we report a laser shock wave method of sintering the nanodiamond powder compacts for use as tools and understand the strengthening behavior of existing PCD tools. We consider LSP as an innovative and effective process for producing nanodiamond tools. LSP is a new and promising surface treatment technique for strengthening materials [3,40]; it has been shown to be effective in improving the fatigue properties of a number of metals and alloys because of its capability to impart desirable dislocation structures and residual stress distributions through compression [40]. Under such pressures as high as 5 GPa during LSP, nandiamond powder compacts can be sintered in cold condition. Similarly polycrystalline diamond tools can be purified by partial phase transition from diamond-like amorphous carbon to diamond, and the dislocation density can be increased with increasing laser shock repetitions. Thus, the material properties such as hardness can be improved. High

performance and cost-effective diamond micro-tools can be achieved by employing laser-induced shock waves to mechanically sinter nandiamond compacts.

A systematic experimental study on LSP was undertaken to examine the effect of power density and pulse repetition rate on nandiamond compacts and PCD tools. Phase transition and hardness improvement were studied by Raman spectroscopy and micro-indentation respectively. Microstructure modification and surface roughness were also studied by scanning electron microscopy and optical profilometery respectively.

2. Experimental methods

Materials: PCD tools were received from Diamond Innovations, Inc (Ohio) in the free-standing form with a thickness of 0.5 mm, grain size of 5 μm and cobalt binder of 10 wt%. Nandiamond powders were procured from Ukraine (sinta1@yandex.ru) which are mass produced by the detonation of explosives (e.g. TNT and RDX mixture) in a closed chamber during less than a microsecond when both pressure and temperature are high, i.e. over 20 GPa and 3000°C. Nano-diamond particles exhibited a very narrow size distribution, i.e. from about 4 nm to about 8 nm. Moreover, these nandiamond contained carbon onions, bucky balls (C60), layered shells, amorphous carbon and metallic impurities for a total of less than 10 wt%. It may be noted that nandiamond has superior properties than single and polycrystalline diamonds due to its large surface area-to-volume ratio and unique electronic structure. Unlike single crystalline diamond, nandiamond is extremely hard without sharp corners.

Preparation of Nano-diamond Powder Compact Nanodiamond powders were uniformly mixed with 8 wt% cobalt and 10 wt% agar-agar (binder) and then subjected to a

cold pressing operation using tungsten carbide die at a pressure of 350 MPa. A disk with diameter of 12 mm and thickness of 2 mm was prepared and heated to 400℃ for 1 hour; agar-agar became liquid and infiltrated in the powder compacts to form an effective binder for nano-diamond powders.

Laser Shock Wave Experiments A schematic configuration of laser shock wave development is depicted in Fig.2.1. A Q-switched Nd:YAG laser at a wavelength of 1064 nm (near infrared, IR) and pulse width of 10 ns was employed. The sample (PCD tool or nandiamond powder compact) surface was sprayed with black paint as an absorptive layer, and covered by 1 mm thick fused quartz as a transparent overlay. The sample was then mounted on an X-Y positioning table and moved at a speed of 0.6 mm/sec with an overlap of 25 % to cover the whole surface.

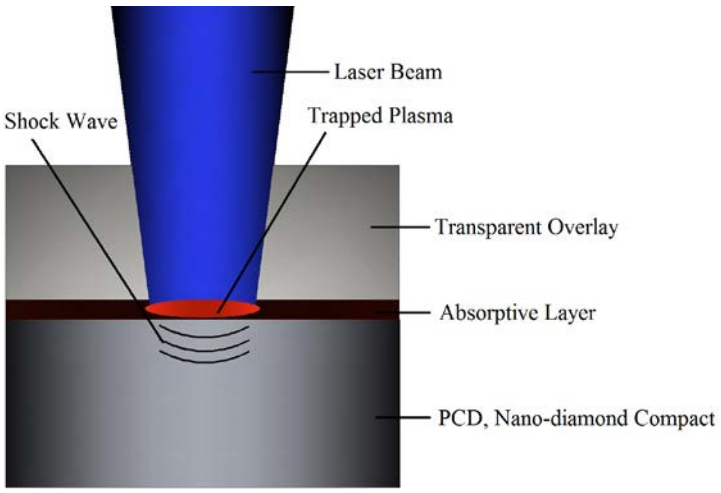

Figure 2.1 Schematic of laser shock peening

For LSP of PCD, the laser beam was defocused to a spot size of approximately 0.6 mm in diameter on the target sample while the pulse repetition rates were 1 Hz, 5 Hz and 10Hz corresponding to the average power of 0.5 W, 1.8 W and 4.0 W respectively. The pulse energy, E, is established as a function of average power, P_a and repetition rate, R, using:

$$E = \frac{P_a}{R}$$

The peak power density is calculated as a function of pulse energy, *E*, pulse width, *t*, and beam area *A*, using:

$$I_P = \frac{E/t}{A}$$

The calculated peak power densities were 17.69 GW/cm^2 at 1 Hz, 12.74 GW/cm^2 at 5 Hz and 14.15 GW/cm^2 at 10 Hz.

For LSP of nano-diamond compact, a defocused beam with a spot size of 1 mm was used, because the 0.6 mm spot size resulted in fracture. The associated peak power densities were 6.37 GW/cm^2 at 1 Hz and 4.59 GW/cm^2 at 5 Hz.

Test and Characterization: A Tukon microhardness tester was used to measure the Vicker's hardness using a diamond pyramid indenter at 1 kgf load and 10 s hold time. Phase transitions were identified using a Raman visible spectroscope (532 nm using Ar-ion laser) for Raman shift range of 900 to 1800 cm^{-1}. Surfaces roughness was measured using the Zygo New View 5000 series optical profilometer with ×20 objective. Microstructure was examined by scanning electron microscopy (JEOL JSM-606LV).

3. Results and discussion

3.1 Phase transition

Fig.2.2 shows the Raman spectra of as-received and laser-shocked PCD. It is seen that the as-received PCD exhibits a distorted curve with two small peaks around 1340 cm^{-1} and 1596 cm^{-1}; these are attributed to diamond-like sp^3 bonded and polycrystalline graphite-like sp^2 bonded crystals respectively [61-63]. Hence, the diamond quality of the as-received PCD is very poor. Shock waves developed at different peak power densities had, however, significant effects in the first order phonon bands from 1000 to 1800 cm^{-1}. For the PCD samples subjected to LSP with the peak power density of 12.74 GW/cm^2 at 5 Hz and 14.15 GW/cm^2 at 10 Hz, two Gaussian curves with peaks centered at 1360 cm^{-1} and 1596 cm^{-1} can be seen. These are denoted respectively as D (disordered carbon) and G (graphite) bands in the literature, The broad peak at 1360 cm^{-1} is assigned to disordered graphite, while that at 1596 cm^{-1} is assigned to polycrystalline graphite. The 1360 cm^{-1} is attributed to the disruption of the long-range order of the graphite lattice. The line-width can be used as a measure of the disorder and stress in the film. The ratio of the intensity of these two peaks indicates almost equal amounts of sp^3 and sp^2 carbon. For the sample shocked with a laser power density of 17.69 GW/cm^2 at 1 Hz, again two Gaussian curves with peaks centered at 1348 cm^{-1} and 1596 cm^{-1} are noted. The 1348 cm^{-1} is assigned to diamond-like sp^3 component. It is interesting to note that there was no shift in the peak of polycrystalline graphite (around 1596 cm^{-1}) with increase in peak power density. Raman analysis thus infers that shock waves caused the PCD for higher quality (through possibly by purification) and phase transition from diamond-like carbon to graphite and disordered carbon with varying sp^2 and sp^3 fractions.

In Fig.2.3, the Raman spectra of LSP processed nandiamond compacts at two different power densities are displayed. When compared with the PCD, the ND shows an additional strong sharp peak at 466 cm^{-1}. According to Prawer et al [64], strong relatively sharp peaks are observed in the Raman spectrum of nano-crystalline diamond around 500, 1330 and 1600 cm^{-1}. While lower power density LSP enabled to retain nandiamond structure, higher power density LSP caused some phase transition to diamond-like carbon at 1340 cm^{-1} (Fig. 2.3).

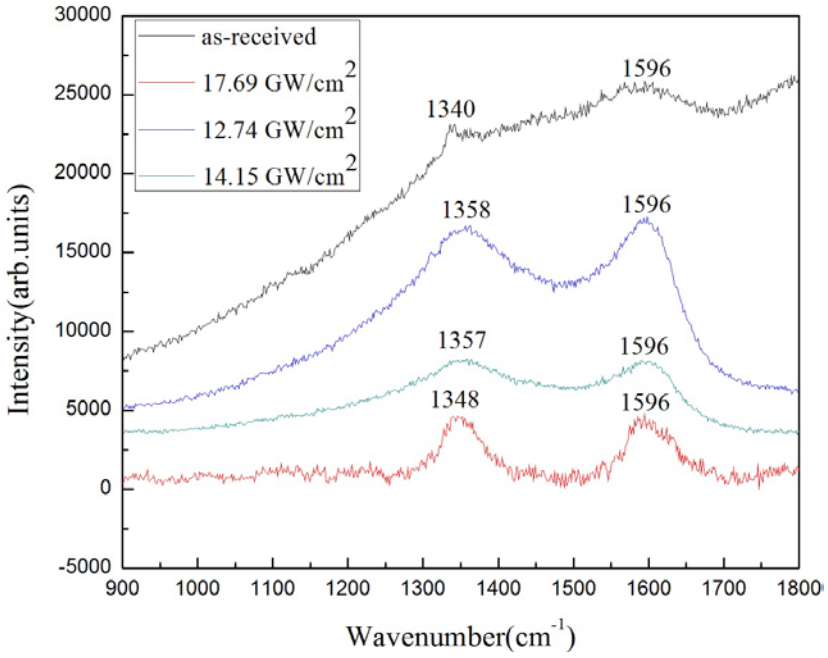

Figure 2.2 Raman spectra of as-received and LSP processed PCD

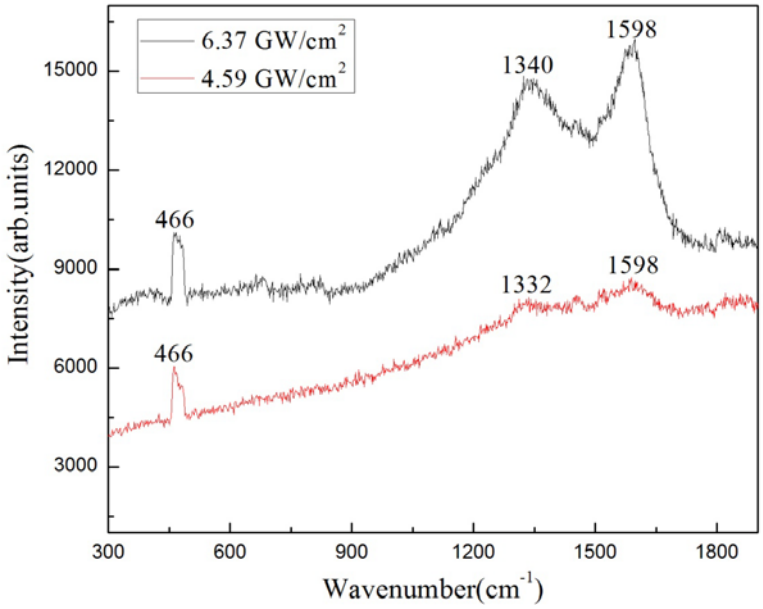

Figure 2.3 Raman spectra of LSP processed nanodiamond compact

3.2 Modeling of stresses and strains

An analytical model for LSP was utilized to predict the shock wave pressure and its effects on the extent of plastic deformation [65, 66]. In the model formulation, it is assumed that laser irradiation is uniform and shock wave propagation in the confining medium is one-dimensional. During LSP, the black paint is vaporized and transformed into plasma by ionization leading to two types of plasma: freely expanding plasma above the overlay and confined plasma below the overlay [65]. Considering the propagation of confined plasma below the transparent overlay, Fabbro's model [66] may be used to calculate the peak shock pressure, P in GPa:

$$P=0.01[\alpha/(2\alpha+3)]^{1/2}Z^{1/2}I_0^{1/2} \quad (2.1)$$

Where α is the efficiency of the interaction ≈0.1 [66, 67] and Z is the combined shock impedance of solid target and glass (gm/cm^{2}sec) ($2/Z=1/Z_1+1/Z_2$) and I_o is the laser intensity in GW/cm^2. Z is calculated as 13.69×10^4 g/cm^{2}s for glass/diamond interface using the data

from the reference [68]. Thus, P is computed as in the range of 2.83 to 4.24 GPa for laser intensities in the range of 4.5 to 10 GW/cm^2 used in this work.

For power densities greater than 10 GW/cm^2, equation (1) is not applicable because, according to Berthe et al., when the laser power density exceeded 10 GW/cm^2, the corresponding shock wave pressure is saturated; this is attributed to the breakdown of transparent overlay [69, 70]. The calculated pressure is well within the limits observed by others [71, 72].

Surface plastic strain must be evaluated to obtain the compressive residual stresses. The plastic strain depends on the peak shock pressure and its propagation through the depth. On the surface of the material, ignoring work hardening and viscous effects, the plastic strain (ε_P), depends only on the magnitude of the peak shock pressure as given by:

$$\varepsilon_P=[(-2HEL)/(3\lambda+2\mu)](P/HEL-1) \quad (2.2)$$

Where *HEL* is the Hugoniot elastic limit, *P* is the peak shock pressure; λ and μ are the Lamé's constants. Because the duration time of pressure is short (same as pulse width), the strain rate effect on the order of 10^6 per second is becoming important and affects HEL. The axial stress required for plastic deformation under uniaxial strain conditions is given by HEL:

$$HEL=[(1-v)/(1-2v)]\sigma_Y^{dyn} \quad (2.3)$$

Where v is Poisson's ratio (0.2) and σ_Y^{dyn} is the dynamic yield strength of diamond at a high strain rate (assumed to be 1 GPa at about 10^6 s^{-1}) [73]. Thus, HEL is found to be 1.33 GPa. The Lamé's constants are given by:

$$\mu=E/[2(1+v)] \quad (2.4)$$

$$\lambda=Ev/[(1+v)(1-2v)] \quad (2.5)$$

Where E is Young's modulus =1220 GPa [70]. Since the powder compact contains porosity of about 40%, the Young's modulus was adjusted to 732 GPa using the rule of mixture as 0.6 E_{Bulk}. Thus μ and λ are 305 GPa and 203 GPa respectively.

Obviously the peak shock pressure exceeds the dynamic yield strength of diamond which means diamond yields and expands in a predictable manner. Stress waves transmitted through an elastic-plastic material can be separated into two distinct waves: an elastic wave with a magnitude of HEL and a plastic wave with a magnitude greater than HEL [65]. Substitution of equations (2.3) to (2.5) in equation (2.2) yielded a surface plastic strain of approximately in the range of 0.02 to 0.03. Model results agree with the hypothesis that laser shock waves create a compressive stress pattern that causes plastic deformation of the particles.

3.3 Microstructure

The large plastic deformation and phase transition had significant influence on the resulting microstructures of LSP samples. Microstructural features of as-received and LSP processed PCD are shown in the SEM images of Fig.2.4. The as-received PCD showed very uniform microstructures with diamond grains and Co-binder and absence of craters or any other obvious defects (Fig. 2.4a and b). In contrast, LSP samples shocked at 1 and 5 pulse/sec exhibited craters and inhomogeneous distribution of phases in the composite matrix (Fig. 2.4 c-f). These craters and inhomogeneity can be explained by the partial heating and evaporation of carbon from PCD by laser ablation [74]. In addition, very huge territorial plastic deformation and phase transition induced by LSP are seen in Fig. 2.4c and d, with no change in the surrounding zone; such features are attributed to the dislocation movement and phase transition.

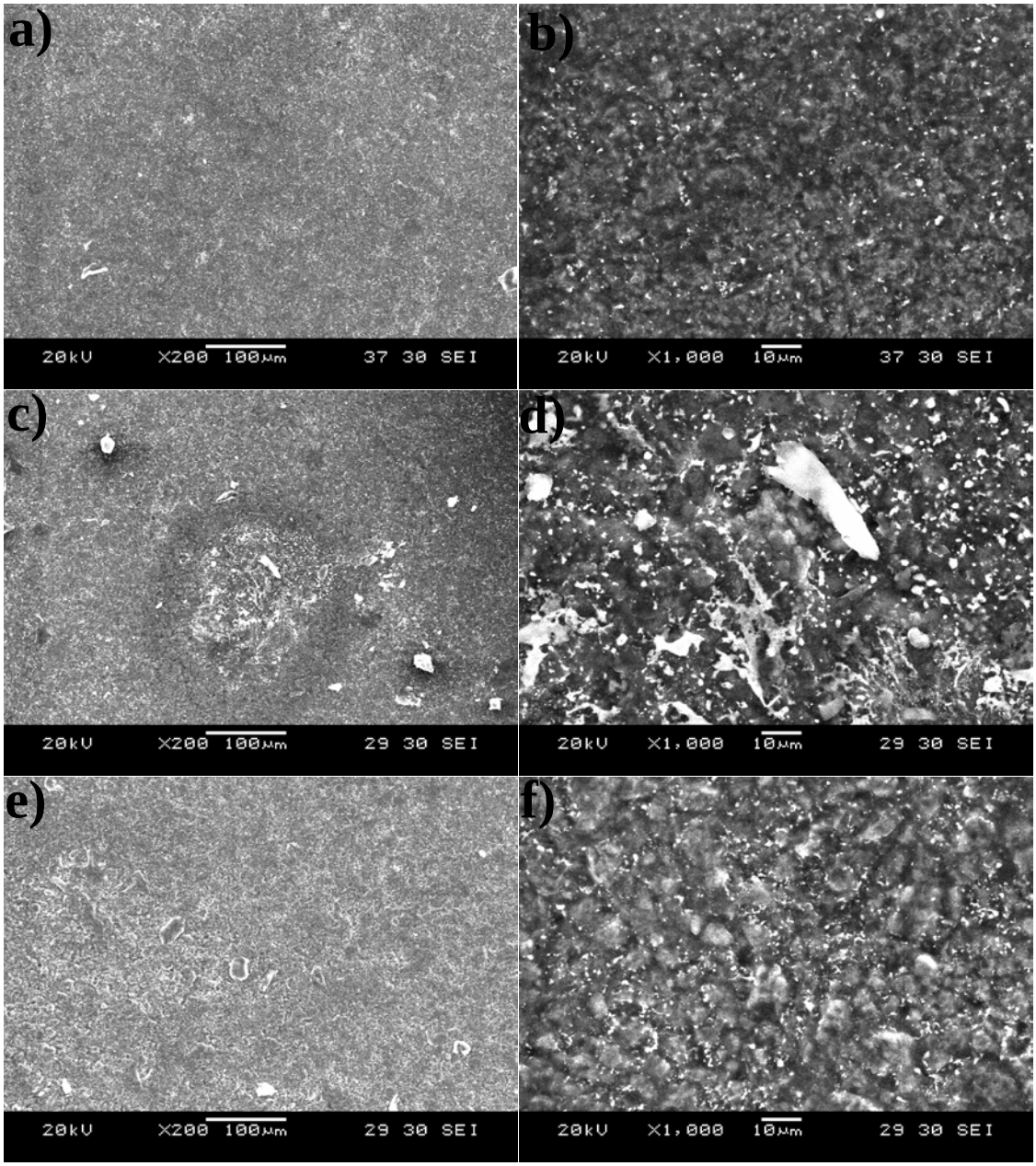

Figure 2.4 SEM images of as-received and LSP processed PCD. Experimental conditions are: (a) and (b) as-received PCD; (c) and (d) laser shocked at single pulse/sec; (e) and (f) laser shocked at 5 pulse/sec

Figure 2.5 shows the microstructural features of nandiamond powder compacts with and without LSP processing. The green compact fabricated by cold die press and subsequent heating is composed of many pores and very inhomogeneous distribution of phases (Fig.2.5a, c, and e). Also some loose particles were interspersed on the surface, as shown in Fig.2.5c.

However upon LSP, the microstructure is consolidated, more tight and well-densified with deformation lines, as shown in Fig.2.5b, d and f. Yushin et al [45] reported that furnace sintering of nandiamond powder compact resulted in an increase in the average size of diamond grains and noticeable broadening of the grain size distribution.

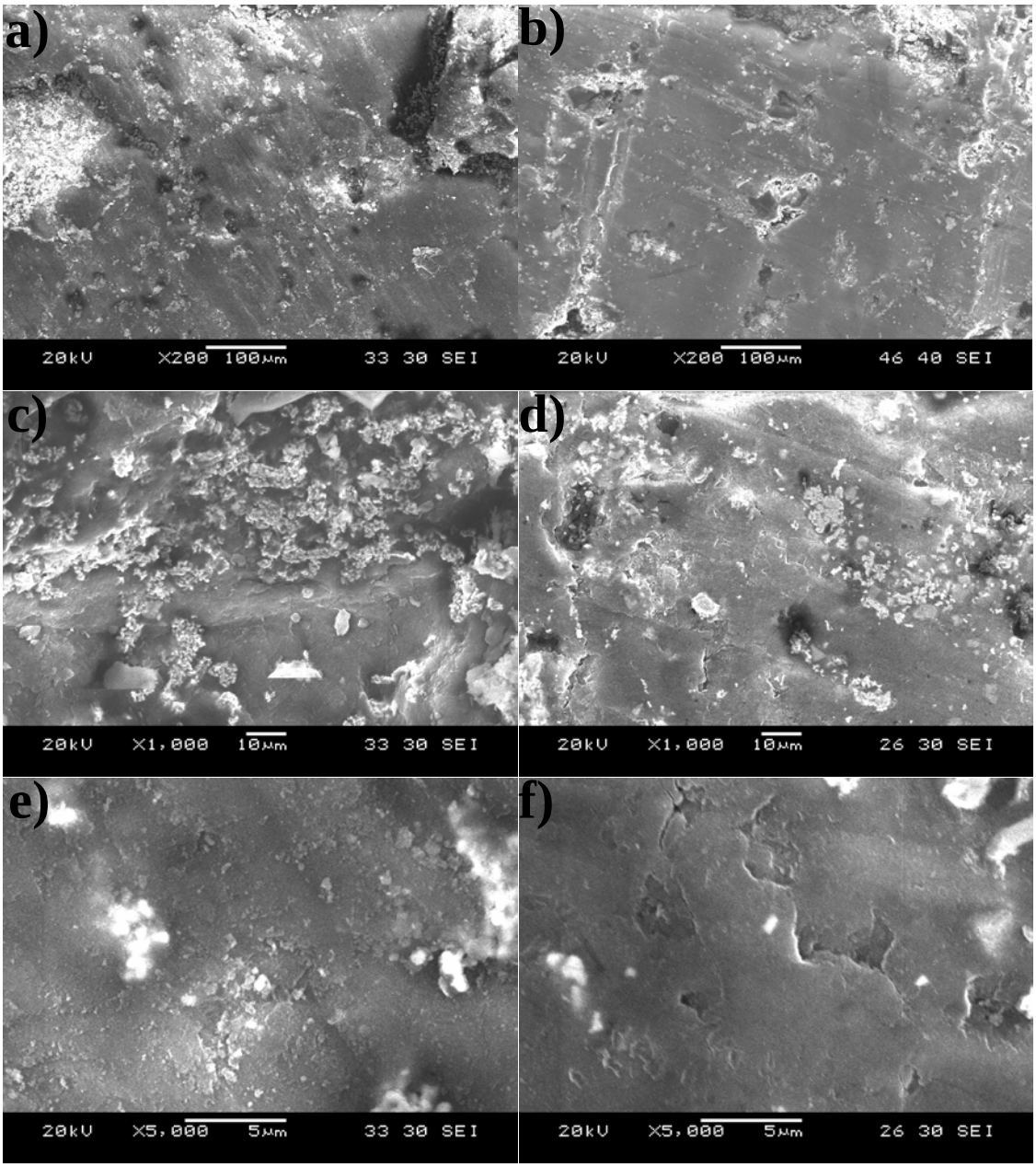

Figure 2.5 SEM images of nanodiamond compact. Experimental conditions are: (a), (c) and (e) no laser shocking; (b), (d) and (f) laser shocked at 5 pulse/sec

3.4 Hardness

The micro-hardness test results of PCD with and without laser shock wave treatment are shown in Fig. 2.6. It was observed that hardness processed by LSP was increased from 75 GPa to 90 GPa. It appears that pulse repetition rate is more sensitive than peak power density; this could be attributed to multiple shots at a given spot creating diamond phase purification as well as an increase in dislocation density. Laser shok waves induce more sp^3 component resulting more covalent bonds and thereby incraese the hardness. According to Murr [75], the dislocation density depends strongly on the peak pressure while their arrangement and displacements are mainly functions of pulse duration. In addition, we believe an increase in laser shock repetition will increase the dislocation density and thereby much higher hardness.

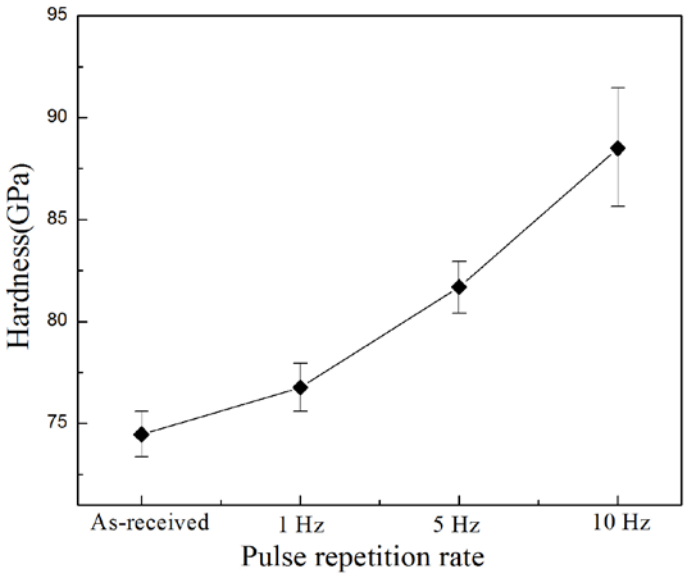

Figure 2.6 Hardness results of PCD with and without laser shocking

The hardness of nanodiamond compacts prepared by cold die press and heating (without laser shock wave sintering) was only 4.87 GPa due to the presence of substntial amount of porosity. After laser shock wave sintering, the hardness was increased to 6.45

GPa; this is attributed to densification, strucutural modification, increase of dislocation density and diamond phase purification (removal of impurities such as carbon onion, functional groups and bulky balls). Hardness similar to that of PCD can only be obtained with decreased pores and improved density. Multiple pulse repetition, structural purification and homogeneous distribution of nano-diamond and cobalt induced by particle reheating, welding and aggregation are essential to obtain the highest possible hardness. Osswald et al [43] sintered nano-diamond powders for 1 min at temperatures between 700 and 1200°C, and for 1–10 min at 900°C under 65 MPa pressure and produced 50% porous pellets having a hardness of 0.1 -0.2 GPa.

3.5 Surface roughness

The surface roughness (Ra) of PCD samples increases with an increase in pulse repetition rate, as shown in Fig.2.7. The reason for the increase is explained by the ablation of material and crater formation (Fig.2.8). Multiple pulses tend to enhance the ablation rate. However, the surface profiliometer traces, shown in Fig.2.9, indicate that the surface roughness parameters Ra and RMS behave differently than the peak-to-valley (P-V) distance. It appears that while Ra and RMS are dependent on pulse repetition rate, the P-V distance (measure of ablation depth) is controlled by the peak power density.

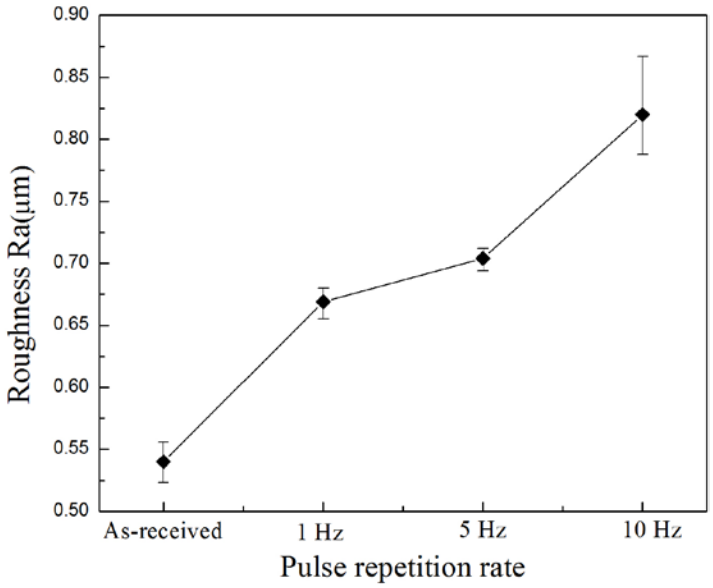

Figure 2.7 Surface roughness results of PCD with and without laser shocking

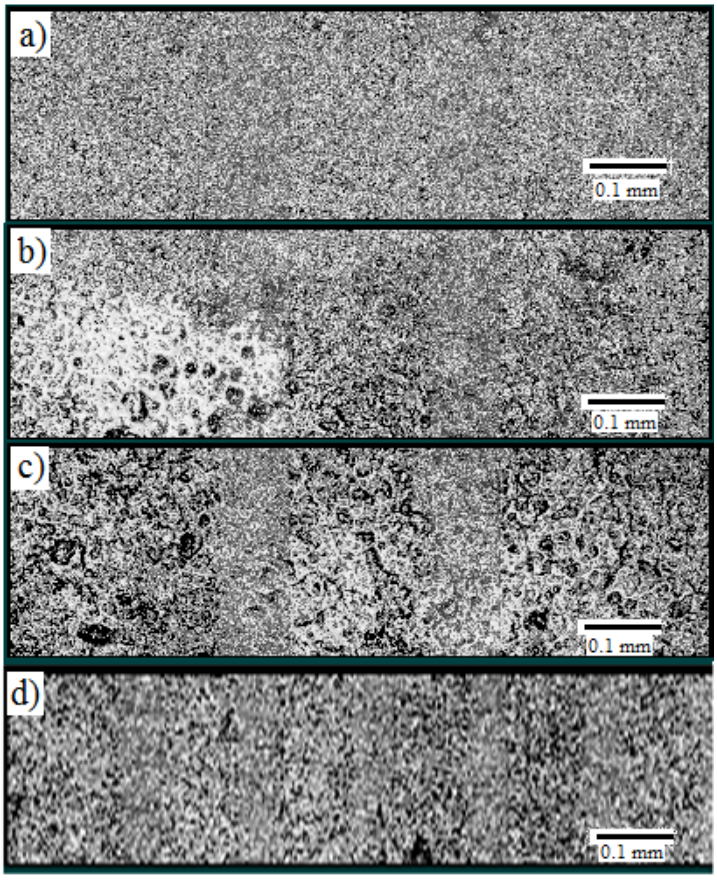

Figure 2.8 Optical images of PCD sample surfaces with and without LSP. Experimental conditions are: (a) as-received PCD; (b) LSP at single pulse/sec; (c) LSP at 5 pulse/sec and (d) LSP at 10 pulse/sec

a)

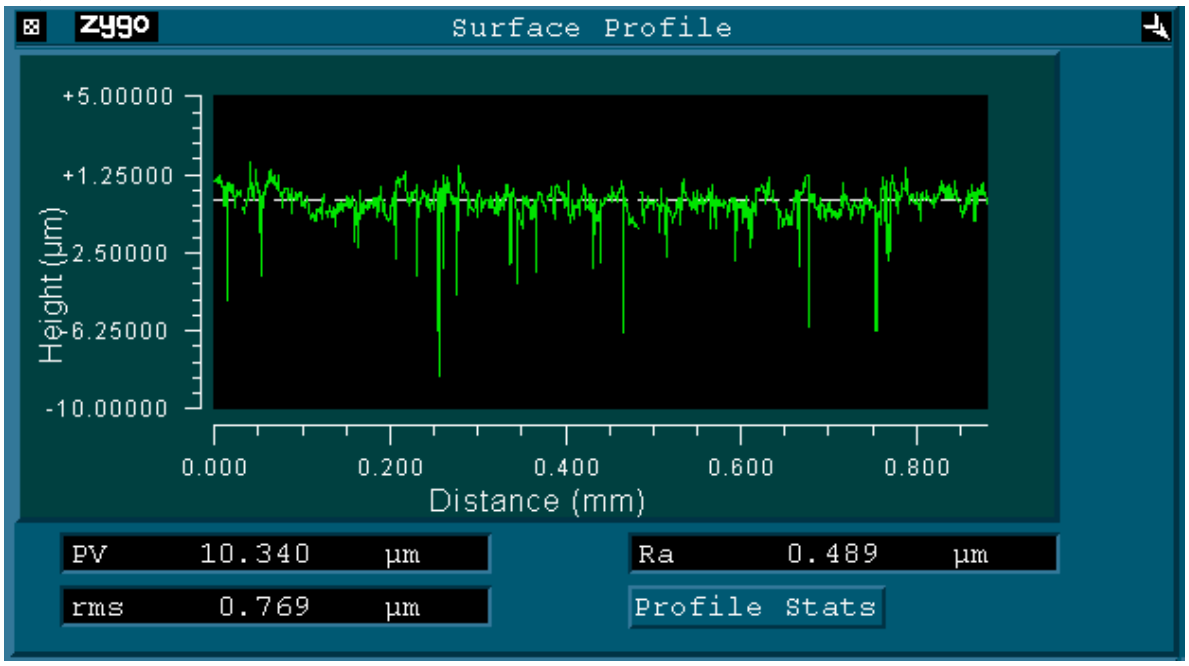
zygo
Surface Profile
+5.00000
+1.25000
-2.50000
-6.25000
-10.00000
Height (µm)
0.000
0.200
0.400
0.600
0.800
Distance (mm)
PV 10.340 µm
rms 0.769 µm
Ra 0.489 µm
Profile Stats

b)

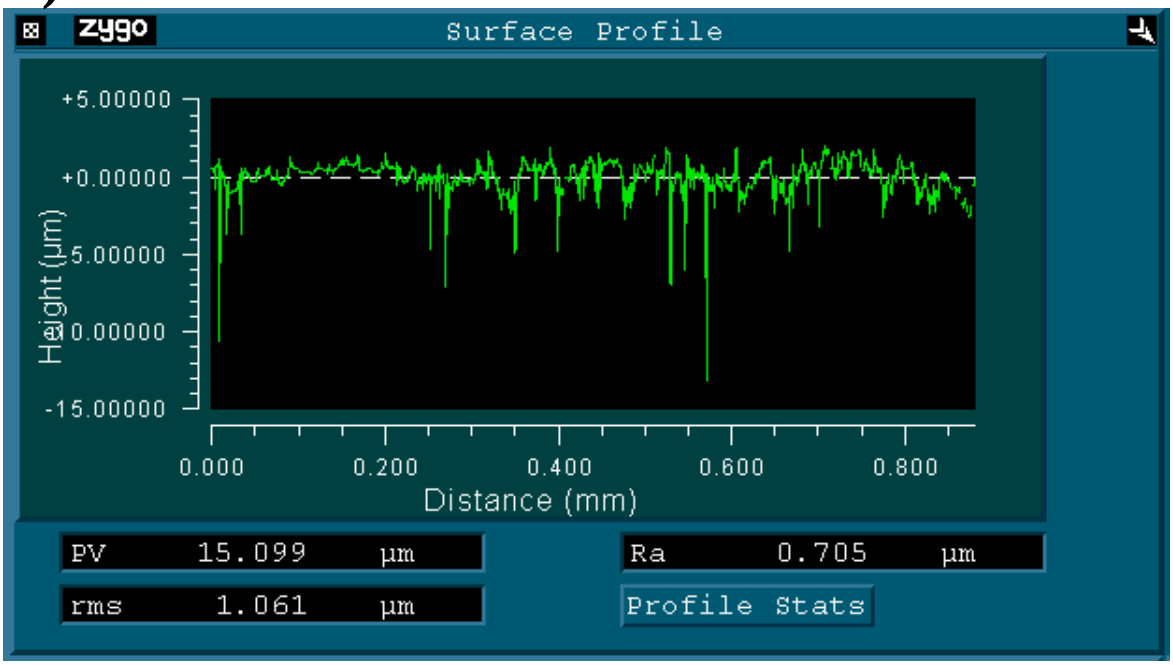
zygo
Surface Profile
+5.00000
+0.00000
-5.00000
-10.00000
-15.00000
Height (µm)
0.000
0.200
0.400
0.600
0.800
Distance (mm)
PV 15.099 µm
rms 1.061 µm
Ra 0.705 µm
Profile Stats

c)

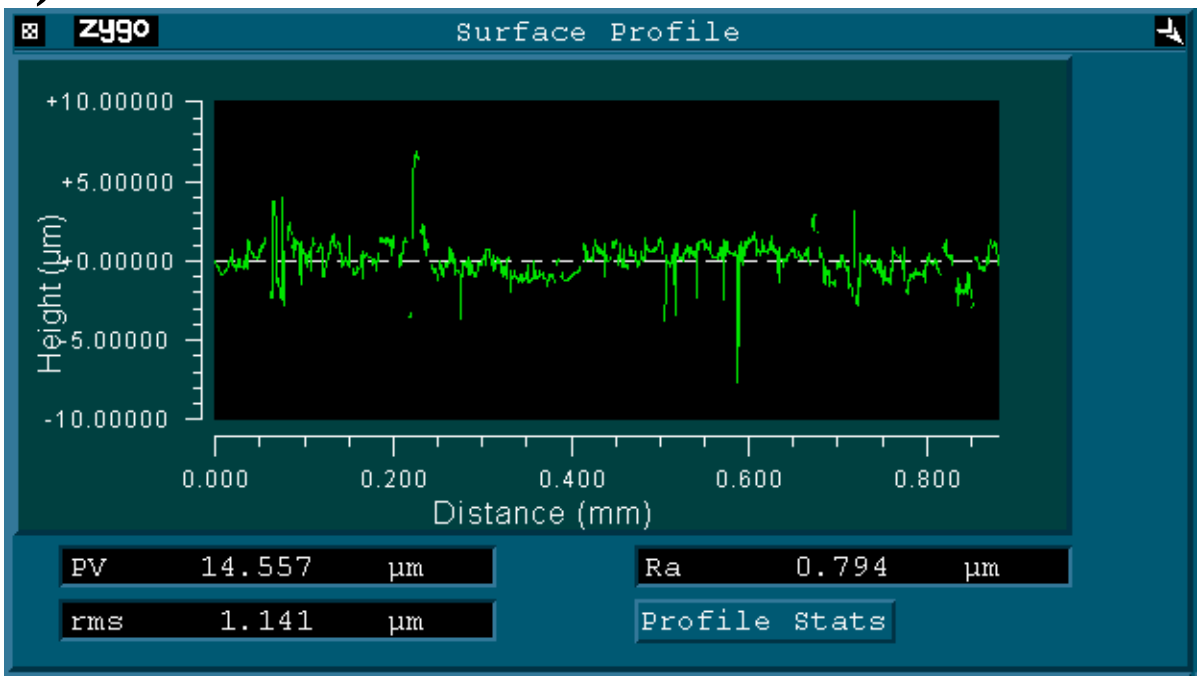

d)

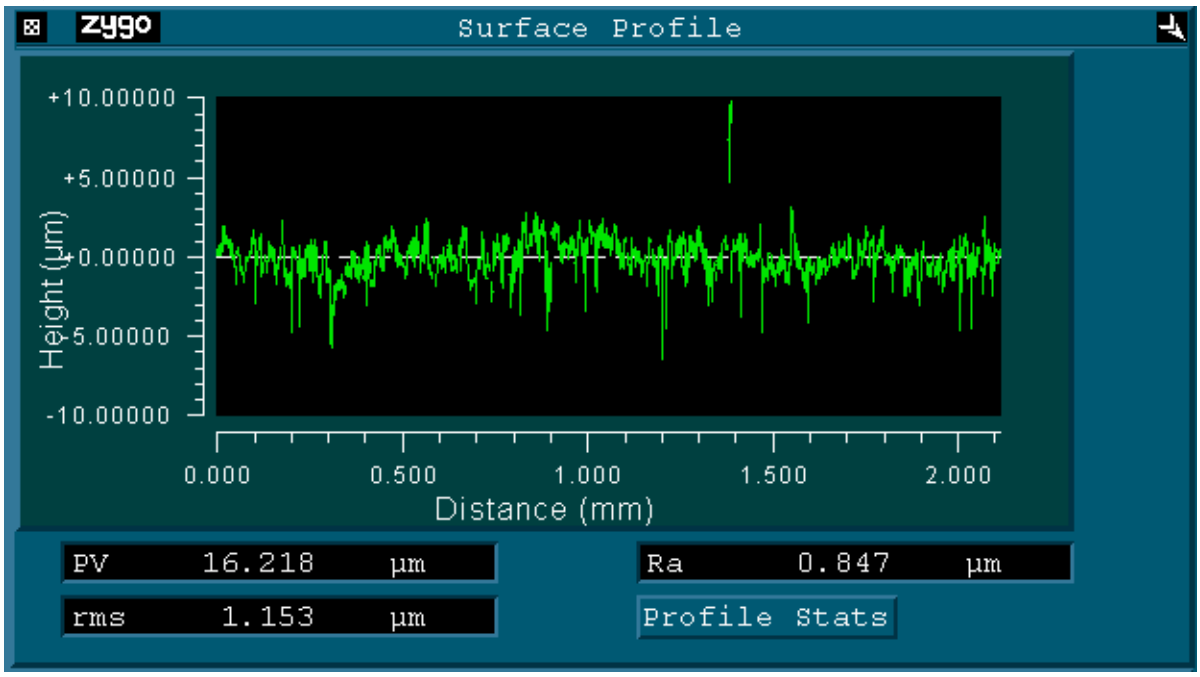

Figure 2.9 Surface profilimeter traces of PCD samples. Experimental conditions are: (a) as-received PCD; (b) LSP at single pulse/sec and power density of 17.69 GW/cm^2; (c) LSP at 5 pulse/sec and power density of 12.74 GW/cm^2 (d) LSP at 10 pulse/sec and power density of 14.15 GW/cm^2

4. Conclusions

A Q-switched Nd: YAG pulsed laser (1064 nm) was utilized to shock process PCD tools and nano-diamond powder compacts as a function of peak power density and pulse repetition rate. Purification, favorable phase transition and improvement in hardness of PCD tools were achieved; however, microstructures became inhomogeneous and surfaces turned out to be rougher. Cold sintering and subsequent annealing of nano-diamond powders resulted in a porous compact with expectedly lower hardness than PCD. Upon laser shock processing, the impurities were reduced, densification was improved and hardness was increased. Thus, shock waves created by the laser caused the diamond for higher quality and improved hardness.

Acknowledgments

This material is based upon work supported by the National Science Foundation under Grant No. CMMI-1029072. The authors also acknowledge the cold sintering facility provided by Larry Jones in Ames Laboratory and scanning electron microscopy services by Yufeng Wu in Mechanical Engineering Department of Iowa State University.

CHAPTER 3. LASER SHOCK PROCESSING ON MICROSTRUCTURE AND HARDNESS OF POLYCRYSTALLINE CUBIC BORON NITRIDE TOOLS WITH AND WITHOUT NANODIAMOND POWDERS

A paper published in the Journal of Materials and Design

Roslyn Melookaran[1,2], Ammar Melaibari[1,2], Cheng Deng[1,2], Pal Molian[1,3]

Abstract

High amplitude, short duration shock waves created by a 1064 nm, 10 ns Q-switched Nd:YAG laser were used to increase the hardness as well as build successive layers of nanodiamond on sintered polycrystalline cubic boron nitride (PcBN) tools. Multiple scans of laser shocking were applied. Scanning electron microscopy, Raman spectroscopy, Tukon micro-hardness tester, and optical surface profiliometer were used to evaluate the microstructure, phase change, Vicker's micro-hardness and surface roughness. Results indicated that laser shock processing of plain PcBN changed the binder concentration, caused phase transition from cubic to hexagonal form, increased the hardness, and almost unaffected surface roughness. Laser shock wave sintering of nanodiamond powders on PcBN resulted in deagglomeration and layer-by-layer build-up of nanoparticles for a thickness of 30 μm inferring that a novel solid freeform technique designated as "shock wave induced freeform technique (SWIFT)" is being discovered for making micro-tools. Depending on the number of multiple laser shocks, the hardness of nanodiamond compact was lower or higher than that

---

[1]Student and Professor, respectively,
Department of Mechanical Engineering, Iowa State University.
[2]Equal contribution to this work
[3]Corresponding author

of PcBN. It is hypothesized that nanodiamond particles could serve as crack deflectors, increasing the fracture toughness of PcBN.

1. Introduction

Cubic Boron Nitride (cBN) is one of the hardest materials known to mankind, exceeded only by diamond. Unlike naturally-existing, covalently-bonded diamond, cBN is a synthetic material exhibiting both covalent and ionic bonds. Consequently cBN surpasses diamond in thermal and chemical stability while retaining high atomic density (1.68×10^{23} cm^{-3}) and maximum hardness of 70 GPa. Besides the cubic form, BN exists in four other allotropes: hexagonal BN (hBN), rhombohedral BN (rBN), explosive BN (eBN), and wurtzitic BN (wBN) [76]. The three phases - hBN, rBN and eBN - are softer with trigonally sp^2 bonded structures while the other two phases - cBN and wBN - are harder with tetrahedral sp^3 bonded structures. Furthermore, amorphous BN (highly disordered structure) and turbostratic BN (disordered, graphitic-like structure) were also found. Among all the forms of boron nitride, cBN is the most thermodynamically stable phase at standard conditions [77] although it is formed from hBN under extreme pressure and temperature conditions [76].

One significant application of cBN is cutting tools used in machining of hard ferrous alloys [78]. Extensive works have been reported on the use of polycrystalline cubic boron nitride (PcBN) as high-performance cutting tools in industry [79-82]. Although polycrystalline diamond (PCD) is much harder and more wear resistant, PcBN has superior thermal and chemical stability required for machining ferrous alloys. PcBN tools are made by mixing hBN powders with a binding agent (usually a metal like Al or ceramic such as TiN),

in a hydraulic press machine with six-way or two-way diamond anvils. The mixture is then sintered at high pressures (6-8 GPa) and high temperatures (1773-2273 K) [78, 83]. During sintering, the powder particles undergo both plastic deformation and chemical reaction with the binder in a complex fashion that is not fully understood [84, 85]. Depending on the grain size (1-20 μm) and type of binder and its volume fraction, the hardness of PcBN tools can vary from 30 GPa to 70 GPa. PcBN is also resistant to chemical attack up to 1500-1600 K in the presence of ferrous metals [86]. PcBN cutting tools are used in precision machining and finishing of hard-to-machine materials allowing for higher levels of productivity, accuracy and reliability in manufacturing [87, 88].

Despite their superior mechanical and physical properties and cutting performance, the PcBN tools suffer from lower toughness and higher production cost. Consequently its applications are limited to finish and semi-finish machining of hard materials. In order to extend PcBN's application to rough and interrupted machining such as milling, the microstructure and composition of PcBN must be modified to increase its toughness. In this chapter, the potential use of laser shock treatment with and without nanodiamond powder to improve hardness and toughness was reported.

Laser shock processing (LSP) is a novel method of strain hardening the materials through compression; it has been successfully applied to increase the hardness and fatigue strength of metals such as aluminum alloys [65, 89-90]. The process involves the use of a high intensity, nanosecond pulsed laser to deliver the high-amplitude stress waves through the target material. Shock waves are generated by laser vaporizing a thin layer of sacrificial material having a low heat of vaporization such as black paint deposited on the surface of target material and forming plasma between the target and the transparent overlay such as

glass. The confinement of plasma by the overlay enhances the amplitude and duration of the pressure pulse and increases the shock wave pressure levels thereby causing structural changes, residual stresses and densification in the target material. It may be noted that the sacrificial material protects the target material from melting and vaporization.

LSP has potential to make PcBN as one of high-performance, high-functionality materials. In addition, embedding or layering nanodiamond (4-8 nm) in PcBN can further enhance hardness and toughness making it useful for rough and interrupted machining. Under the pressures of LSP (up to 5 GPa), nanodiamond powders can be sintered in cold condition. Nano-diamonds have increased surface area to volume ratio and exhibit higher surface reactivity than macro and microcrystalline diamond. Applications for nanodiamond include deposition of wear and corrosion-resistant metal coatings, cooling fluids, and lubricants [43].

Recently there is a spur of research activities in developing cBN/nanodiamond composites (both bulk sintered and thin films) for improving the electronic and mechanical properties. Synthetic PcBN was prepared by powder metallurgy with the addition of nanodiamond, titanium, aluminum and silicon at 5.5 GPa 1200°C for 500 s [89]. Nanodiamond reacted with silicon, titanium and aluminum to form various compounds with super hardness, high heat resistance and high stability. There was no graphitization of nanodiamond during the sintering process due to the presence of silicon [91]. Another work dealt with the growth of cBN/nanodiamond composite thin films by plasma enhanced CVD for improved properties [92].

In this paper we report the effects of LSP on the microstructure, phase transition, hardness and surface roughness of PcBN cutting tool with and without nanodiamond. A groove type of structure on PcBN by direct laser irradiation was created prior to the addition of nanodiamond powder. Fig.3.1 shows a schematic of LSP of PcBN with a layering of nanodiamond powder. The rationale for using nanodiamond is two-fold: (1) due to its fine size (4-8 nm), nanodiamond can fill in the voids between cBN crystals and the binder and thereby increasing the density of PcBN; (2) due to large surface area-to-volume ratio, nanodiamond can react easily with binders to form various carbides and thereby increasing the strength and hardness of PcBN or exist as individual particles offering toughness to PcBN.

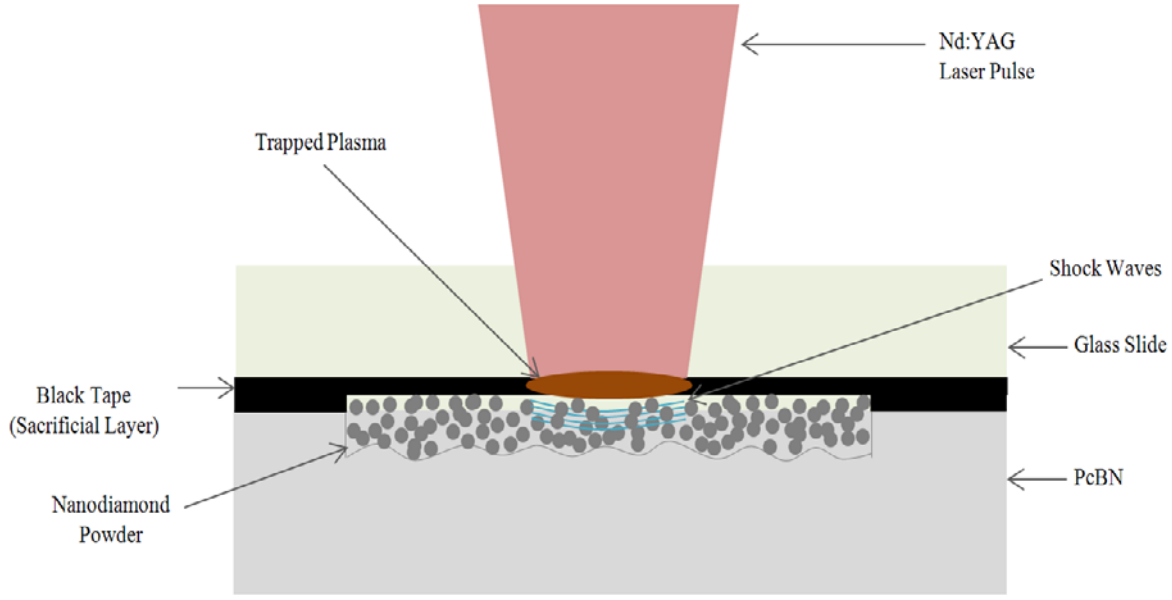

Figure 3.1 Schematic of LSP of PcBN with a layering of ND powder

2. Experimental details

The PcBN blanks with a nominal diameter of 50 nm (Grade HTM), received from Diamond Innovations, Inc. (Ohio, USA), consisted of 0.8 mm thick PcBN layer bonded to a

tough 0.8 mm thick tungsten carbide (WC-13% Co) substrate. The PcBN layer is composed of 2 lm size cBN particles embedded in a TiN matrix. The composition of PcBN is 50% cBN, 45% TiN and 5% AlN by volume. The nanodiamond powders (90% purity, 4-8 nm in size, spherical/elliptical particles produced by the detonation of explosives) were procured from Ukraine (sintal@yandex.ru). The surfaces of the nanodiamond particles contained many functional groups such as hydroxyl, carbonyl, carboxyl and ether-based resin.

A 1064 nm, Q-switched Nd:YAG laser (Quantel 481 near diffraction limited beam) was employed to create high amplitude, short duration shock waves. The laser parameters were set at pulse width of 10ns, average power of 2 W and frequency of 10 Hz. A defocused beam of 1mm diameter was used throughout the experimentation with a calculated peak power density of 2.55 GW/cm^2. Typical range of peak power density for laser shock processing is 1-5 55 GW/cm^2 [65].

The PcBN samples were subjected to LSP by applying a black tape (0.21 mm thick) as a sacrificial layer (to protect the sample's surface from direct ablation and melting) followed by placement of a transparent overlay (microscope glass slide, 1 mm thick). A thin layer of high vacuum grease was used to secure the glass slide on the sample. The overlay assists in increasing the shockwave intensity by confining the expanding plasma and thus the pressure developed propagates through material causing densification of the sample [89].

For PcBN samples without the addition of nanodiamond (B1 through B5 in Table 3.1), five different samples each with a size of 6.4 × 6.4 mm were prepared and laser shocked from one to five scans at a x-y positioning stage speed of 0.5 mm/s in x-direction and a movement of 0.75 mm in y-direction; such parameters allowed for a horizontal overlap of

95% and a vertical overlap of 25%. Increased overlap was preferred because it was reported that multiple shocks of a region would increase the plastically-affected depth [65].

For the PcBN samples with nanodiamond powder, grooves were first produced for an area of 3.8 × 3.8 mm on the PcBN using the identical laser parameters as in LSP (no overlay and no sacrificial layer). The average depth of grooves based on 10 measurements was recorded as 20 ± 2 μm. After depth measurements were taken, nanodiamond powders were layered flush with the top of the sample surface and little above. The black tape (sacrificial layer) was then glued on the top of sample and around the grooved area to act as a shallow fence for nanodiamond powders. The glass slide was mounted on the sample using a thin layer of grease and then subjected to LSP. Finally, the samples were rinsed in acetone to remove the excess powders and residues of black tape. Samples C1 through C4 were prepared as listed in Table 3.1. For C1, one nanodiamond layer was added and then shock processed in one laser scan. For C2, LSP was repeated five times (five scans), each time adding a new layer of nanodiamond. For C3, one layer of nanodiamond was applied but LSP was repeated five times (five scans). For C4, one layer of nanodiamond was applied but LSP was repeated 10 times (10 scans). It may be noted the 0.2 mm thick black tape lasted for three scans of LSP after which it was replaced. The thickness of nanodiamond layer from the bottom of groove was measured using an optical microscope with a resolution of 1 μm. ten measurements were performed for each case and the average value was recorded.

Raman spectroscopy of LSP regions was performed to identify the phase transitions using Ar-ion laser with a 20 lm entrance slit width, 50mW laser power, and 488 nm operating wavelength. A scanning electron microscope (SEM) operating at 20 kV (Oxford EDS system JEOL 6060LV) in the secondary electron mode was then used to examine the microstructure

of PcBN and uniformity of ND powder compaction. A Wilson Tukon micro-hardness testing machine was used to measure the Vickers hardness of LSP regions. The loading conditions were a 1 kg load and a dwell time of 10 s. The diagonals of indentations were measured using a Nikon Eclipse microscope coupled with a CCD camera at 1000× magnification. At least 10 hardness measurements were made per sample to get an average hardness value and a standard deviation. Finally surface roughness was evaluated using the Zygo New View 5000 series optical profilometer with 20× objective.

Table 3.1 Sample designations and associated experimental conditions

Designation	Sample	Treatment	Thickness of nanodiamond layer (μm)
A1	PcBN	Untreated	-
B1	PcBN	One time of LSP	-
B2	PcBN	Two times of LSP	-
B3	PcBN	Three times of LSP	-
B4	PcBN	Four times of LSP	-
B5	PcBN	Five times of LSP	-
C1	20 μm depth-grooved PcBN	One layer of nanodiamond and one scan of LSP	3 μm from the bottom of groove
C2	20 μm depth-grooved PcBN	Five layers of nanodiamond and one scan of LSP for each layer	31 μm from the bottom of groove
C3	20 μm depth-grooved PcBN	One layers of nanodiamond and 5 scans of LSP	14 μm from the bottom of groove
C4	20 μm depth-grooved PcBN	One layer of nanodiamond and 10 scans of LSP	13 μm from the bottom of groove

3. Results and discussion

3.1 Laser shock processed PcBN samples (B2-B5)

Fig.3.2 shows the micro-hardness test data of both untreated and laser shock processed samples. A maximum hardness of 4500 kg/mm^2 (45 GPa) was obtained in sample B2, with an increase in micro-hardness of 15% over untreated PcBN; such an increase in hardness could be attributed to a number of factors including plastic deformation of cBN particles, phase transition of hBN, development of residual stresses, stress fracturing of binder phases and reduction in porosity and other flaws due to densification. Maximum hardness was reached only after two scans of LSP. Although successive laser scans allow for increased strain hardening and build-up of compressive residual stresses deeper into the surface which assist in increasing the hardness [89], there may be other deleterious effects such as removal or dissolution of binder materials and transformation of cBN to hBN that might have caused a loss in hardness. Let us now examine the evidence for hardness changes from SEM images and Raman spectroscopy data.

SEM images of untreated and laser shock processed PcBN as a function of number of scans are presented in Figs. 3.3 and 3.4. The microstructure of untreated sample (Fig. 3.3) consists of 2 μm-sized particles of cBN (dark) and sub-lm sized particles of AlN (light) in a matrix of TiN (gray). The microstructure is homogenous and the binding phase is uniformly distributed in its volume. The micrographs do not reveal any detectable pores within this scale suggesting that the material is nearly fully densified. Although not shown here, PcBN is likely to contain structural defects namely dislocations and microtwins and TiB_2 at the interfaces and grain boundaries based on transmission electron microscopy analysis of cBN/TiN systems [93, 94].

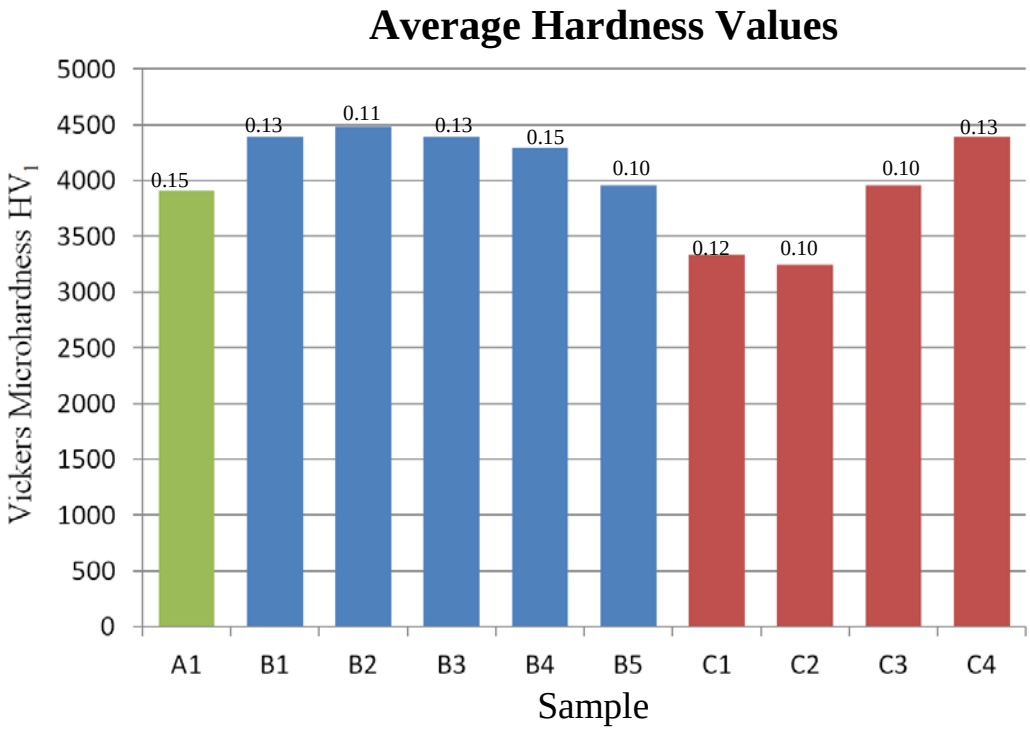

Figure 3.2 Average micro-hardness values of PcBN samples with and without nanodiamond. Coefficient of variation is listed above each bar.

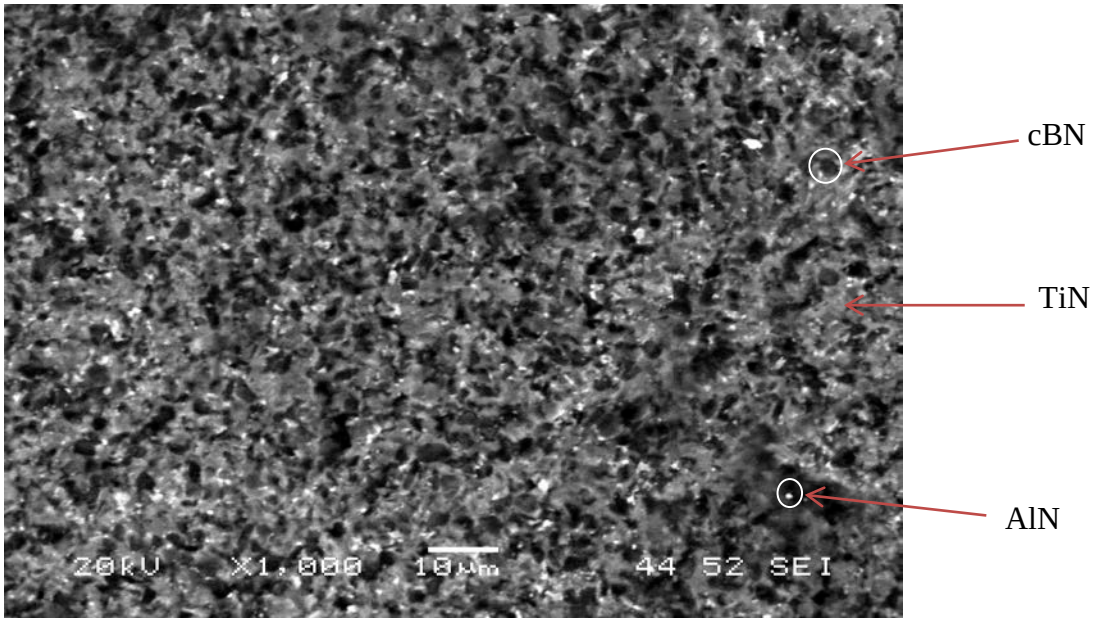

Figure 3.3 SEM image of untreated PcBN sample (A1)

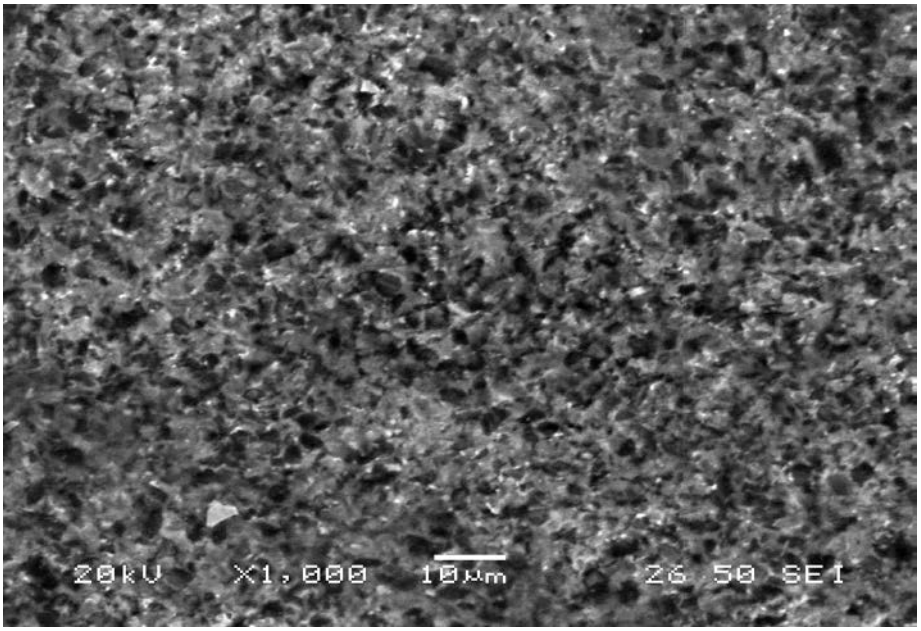

(a) Sample B2

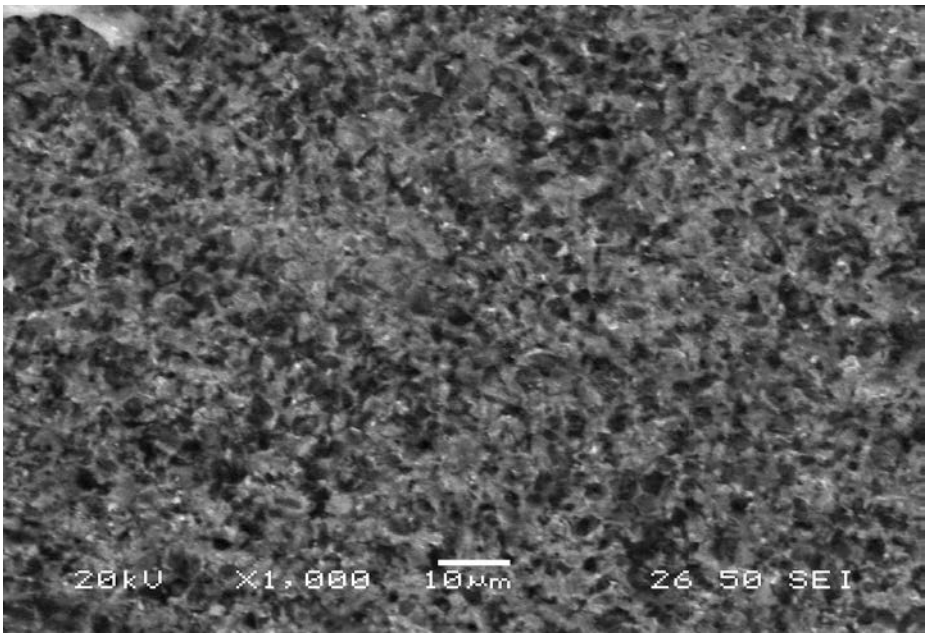

(b) Sample B5

Figure 3.4 SEM images of laser shock processed PcBN samples: (a) LSP two times (B2) and (b) LSP five times (B5)

After LSP, the particle size and volume fraction of cBN remained nearly same; however, there was a significant reduction in the amount of AlN (Fig. 3.4). In sample B5,

AlN has almost disappeared indicating the following plausible explanations: one is the stress fracturing and dissolution of AlN in the TiN matrix to form a solid solution of TiN and AlN; other is the stress fracturing and removal of AlN leaving fine porosity. Both can contribute to the reduction in hardness. It can be seen from Fig. 3.2 that hardness first increases with number of shocks and then decreases upon further increase of shocks. There is an increased plastic deformation with increase in shocks. However, multiple shocks may break the binder particles bridging the cBN grains, thus reducing the hardness of the material. In addition, phase transformations result in hardness changes.

Raman spectrum of untreated PcBN sample (Fig. 3.5) shows four Raman peaks: 1069, 1201, 1319, and 1579 cm^{-1}. The weaker intensity peaks and wider widths are typical of polycrystalline samples compared to single crystalline samples. The position of Raman peaks and their full width at half maximum (FWHM) in PcBN depends on the grain size, residual stresses, impurities, binder, extent of plastic deformation and defects. Peaks at 1069 and 1319 cm^{-1} are correlated with TO and LO phonon scattering that originates from the cBN phase. The peak positions of cBN are upshifted from the values corresponding to the single crystalline cBN, which typically have TO and LO peaks at 1056 and 1304 cm^{-1}, respectively. The upshifted and broadened peaks can be attributed to the plastic deformation which takes place during the sintering process [95], a reduction in the crystallite size during the sintering process [96] and the presence of impurities/defects which comes from the binder materials [97]. The 1201 cm^{-1} peak can be assigned to a boron-doped phase [98] which could be generated by some defects in the sample during the sintering process. The 1579 cm^{-1} peak is correlated with the eBN phase which typically has a peak around 1588 cm^{-1} [99].

After laser shocking tow times (Fig. 3.6), the cBN peaks are downshifted slightly to 1067 and 1310 cm^{-1}. The position of Raman peaks can be used to characterize the residual stresses. Experiments have provided that a Raman shift of 3.39 $\pm$ 0.08 cm^{-1}/GPa for the TO Raman peak and 3.45 $\pm$ 0.07 cm^{-1}/GPa for the LO Raman peak [100]. Based on this data, LSP-induced residual stresses can be calculated in the range of 0.6-2.6 GPa. Such stress values are also observed in other processes such as CVD and PVD. For example, a plasma CVD process induced 2-3 GPa residual stresses in cBN thin films which are even lower than those obtained with PVD films [92]. Analysis of diamond-indented single and polycrystalline cBN samples resulted in shifts of the Raman lines from their unstressed positions and indicated a compressive stress field with stresses ranging from 0.07 to 0.3 GPa [95].

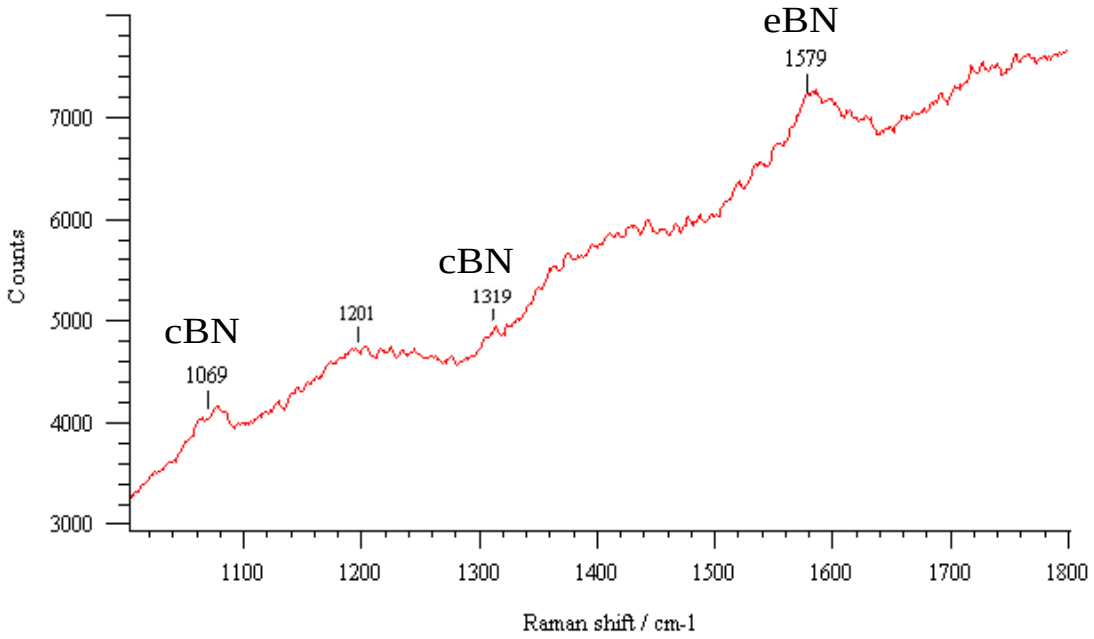

Figure 3.5 Raman spectrum of sample A1 (untreated)

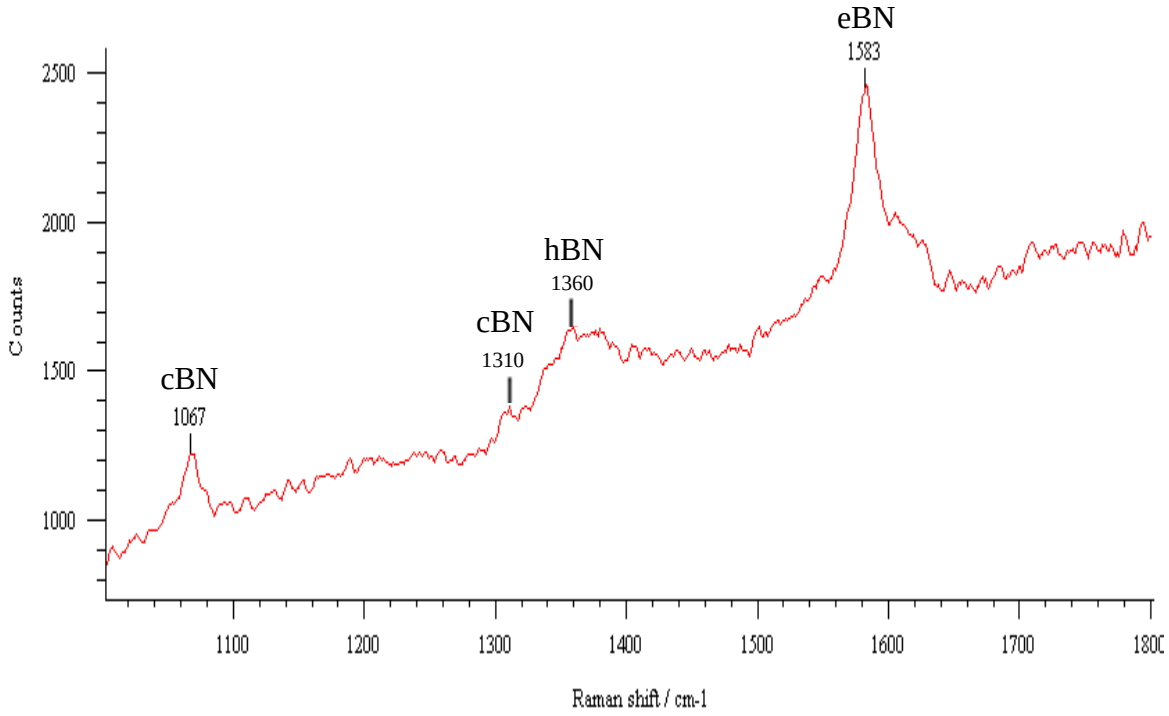

Figure 3.6 Raman spectrum of sample B2 (two times LSP)

In sample B2, the disappearance of the 1201 cm^{-1} peak and the presence of the 1360 cm^{-1} peak indicate a transformation of cBN to hBN which typically has a 1366 cm^{-1} peak [76]. It should be mentioned that the characteristic peak of hBN (1366 cm^{-1}) is much stronger than that of cBN because the scattering coefficient of hBN is two orders of magnitude higher than that of cBN [92]. The eBN peak was also upshifted and the peak became sharper. The reason for the upshift is not clear at the moment; however, the sharpness of the peak suggests an increase of the transformation of cBN to this phase. Increasing the number of laser scans seems to increase the transformation of cBN to hBN and eBN phases.

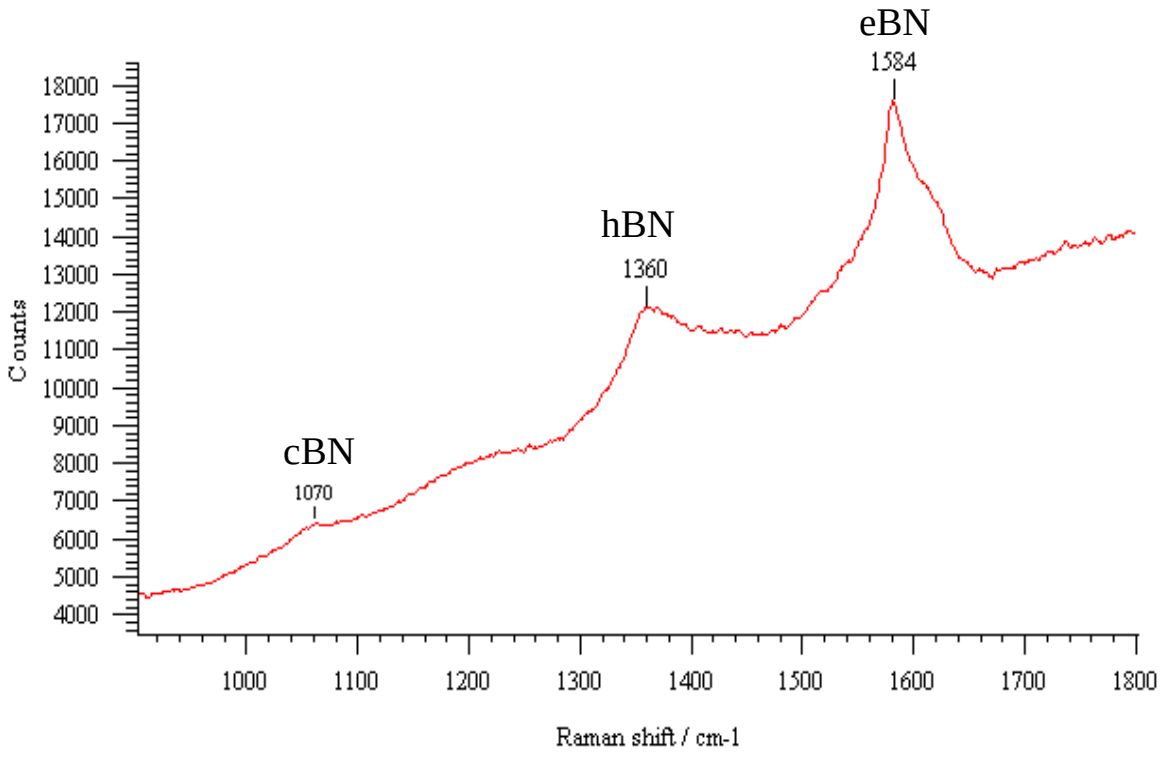

Figure 3.7 Raman spectrum of sample B5 (five times LSP)

In the Raman spectrum of the sample subjected to LSP five times (Fig. 3.7), the hBN and eBN peaks become sharper while the cBN peak almost disappeared. Thus, the loss in hardness with five times LSP is primarily attributed to a change from hard cBN to soft hBN phase. It is hypothesized that multiple shock wave compression creates lattice strain and defects and results in the strain accumulation leading to conversion of cBN into hBN by some sort of diffusion mechanism.

Optical profilometer traces (Figs. 3.8 and 3.9) of LSP treated PcBN show that surface roughness parameters (Ra, rms, peak-to-valley) have slightly increased with the number of laser scans. Untreated PcBN has an even distribution of peaks and valleys with a Ra of 0.421 μm. With LSP scans, the Ra increased marginally and the formed surface has

concentrated areas of peaks and valleys. The loss of AlN particles leaving a porous structure on the surface might have also contributed to the surface roughness.

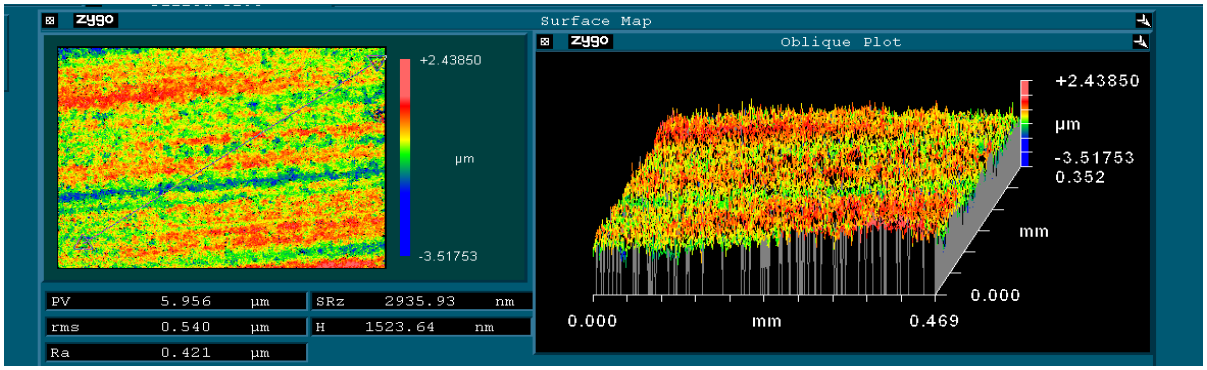

Figure 3.8 Optical profilometer trace of untreated PcBN (Sample A1)

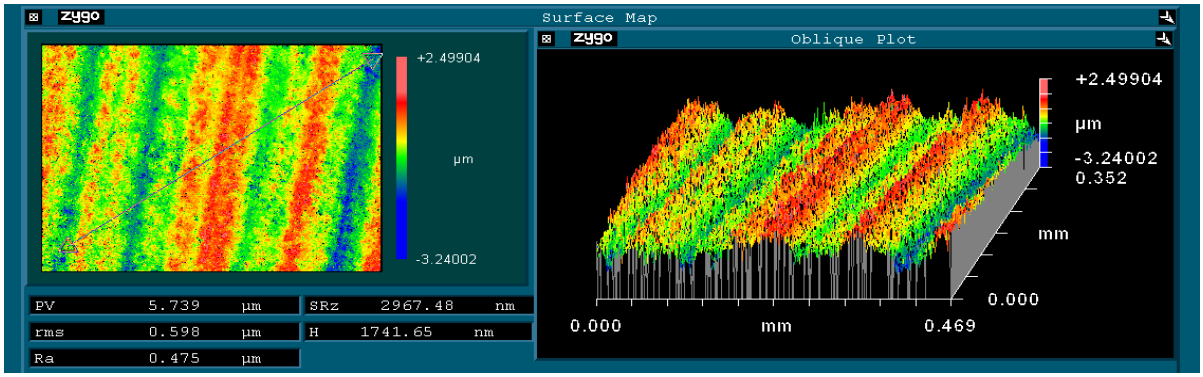

(a) Sample B2

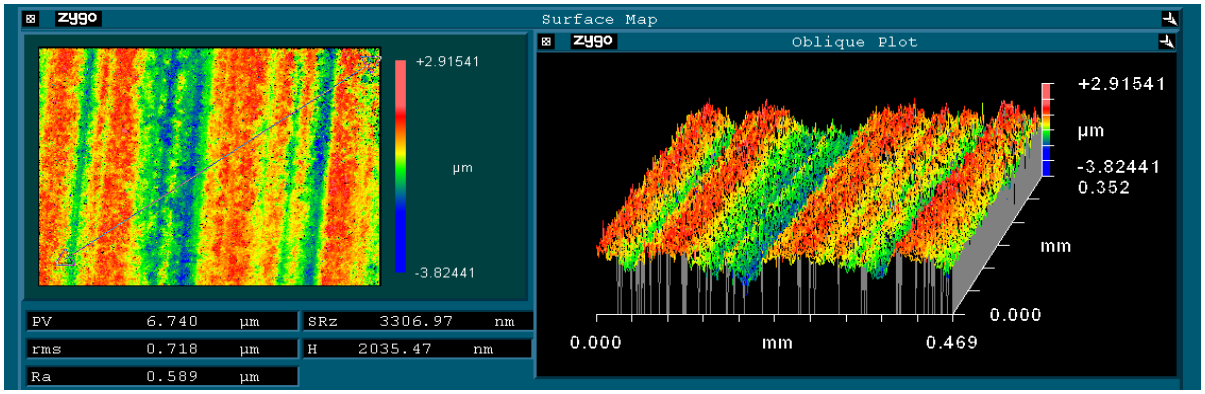

(b) Sample B5

Figure 3.9 Optical profilometer traces of LSP treated PcBN: (a)sample B2 and (b)sample B5

3.2 Laser shock processed PcBN samples with nanodiamond

Table 3.1 shows that the thickness of nanodiamond deposit on PcBN by LSP depends on the number of scans and number of nanodiamond layer additions. It may be noted that without the groove formation, there is no bonding of nanodiamond on the PcBN substrate. With only single layer nanodiamond powder, the average rate of deposition was about 3 μm per scan for up to five scans after which the number of scans do not appear to influence the deposit thickness. It is believed that significant amount of shock wave energy is to be expended initially to bind the nanoparticles in the grooves. However, rapid build-up of thickness occurs if nanodiamond powders are added in between scans. For example, sample C2 exhibits a total average thickness of 31 μm (11 μm above the baseline surface of the PcBN) in five scans. Multiple laser scans thus increased densification and reduced the amount of loose powders.

Micro-hardness test data shown in Fig. 3.2 indicates that best results were obtained with multiple LSP scans over the same area. In samples C1 and C2 (one scan per layer), the micro-hardness was lower due to lower densification of nanodiamond and agglomeration that skewed the micro-indentation process. However, the sample C4 processed with 10 scans had much improved densification, reduced agglomeration and better bonding for a net 12% increase in hardness over untreated PcBN. It may be noted that nanodiamond are not hard unless fully consolidated. For example, plasma pressure compaction of detonation synthesized nanodiamond between 700 and 1200 ^{o}C under 65 MPa pressure yielded only porous pellets having a hardness of only 0.2 GPa [43]. Micro-hardness of high-purity detonation nanodiamond in 100% dense form was reported to be 30-35 GPa [101].

Nanodiamond compacts sintered from high purity, 25 nm size diamond crystals at high pressure of 8 GPa and temperature above 1500 ^{o}C produced hardness of 50 GPa [102].

PcBN usually fails in a brittle manner with rapid crack propagation throughout a stressed material. The resistance of PcBN to crack propagation can be significantly enhanced by the grain size and by adding various reinforcements such as secondary phase particles, whiskers and fibers. In the present study, we hypothesize that nanodiamond particles contribute to weak interfaces and high residual stresses between cBN and nanodiamond as a result of their thermal expansion difference; this will allow the crack to be deflected away leading to improved toughness in PcBN.

SEM micrographs displayed in Fig.3.10 illustrate that the agglomeration of nanodiamond is reduced upon multiple scans (compare C1 and C3). The pressure from the shock processing is great enough to break down the nanodiamond agglomerates, and disperse them more evenly over the area. Sample C2 exhibited similar sized agglomerates as in C1, but there was also varying heights in relation to the base of the groove. Sample C3 has the smallest and most evenly dispersed agglomerates.

Raman spectroscopy analysis of sample C1 revealed the presence of nanodiamond and different phases resulting from the reactions of nanodiamond and BN, as shown in Fig.3.11. The 1329 cm^{-1} is attributed to nanodiamond [103]. The cBN peaks almost disappeared. The TO mode at 1048 cm^{-1} can be seen very broad, which is due to the possible increase in residual stresses, while the LO mode around 1304 cm^{-1} disappeared completely in the dispersion of the spectrum. The 1201 cm^{-1} peak, which is related to the boron-doped phase that existed in the untreated sample, can be still seen here. Another phase, such as

boron carbonitride with a 1360 cm^{-1} (D bond) and 1600-1620 cm^{-1} (G bond) [104, 105], is also noted even though the D bond for this phase does not appear clearly on the spectrum. The 1397 cm^{-1} and 1601 cm^{-1} peaks show the C=N bonds. The 1700 cm^{-1} peaks, which are close to the theoretical carbonyl peak, could be an indication for the addition of oxygen, upon air exposure, to the C=N bond as in Aramid.

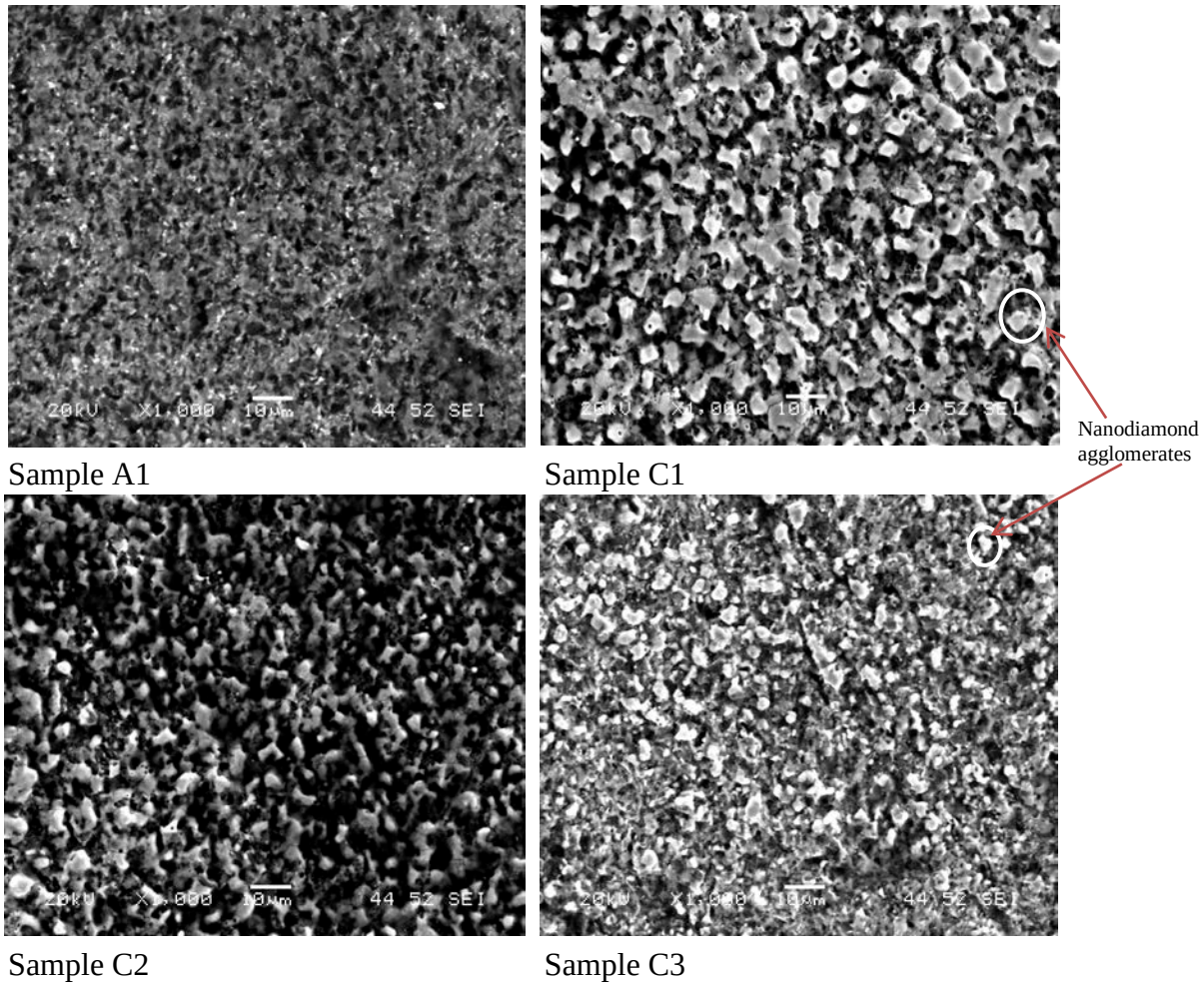

Figure 3.10 SEM images of laser shock hardened PcBN with nanodiamond powders

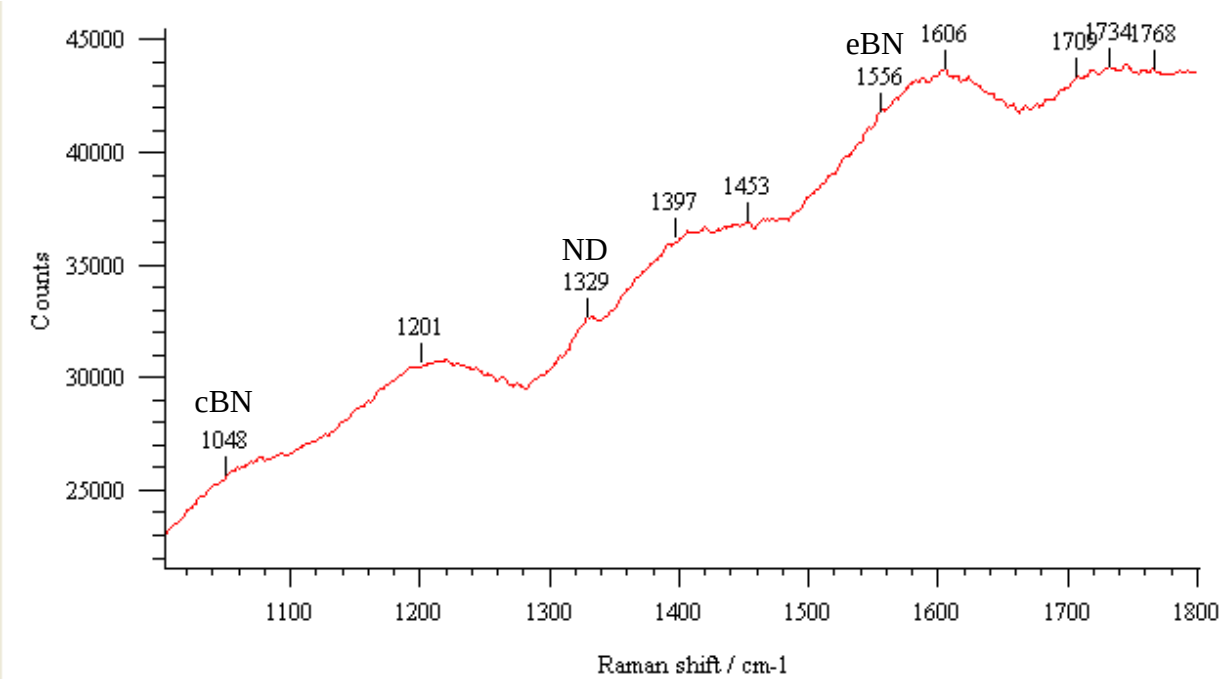

Figure 3.11 Raman spectrum of sample C1

The observations for the case of one layer of nanodiamond with one scan are the same for the case of five layers of nanodiamond with one scan for each (Fig.3.12). The peaks are shifted slightly since the residual stresses increased with each pass. Increasing the number of scans on one layer of nanodiamond (Fig.3.13) increased the transformation of cBN to hBN and nanodiamond to graphite. Note that, the peak at 1593 cm^{-1} can be a result of either an upshifted eBN peak, or the appearance of boron carbide. The C=B bond has a peak at 1590 cm^{-1} [106]. Studies on the microstructural characterization of diamond films deposited on cBN crystals by microwave plasma CVD revealed shifting of Raman peaks that is attributed to thermal stresses caused by the difference in lattice parameter and thermal expansion between diamond and cBN [107].

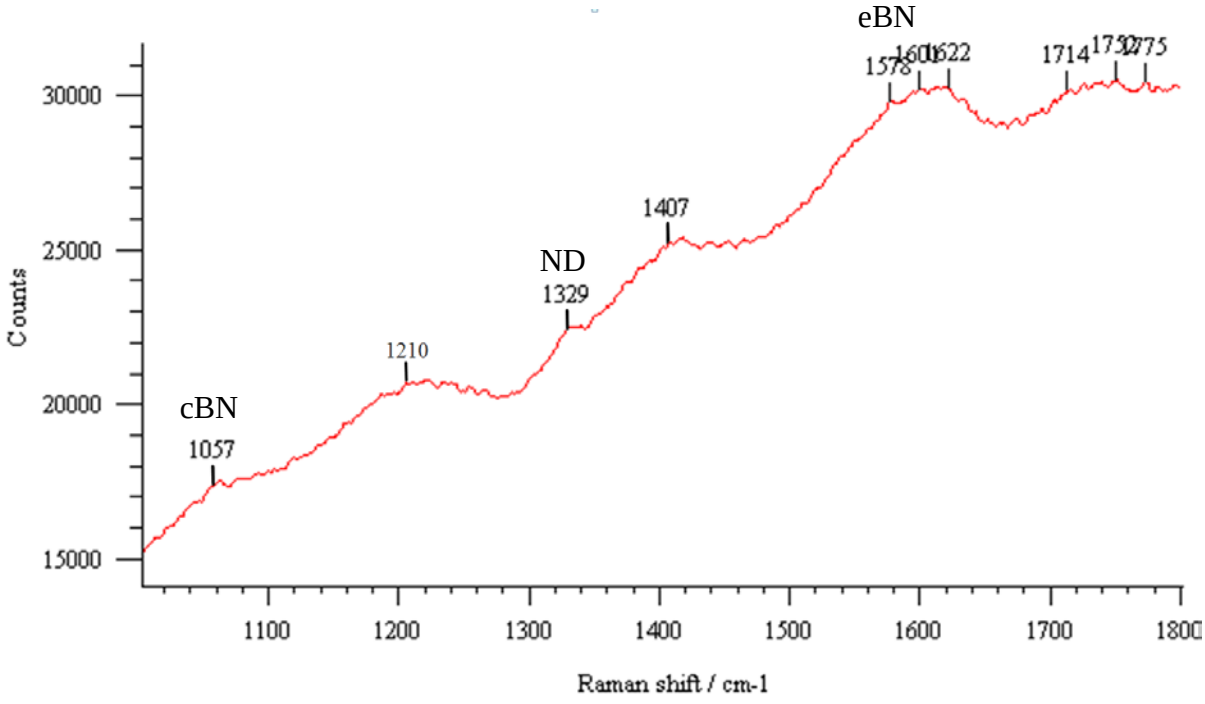

Figure 3.12 Raman spectrum of sample C2

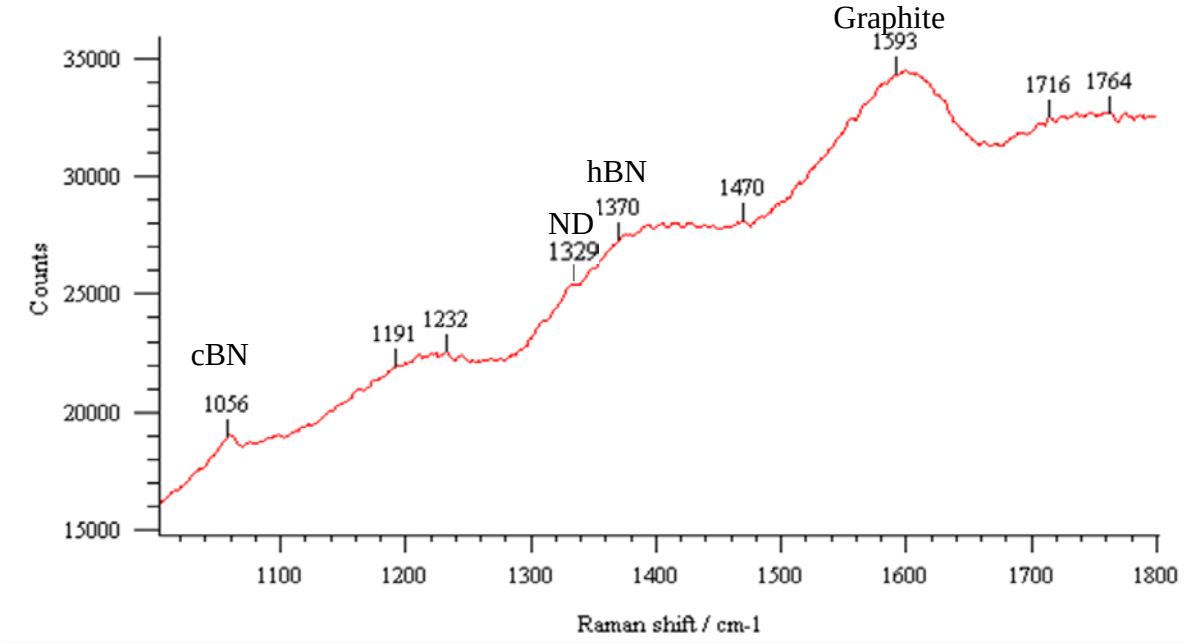

Figure 3.13 Raman spectrum of sample C3

Groove formation coupled with nanodiamond addition and compaction by LSP has increased surface roughness in samples C1-C3 (Fig.3.14). Sample C3 has the largest Ra value (0.688 μm) due to multiple bombardments while sample C2 has the highest peak to valley (PV) due to the addition of multiple layers of nanodiamond and uneven compaction.

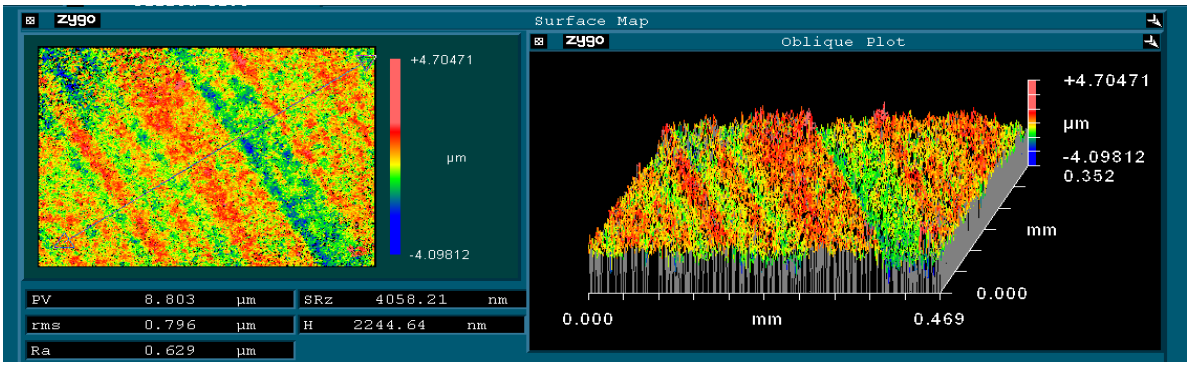

Sample C1

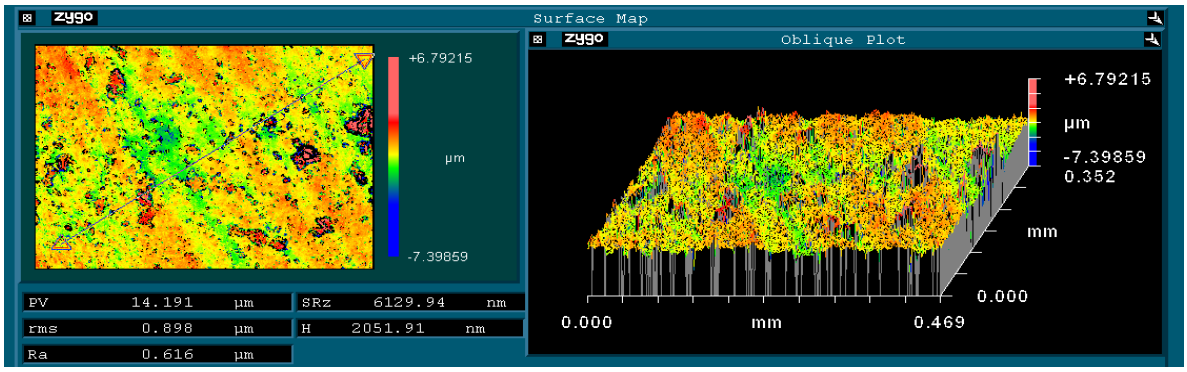

Sample C2

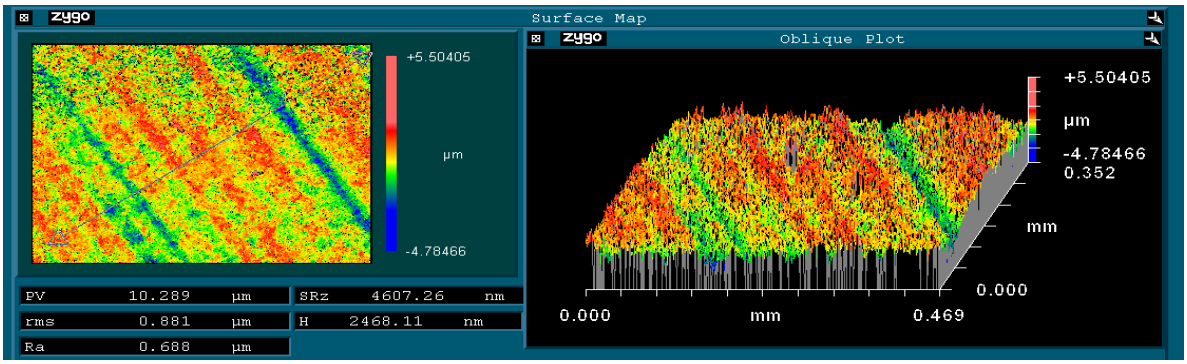

Sample C3

Figure 3.14 Optical profilometer traces of LSP treated PcBN with nanodiamond

4. Conclusions

Laser shock processing of polycrystalline cubic boron nitride (PcBN) caused phase transformation and significant changes in hardness and microstructure. The key parameter that influenced the results was multiple shocks. A maximum of 15% increase in hardness was obtained with two scans under the non-optimized laser parameters. Laser shock sintering of nanodiamond powders on PcBN led to a potential solid freeform fabrication technique of building layer-by-layer to form a micro-diamond tool. The hardness of nanodiamond compacted by laser shock waves was 12% higher than that of PcBN. Multiple shocks not only increased the hardness but also broke down the agglomerates and improved densification. Thus, laser shock processing is a viable technique for increasing the hardness of PcBN and sintering of nanodiamond on PcBN.

Acknowledgments

This material is based upon work supported by the National Science Foundation under Grant No. CMMI-1029072. Roslyn, the lead author, likes to thank NSF’s Research Experiences for Undergraduates for providing an opportunity to participate in the research project.

CHAPTER 4. NANODIAMOND POWDER COMPACTION VIA LASER SHOCKWAVES: EXPERIMENTS AND FINITE ELEMENT ANALYSIS

A paper published in The journal of Powder Technology

Cheng Deng[1,3], Ming Liu[2] and Pal Molian[1]

Abstract

Laser shock sintering (LSS) is an innovative technique employing mechanical forces to densify powders. It can impart compressive stresses into material to improve the relative density and generate residual stresses to enhance the fatigue strength. In this work, LSS of nanodiamond powders embedded in polycrystalline cubic boron nitride (PcBN) substrate was experimentally investigated using a 1064 nm, 10 ns Q-switched Nd:YAG laser with a peak power density of 6.37 GW/cm^2. Finite element simulation (FEM) was applied to predict the mechanical deformations induced by LSS. The dynamic analysis by ABAQUS/Explicit and static analysis by ABAQUS/Standard were performed in detail to predict the residual stress field and densification of nanodiamond powder compacts. The predicted densification of nanodiamond powder compacts are in agreement with the experimental data for single and multiple laser shocks.

---

[1]Graduate student and Professor, respectively,
Department of Mechanical Engineering, Iowa State University.
[2]Graduate student, University of Kentucky
[3]Corresponding author

1. Introduction

More recently, diamond tools (including polycrystalline, single crystal, chemical vapor deposit) have increased number of applications in manufacturing of various microdevices as well as in ductile machining of brittle materials. Nanodiamond is an emerging material with vast potential for tooling applications due to its novel tribological properties [43]. For example, the hardness of nanodiamond (Knoop microhardness, 120-140 GPa) is even greater than that of diamond single crystals (60-120 GPa) [108]. However, there are still no effective ways to manufacture nanodiamond tools by powder sintering. Rather than traditional sintering and manufacturing of nanodiamond tools from powders under high temperature and high pressure, laser shock sintering (LSS) can be considered as an innovative and viable technique. Laser shocks can impart desirable dislocation structures and compressive residual stresses into metals through compression to improve fatigue strength and hardness [40]. By laser shocking, the peak pressure can reach as high as several gigapascals; under such conditions and due to large surface area of nanoparticles, the nanodiamond powders can be compacted without a need for high temperatures.

Finite element method (FEM) was first applied by Braisted and Brockman [109] forthe investigation of mechanical behavior and predication of residual stresses from the laser shocked metals, facilitating a novel way to optimize parameters. Other researchers [110, 111] have then followed with a continuum type approach where the material is assumed to be homogeneous, isotropic and compressible continuum. Some of these simulations have been closely correlated to the experimentally measured residual stresses. However, research on laser shock simulation is mostly limited to bulk metals. There is almost no working of the

FEM simulation of LSS for powder compacts to predict the densification, micro-hardness evolution and residual stress field because of the complexity involved in powder compaction.

In this paper, a systematic experimental study was undertaken to examine the effect of LSS on properties of nanodiamond powder compacts. In addition, a comprehensive FEM simulation was carried out. The behavior of nanodiamond powder compacts subjected to single and multiple laser shocks had been analyzed and compared with the experimental data.

Different from other sintering or laser processes, the principle of laser shockwave method for sintering powder material compact involves exerting a mechanical force rather than a thermal force on the surfaces. In this work, a high intensity, nanosecond pulsed laser beam combined with a suitable transparent overlay is employed to drive the high-amplitude stress waves through the nanodiamond powders filled inside the holes on a polycrystalline cubic boron nitride (PcBN) substrate. A schematic configuration of LSS is depicted in Fig.4.1. A thin sacrificial layer with a low heat of vaporization such as black paint is deposited on the surface of PcBN substrate and then covered with a transparent overlay, which is a dielectric material such as glass. When laser energy is absorbed by this thin sacrificial layer, it burns and creates plasma between the target and overlay leading to the generation of shockwaves. The overlay confines the thermally expanding vapor and plasma against the substrate surface, thus enhancing the amplitude and duration of the pressure pulse and increasing the shock pressure levels; this in turn results in sintering, microstructural changes, residual stresses and densification in the nanodiamond powder compacts. The sacrificial layer also protects the substrate surface from melting and vaporization due to laser heat.

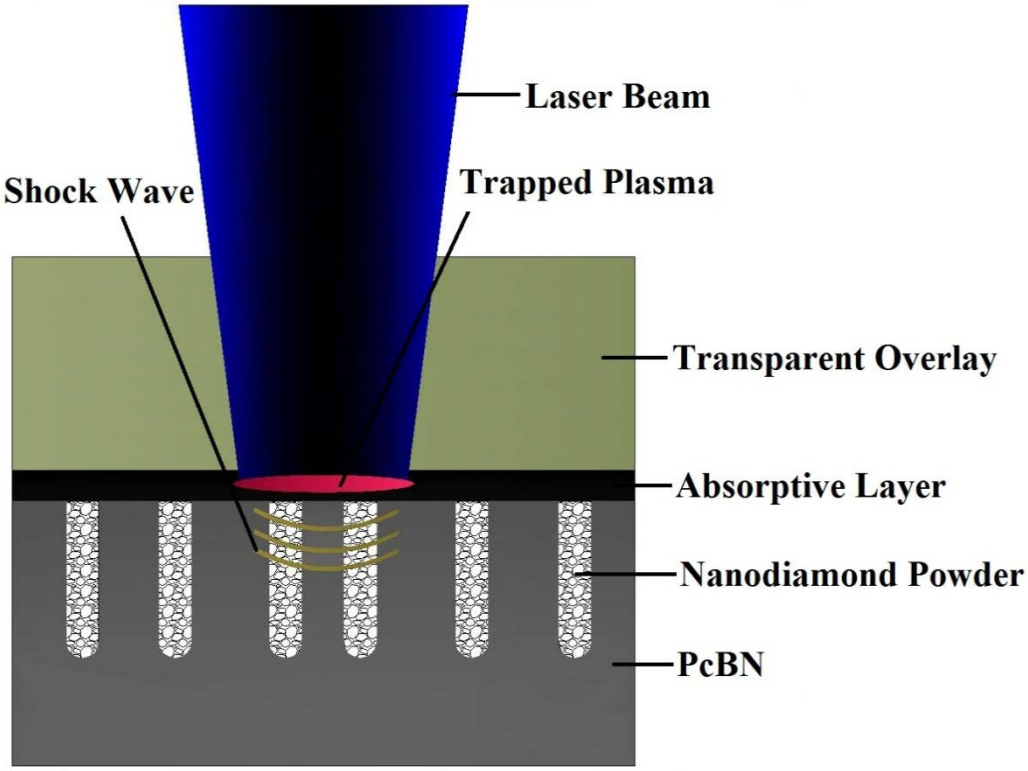

Figure 4.1 Schematic of LSS that holes were drilled and filled with nanodiamond powders

Considering the propagation of confined plasma below the transparent overlay, shockwave peak pressure can be given by Fabbro's model [66] as follows:

$$P_{\max} = 0.01\left\{[\alpha/(2\alpha+3)]ZI_0\right\}^{1/2} \tag{4.1}$$

Where I_0 is the laser power density, α is the efficiency of the interaction ≈ 0.1[66, 67] and Z is the combined shock impedance between the target material and confining medium (in grams per square centimeter second). The model considers the plasma to be a perfect gas and the impedance is given by,

$$\frac{2}{Z} = \frac{1}{Z_1} + \frac{1}{Z_2} \tag{4.2}$$

Where Z_1 and Z_2 represent the shock impedance of the target material and the confining medium respectively.

As the shockwave propagates into the solid target, the onset of plastic deformation begins when the peak pressure is greater than the Hugonoit elastic limit (HEL) of the target material and induces residual stresses throughout the affected depth which can be expressed by:

$$HEL = \frac{1-\nu}{1-2\nu}\sigma_Y^{dyn} \tag{4.3}$$

Where ν represents Poison's ratio and σ_Y^{dyn} is the dynamic yield strength at a high strain rate.

2. Material and methods

2.1 Materials

Nanodiamond powders were procured from a company in Kharkiv, Ukraine, SPE SINTA Ltd. (sinta1@yandex.ru) which are mass produced by the detonation of explosives (e.g. TNT and RDX mixture) in a closed chamber during less than a microsecond when both pressure and temperature are high, i.e. over 20 GPa and 3273 K. Nanodiamond particles exhibited a very narrow size distribution, i.e. from about 4 nm to about 8 nm. Moreover, these nanodiamond contained carbon irons, bulky balls (C60), layered shells, amorphous carbon and metallic impurities for a total of less than 10 wt%. It may be noted that nanodiamond has superior properties than single and polycrystalline diamonds due to its large surface area-to-volume ratio and unique electronic structure. Unlike single crystalline diamond, nanodiamond is extremely hard without sharp corners. Polycrystalline cubic boron nitride (PcBN) blanks with a nominal diameter of 50 mm (Grade HTM), received from Diamond Innovations, Inc. (Ohio, USA), consisted of 0.8 mm thick PcBN layer bonded to a tough 0.8 mm thick tungsten carbide (WC-13% Co) substrate. The PcBN layer is composed

of 2 μm size cBN particles embedded in a TiN matrix. The composition of PcBN is 50% cBN, 45% TiN and 5% AlN by volume.

2.2 Pulsed laser drilling of PcBN

A Q-switched Nd:YAG laser at a wavelength of 1064 nm (near infrared) and pulse width of 10 ns was employed. The focused laser beam with an average power of 4 W, spot size of 0.4 mm and pulse repetition rate of 10 Hz was applied to drill blind holes at the PcBN substrate which was mounted on a X-Y positioning table and moved at a speed of 0.12 mm/sec (no overlap of holes). The holes had an average diameter of 0.1 mm and depth of 180 μm. Following drilling, the holes were cleaned using acetone in an ultrasonic bath to remove the recast layer.

2.3 Laser Shockwave Sintering

The holes in PCBN were dry filled with nanodiamond powders and then sprayed with black paint as an absorptive layer, as well as covered by 1 mm thick fused quartz as a transparent overlay. The laser beam with an average power of 0.5 W was defocused to a spot size of approximately 1.0 mm in diameter on the PCBN surface to prevent the nanodiamond powders from burning while the pulse repetition rate was kept at 1 Hz. The number of shocks for each hole ranged from 1 to 5 times; each time, a new sacrificial layer of black paint was sprayed. The microscope images of blind holes with and without filled nanodiamond powders are shown in Fig.4.2. The pulse energy Q_L, is established as a function of average power, P_a and repetition rate, R, using:

$$Q_L = \frac{P_a}{R} \tag{4.4}$$

The peak power density is calculated as a function of pulse energy, *E*, pulse width, *t*, and beam area *A*, using:

$$I_P = \frac{E/t}{A} \tag{4.5}$$

The calculated peak power density was 6.37 GW/cm^2 at 1 Hz.

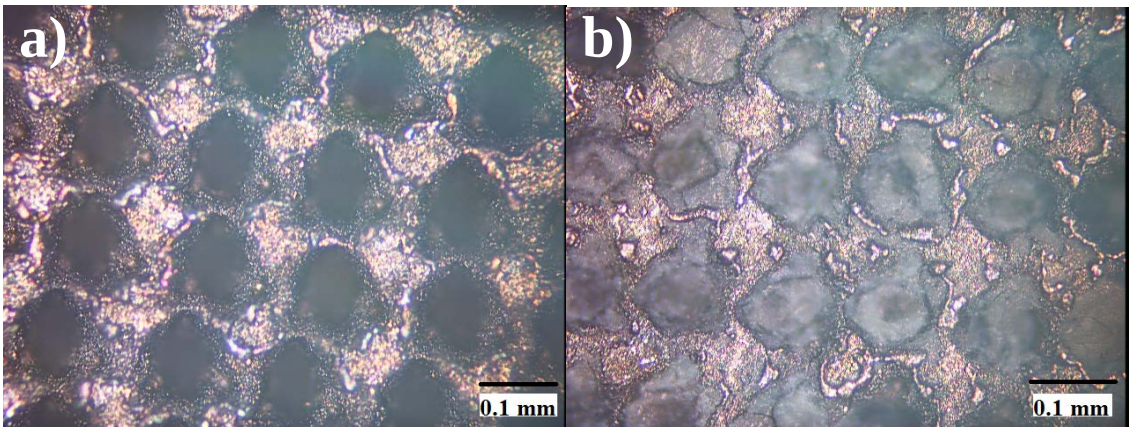

Figure 4.2 Microscope images of (a) blind holes and (b) holes dry filled with nanodiamond powders and laser shocked one time

2.4 Test and Characterization

A Tukon micro-hardness tester using a diamond pyramid indenter was used to measure the Vicker's hardness at 1 kgf load and 10 s hold time. A Raman visible spectroscope (532 nm using Ar-ion laser) was used to identify the phase transitions for Raman shift range of 900 to 1800 cm^{-1}. An optical microscope was utilized to characterize and measure the depression depth which is defined as the distance between the surfaces of PCBN and nanodiamond powder compact after LSS. Transmission electron microscopy (TEM) was employed for determining the as-received nanodiamond powder grain size and its uniformity. Scanning electron microscope (SEM) was used to examine the microstructural changes associated with multiple shocks.

3. Finite element simulation

3.1 LSS Model Formulation

FEM software ABAQUS™ was used to analyze the deformation in LSS. ABAQUS/Explicit is used for the high energy dynamic events in progress of LSS while ABAQUS/Standard is used to obtain residual stresses of steady state and hardness information through reading the files created from ABAQUS/Explicit. The FEM analysis procedure is presented in Fig.4.4. The combined procedure takes the advantage of performing both explicit and implicit analysis. Temperature effect is neglected since laser shockwave is not a thermal process. This process involves energy absorption by the black paint, followed by its evaporation and subsequent energy dissipation through nanodiamond /PcBN substrate. Heat capacity, density, molar mass and latent heat of vaporization of the black paint (Xylene) were obtained from the materials handbook [112] and used for the calculation of the paint's laser energy absorption. The measured thickness of the black paint is 17 μm, using a microscopic technique with a resolution of 1 μm. For each laser shocking pulse, the total input pulse energy is

$$E = \frac{P_a}{R} = \frac{0.5W}{1Hz} = 500mJ \tag{4.6}$$

The defocused spot size is 1 mm, so the volume of evaporating black paint under each pulse is

$$V = \frac{\pi(10^{-3}m)^2}{4} \times (17 \times 10^{-6}m) = 1.3345 \times 10^{-11}m^3 \tag{4.7}$$

The mass of black paint is

$$m = \rho V = (864kg/m^3)(1.3345 \times 10^{-11}m^3) = 11.53 \times 10^{-9}kg \tag{4.8}$$

If Q is taken as energy absorption by Xylene then, Q can be calculated by the following equations according to the procedure shown in Fig. 4.3:

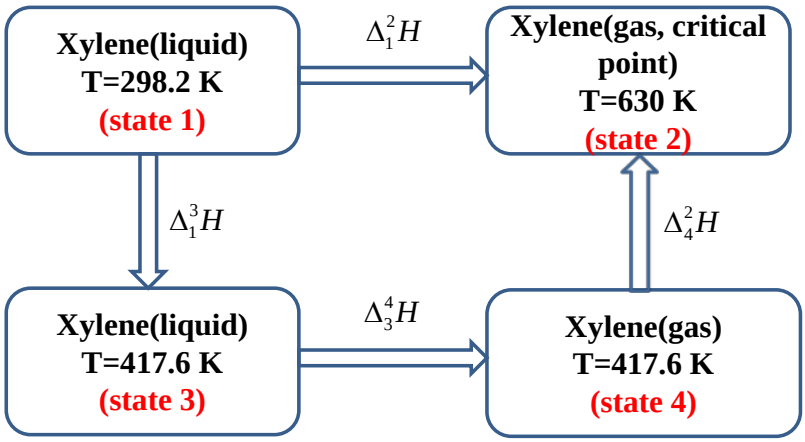

Figure 4.3 Thermal analysis procedures for energy absorption by Xylene

$$\Delta_1^3 H = (1771 J/K\cdot kg)\times(11.53\times10^{-11} kg)\times(417.6-298.2)K = 1.612\times10^{-3} J = 1.612 mJ$$

$$\Delta_3^4 H = \frac{11.53\times10^{-6} g}{106.17 g/mol}(36.82 kJ/mol) = 4.0\times10^{-3} J = 4.0 mJ$$

$$\Delta_4^2 H = (-15.84+0.6\times630-3.441\times10^{-4}\times630^2+7.523\times10^{-8}\times630^3)\frac{J}{K\cdot mol}\times\frac{11.53\times10^{-6} g}{106.17 g/mol}\times(630-417.6)K$$

$$= 244.4 J/K\cdot mol\times\frac{11.53\times10^{-6} g}{106.17 g/mol}\times(212.4)K = 5.64\times10^{-3} J = 5.64 mJ$$

$$Q = \Delta_1^2 H = \Delta_1^3 H + \Delta_3^4 H + \Delta_4^2 H = (1.612+4.0+5.64)mJ = 11.25 mJ \quad (4.9)$$

The remaining 489 mJ of pulse energy will be trapped by the plasma formed at the glass/substrate interface. Due to the confined nature of the plasma, the effect would be more significant that a large fraction of energy (80%-90%) is used for the ionization of plasma under these conditions of irradiation [66]. Based on this reference, we believe that the absorption is 80% of the energy. This implies a residual energy of 98 mJ for dissipation into the substrate. It can be assumed that in a spot size area, the components ratio of PcBN and nanodiamond plus carbon derivative composite is 1:1. The thermal conductivity of substrate can then be averaged. The thermal skin thickness can be calculated by following equation [113]:

$$z = 0.5\sqrt{4\kappa t} = 0.5\sqrt{4\times4.8\times10^{-4} m^2/s\times10 ns} = 2.19\mu m \quad (4.10)$$

Where z is the thermal penetration depth, κ is thermal diffusivity and t is laser pulse width.

From the above equation, we can conclude that thermal penetration depth mainly depends on laser pulse width. The laser pulse width is only 10 ns, which means continuing heat transfer from the laser is too short; as a result, even all the laser energy is absorbed by the substrate, the thermal skin thickness would still be small. Also, due to the rapid dissipation of laser shockwaves, it could be assumed that the contact between the nanodiamond powders and surrounding cavity wall is frictionless, under which condition, it can be expected that the density distribution is homogeneous.

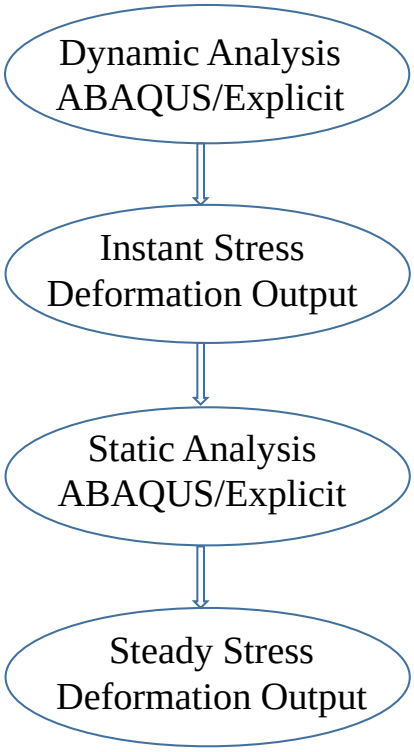

Figure 4.4 FEM analysis procedures for LSS

The high amplitude, very short duration pressure pulse of the shockwave is one of the key parameters related to the effects of LSS. Because of the presence of the confinement layer [40], the duration of pressure pulse can be increased 2~3 times than the duration of the

laser pulse. Consequently, the duration of shockwave is set as 30 ns which are 3 times that of laser pulse duration. For simplicity, the pressure versus time is assumed to be quadratic

$$\frac{P}{P_{\max}} = (30 - t)t/225 \tag{4.11}$$

Where P is the pressure applied on the top surface of the sample, $P_{\max}$ is the peak pressure of 2.8 GPa for the power density used in this work [114], and *t* is the time in nanoseconds. The spatial distribution of pressure within the radius of the beam is usually Gaussian, but we have assumed it to be uniform because the radius of nanodiamond sintered area is much smaller than the radius of beam. Since plastic deformation lasts longer than the pressure pulse [109], we set the time for solving dynamic process at 300 ns.

Elastic-plastic behavior of nanodiamond powder is considered. The increment in mechanical deformation can be decomposed linearly into elastic and a plastic part described by [115]:

$$d\varepsilon^{tot} = d\varepsilon^{el} + d\varepsilon^{pl} \tag{4.12}$$

Where $\varepsilon^{tot}, \varepsilon^{el}, \varepsilon^{pl}$ are total, elastic and plastic strains, respectively. The linear elastic behavior is governed by Hooke's law. For isotropic materials, elastic properties consist of Young's modulus *E* and Poisson's ratio *v*. The clay plasticity model [116] which originates from soil mechanics due to the similarity of powders to soil is used for modeling the inelastic deformation with volume change assuming the powder to be a continuum [117-119]. The model is based on the yield surface, which can be expressed by:

$$\frac{1}{\beta^2}\left(\frac{p}{a} - 1\right)^2 + \left(\frac{q}{Ma}\right)^2 - 1 = 0 \tag{4.13}$$

Where p is the equivalent stress defined below, q is von Mises stress, M, β (=1), and a describe the size and shape of the yield surface. For uniaxial cylindrical compaction of powders with walls having $\sigma_r = \sigma_\theta$ [120]:

$$p = \left(\sigma_a + 2\sigma_r\right)/3, \quad q = \left|\sigma_a - \sigma_r\right| \tag{4.14}$$

Where σ_a, σ_r, σ_θ are axial, radial and tangential stresses, respectively. A linear relationship between the axial stress and radial stress is given as [121]:

$$\sigma_r = k\sigma_a \tag{4.15}$$

Where k is the stress transmission ratio ($0 < k < 1$). The constant M in equation (8) can be calculated from [122]:

$$M = \frac{q}{p} = \frac{9}{2+4k} - \frac{3}{2}, 0 < k < 1 \tag{4.16}$$

Assume $k = 0.618$ [123], then $M \approx 0.5$

The constant a is given by [120]:

$$a = \frac{p_c}{\left(1+\beta\right)} \tag{4.17}$$

Where p_c is hydrostatic compression yield stress (or the first invariant of stress tensor) that can be related to the corresponding volumetric plastic strain, ε_{vol}^{pl} [115]:

$$p_c = p_c(\varepsilon_{vol}^{pl}) \tag{4.18}$$

Then the yield surface grows in size with the increase of compressive volumetric plastic strain, ε_{vol}^{pl}, which can be calculated from the volume change (porosity ratio or relative density) :

$$\varepsilon_{vol}^{pl} = -dV/V = \ln\left(\rho/\rho_0\right) = \ln\left(V_0/V\right) \tag{4.19}$$

Where ρ_0, V_0 are the initial bulk density and volume, $\rho = \rho_0 \exp\left(\varepsilon_{vol}^{pl}\right)$, $V = V_0 \Big/ \exp\left(\varepsilon_{vol}^{pl}\right)$ are the density and volume corresponding to a specific volumetric plastic strain. Compressive strains are assigned positive values here.

Plastic flow is normal to the yield surface. During LSS, the powder compacts become harder and harder by reducing the pore volume; this makes it difficult to compress further and requires extreme force to rearrange the particles. The initial state of the nanodiamond as loose powder is strain-free and stress-free. The hardening law can be expressed as an exponential function:

$$p_c = H\left(\exp\left(\varepsilon_{vol}^{pl}\right) - 1\right) + \alpha \tag{4.20}$$

Where H is the hardening coefficient, α is a constant with small value (assumed to be 0.03 GPa) to ensure that the powder has no plastic behavior when $\varepsilon_{vol}^{pl} = 0$; this represents the loose state [124]. H is evaluated as follows: During LSS, the powder is stressed and deformed in a dynamic way in which case static stress-strain relationship is invalid to characterize the material response [125]. Because of the high strain rate associated with short duration of pressure pulse and work hardening effect the yield stress can be increased by 40%~200% [126]. The dynamic yield strength σ_Y^{dyn} can be calculated from the Hugoniot elastic limit (HEL) as follows:

$$P_c = \sigma_Y^{dyn} = \frac{1-2\nu}{1-\nu} HEL \tag{4.21}$$

Where ν represents Poisson's ratio (0.07), and assumed $HEL = 45$ GPa for the nanodiamond and carbon derivative composite [127, 128]. The calculated $\sigma_Y^{dyn} = 41.6$ GPa can be regarded as the hydrostatic compression yield stress when full densification is achieved and the

volumetric plastic strain is $\varepsilon_{vol}^{pl} = \ln \chi = \ln\left(\rho_f / \rho_0\right)$, where ρ_f is the full density of this material, ρ_0 is the original density of the green powder compact, and χ is the density ratio. Since the powder compact contains porosity of about 40%, then $\chi = 1.67$. Substituting these into the Hardening Law Equation (20), the hardening coefficient is $H \approx 62$ GPa.

The application of the constitutive law of powders is quite difficult [115] because of the fluid-like behavior and loose aggregation of discrete particles [120, 129]. Although the constants in clay plasticity model could be dependent on density or load history [130], we have assumed these to be independent because it has been revealed that the final green density distribution is determined by the parameter of hardening law rather than the shear failure surface [131]. We have also validated this assumption by a comparison between simulation and experimental results.

Table 4.1 lists the material properties of the powder compact required for the FEM simulation. Here the Young's modulus is adjusted to 732 GPa using the rule of mixture as $0.6E_{Bulk} = 0.6 \times 1220\ GPa = 732\ GPa$ [70].

Table 4.1 Mechanical properties of nanodiamond and carbon derivative composite

Properties	Value	Unit
Density, ρ	3455	kg/m^3
Poisson's ratio, ν	0.07	
Young's modulus, E	732	GPa
Hugoniot elastic limit *(HEL)*	45	GPa

A stability condition in ABAQUS/Explicit using finite difference method is required for accurate results [132]. The stable time increment can be calculated by

$$\Delta t_{stable} = L\sqrt{\rho / E} \tag{4.22}$$

Where L is the element length, whose smallest value is 0.6 μm. The stable time increment should be on the order of the magnitude of 10^{-11} s, which is reasonable when compared with simulation time of other researcher's laser induced plasma shockwaves [133, 134]. For Vickers indentation hardness simulation, an axisymmetric model with a rigid conical indenter having a half angle of 70.3º was chosen [135]. Under such condition, the projected area of the conical indenter is the same as that of the Vickers indenter.

3.2 Finite element modeling

A cylinder sample with the diameter of 0.1 mm and depth of 0.18 mm is used. Since this cylinder is subjected to an axisymmetric uniform circle pressure pulse, an axisymmetric model with cylindrical coordinates *1-2-3 (1 radial, 2 axial, 3 tangential)* is established. The axisymmetric boundary conditions (zero radial displacement) are applied on the symmetric axis, while bottom surface is fixed and circumferential surface is only allowed to move along the load direction. The model consists of CAX4R elements (Continuum, axisymmetric, 4 nodes, reduced integration), with the use of a BIAS function in z-direction to allow a denser mesh near the top surface with coarse mesh near the bottom surface. 40200 axisymmetric 4-node elements with reduced integration were used to mesh a $\Phi 0.1 \times 0.18$ mm body as shown in Fig.4.5. The mesh is swept to one quarter of the configuration.

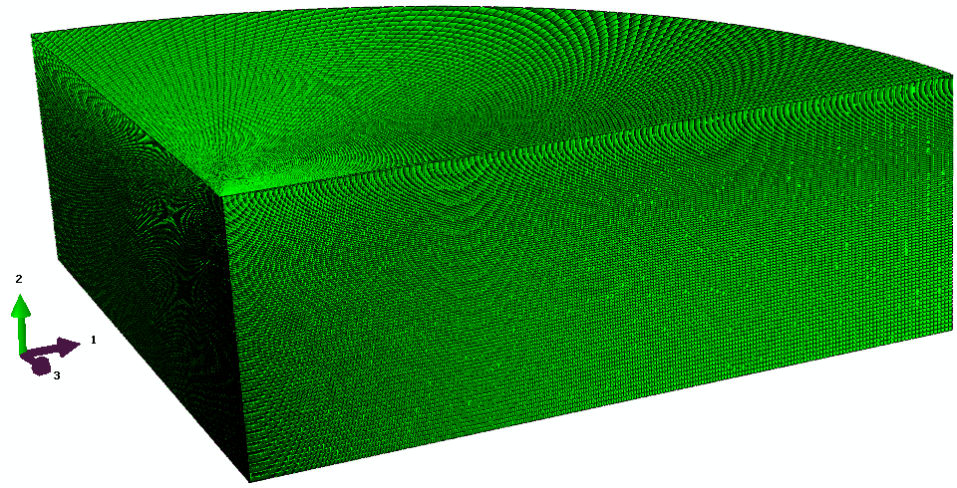

Figure 4.5 Finite Element model from ABAQUS™

4. Results and discussion

4.1 Experimental Results

The average hardness of nanodiamond powder compact by one time LSS is 30.4 GPa, and increased significantly to 36 GPa when shocked two times. However this trend gradually leveled off with multiple times of LSS, as shown in Fig.4.6, because the microstructural refinements as well as the rate of densification and work hardening tend to decrease with multiple shocks. The hardness is about 30% of that reported for high-temperature, high-pressure fully compacted nanodiamond [108].

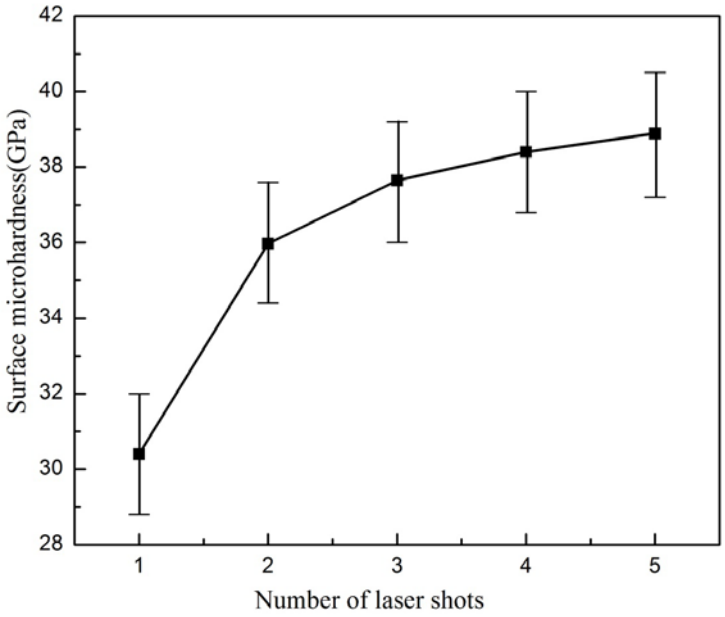

Figure 4.6 Hardness results of nanodiamond compact by multiple LSS

Figure 4.7a shows a typical Raman spectrum of unprocessed nanodiamond powder with three characteristic peaks centered at 1133, 1363 and 1589 cm^{-1}. According to Ferrari and Robertson [136], the Raman spectrum of a typical nanodiamond consists of a small diamond peak at 1332 cm^{-1} and four extra features at 1150, 1350, 1480 and 1550 cm^{-1}. The peaks at 1350 and 1550 cm^{-1} are the D and G peaks of amorphous carbon. The peak at 1150 cm^{-1} has been attributed to nanocrystalline diamond. The deviations in our Raman spectrum (Fig.4.7a) are caused by the presence of impurities such as carbon and OH-groups. Figure 4.7b shows LSS nanodiamond for one and two shocks. Two new peaks were identified: one is around 1100 cm^{-1} which is a downshift from 1150 cm^{-1} possibly caused by residual stresses; the other is a well-defined peak at 1600 cm^{-1} indicating the formation of nanocrystalline graphite [137]. Such changes in the phase and residual stress account for increased micro-hardness of the nanodiamond powder compact.

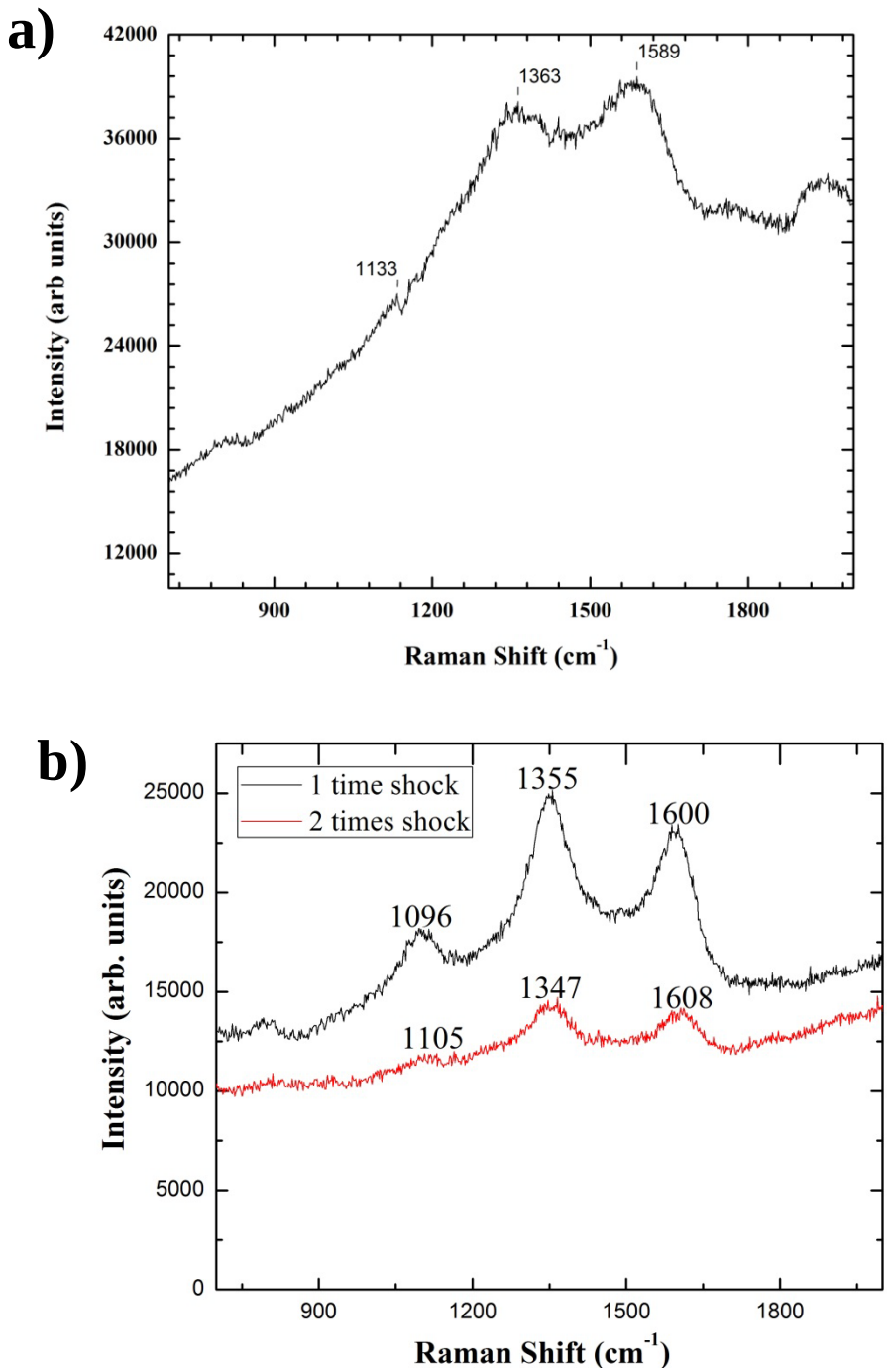

Figure 4.7 a) Raman spectrum of unprocessed nanodiamond powder. b) Raman spectrum of LSS processed nanodiamond powder

Figures 4.8a and 4.8b are TEM micrographs of the nanodiamond. The insert in Fig.4.8a is a selected area diffraction pattern (SADP). The micrographs demonstrate the uniformity of the particles. Fig.4.8b is at a higher magnification of an area different than

Fig.4.8a. The grain size determined is 7.35+/-1.25 nm and 8.44+/-1.93 nm from two different areas.

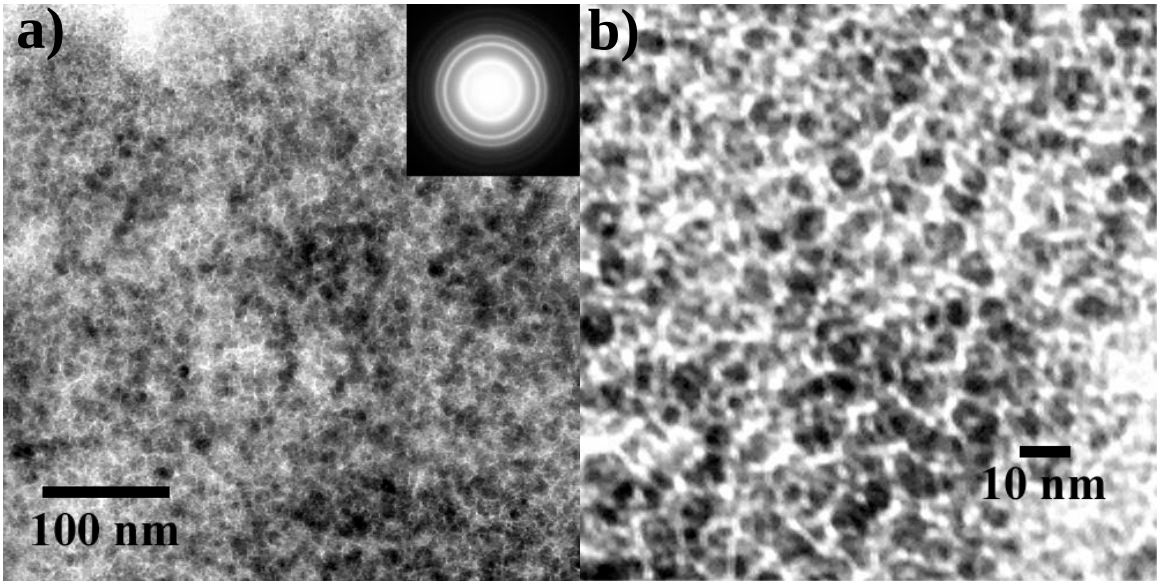

Figure 4.8 TEM micrographs of the as-received nanodiamond powder. Figure 4.8a is a lower magnification with a selected area electron diffraction pattern in the upper RHC. The clear concentric rings are characteristic of a nanophase. Figure 4.8b is a high magnification micrograph showing the rounded nature of the grains.

SEM images of LSS nanodiamond as a function of number of shocking times are presented in Fig.4.9. LSS nanodiamond for one and two shocks revealed inhomogeneous microstructures as well as many pores and loose particles (Fig. 9a, b). In contrast, LSS nanodiamond for three or more shocks exhibited more tight and well-densified microstructures with deformation lines, as shown in Figs.4.9c, d and e. Overall there is an improvement in densification with multiple shocks. However, there are cracks across part of LSS zones and these cracks are branched as a result of tensile residual stresses. Figure 4.10 shows that the depression depth, a measure of densification, increases with multiple times of LSS; this is attributed to continuous compression and plastic deformation of the powders.

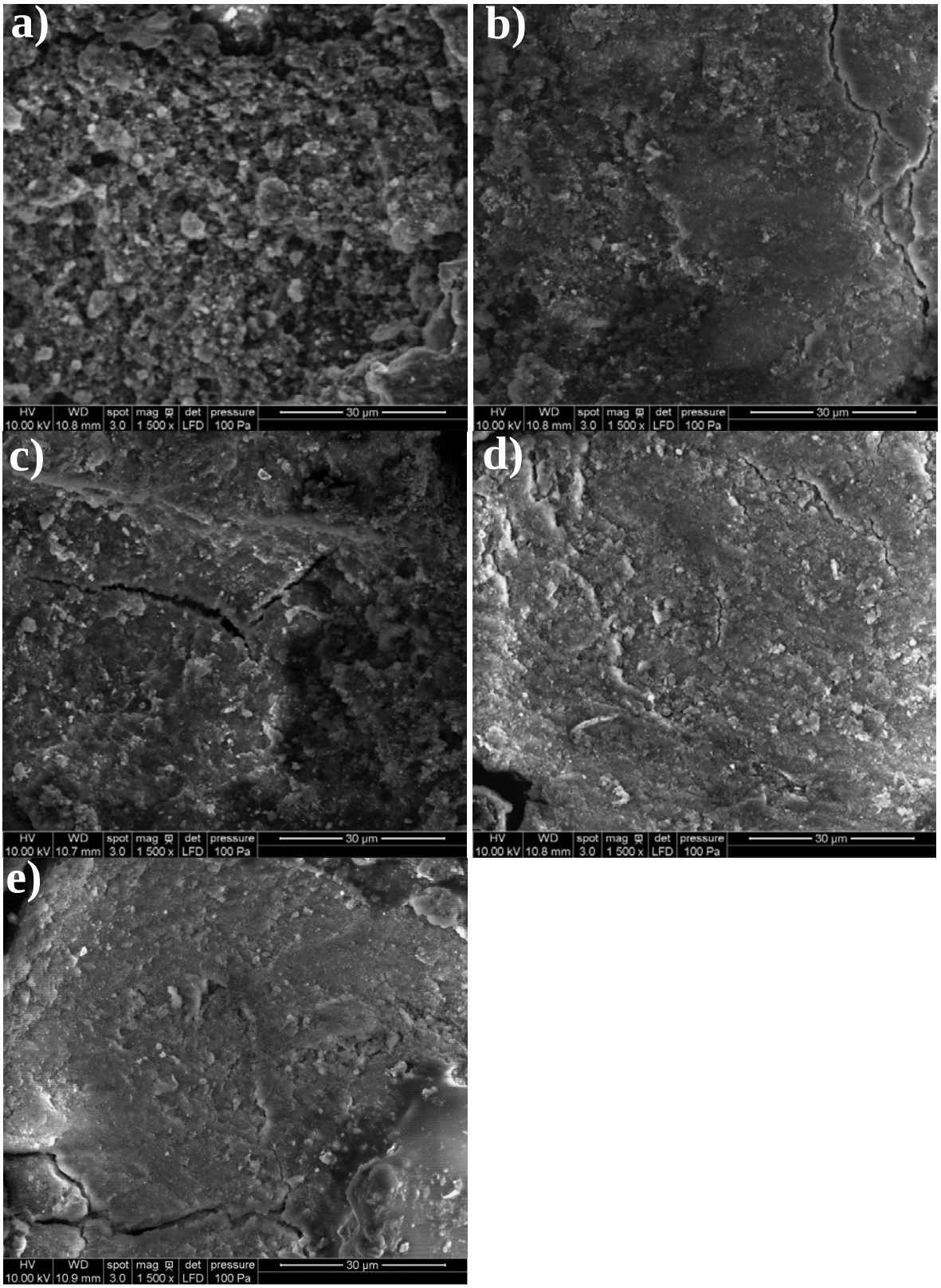

Figure 4.9 SEM images of nanodiamond compact by LSS of multiple times: a) one time; b) two times; c) three times; d) four times; and e) five times.

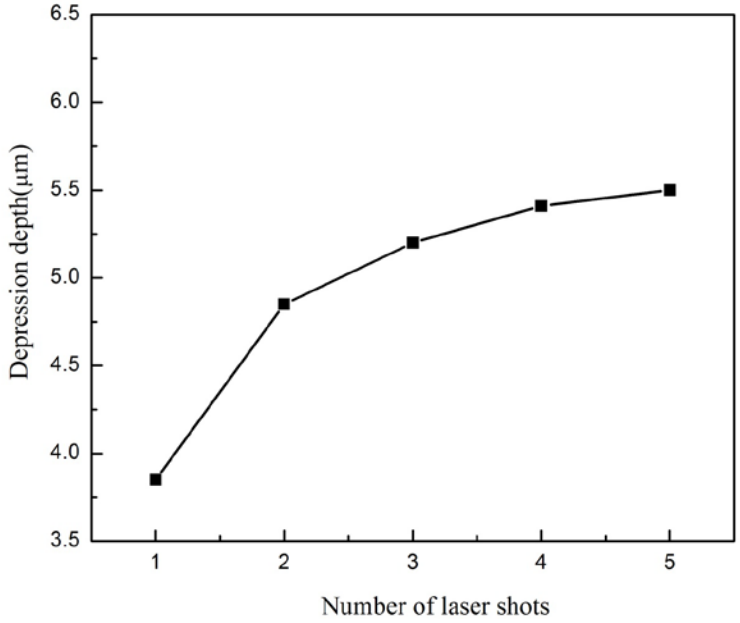

Figure 4.10 Depression depth measured by optical microscope

4.2 Simulation results

4.2.1 Dynamic stress state

The dynamic stresses, σ_{radial} and σ_{axial}, vary along the depth and time by single and multiple laser shocks are presented in Fig. 4.11. The magnitude of axial and radial stresses at 15 ns by one laser shock are around 2800 MPa and 2550 MPa respectively, which is about 15% higher than that at 30 ns, 17% higher than that at 60 ns and much higher than that at 90 and 120 ns. The stress attenuation with time is attributed to the dissipation of laser as well as by plastic deformation and energy absorption within the nanodiamond powder compact. The dynamic stress change after five laser shocks is similar, as shown in Fig.4.11b, but both the axial and radial stresses propagate much deeper when compared to that of the single shock since the nanodiamond powder is compressed more tightly and less energy is absorbed by loose powder. The radial stress (σ_{radial}) is more important in LSS because it ultimately leads to the residual compressive stress.

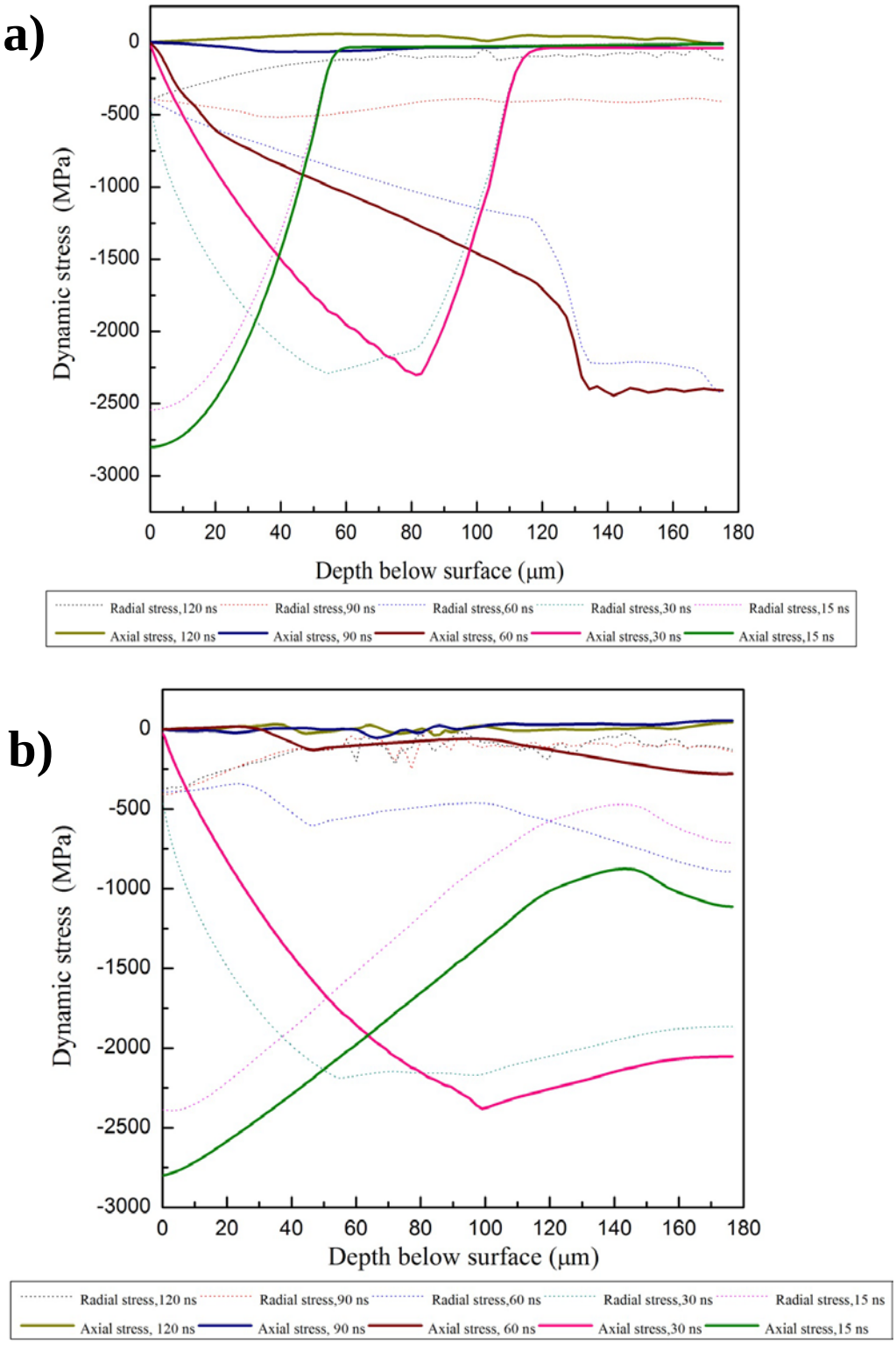

Figure 4.11 a) Propagation of dynamic stresses, σ_{radial} and σ_{axial} in depth at different time under single laser shock. b) Propagation of dynamic stresses, σ_{radial} and σ_{axial} in depth at different time under five laser shocks

4.2.2 Residual stress field from static analysis

Figure 4.12 presents the contours of the von Mises residual stress distributions. The average residual stress is much higher for five shocks compared to a single shock due to the increased depth of stress propagation.

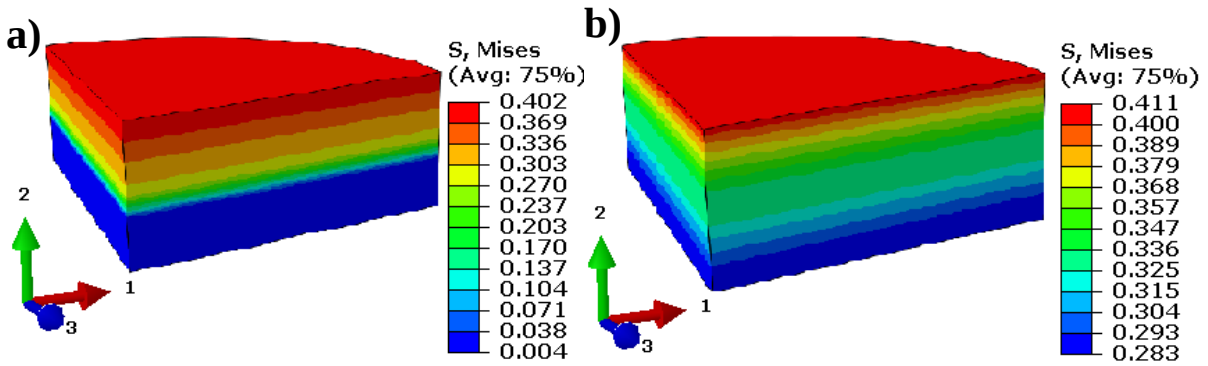

Figure 4.12 Contour of von Mises residual stress distribution by LSS: a) single shock; b) five shocks

Figure 13 shows the contours of radial and axial components of the residual stress field for single and multiple shocks. For the radial component, a large compressive stress gradient exists between the top and bottom surfaces in the case of a single shock. With the increasing number of shocks, the stress gradient tends to diminish due to continuous, non-uniform plastic deformation. For the axial component, tensile residual stresses were noted in both top and bottom surfaces for a single shock while a smaller tensile residual stress field was mostly seen on the top surface with increasing shocks; this is attributed to the reversing yielding effect due to the interaction of the various stress waves in the material.

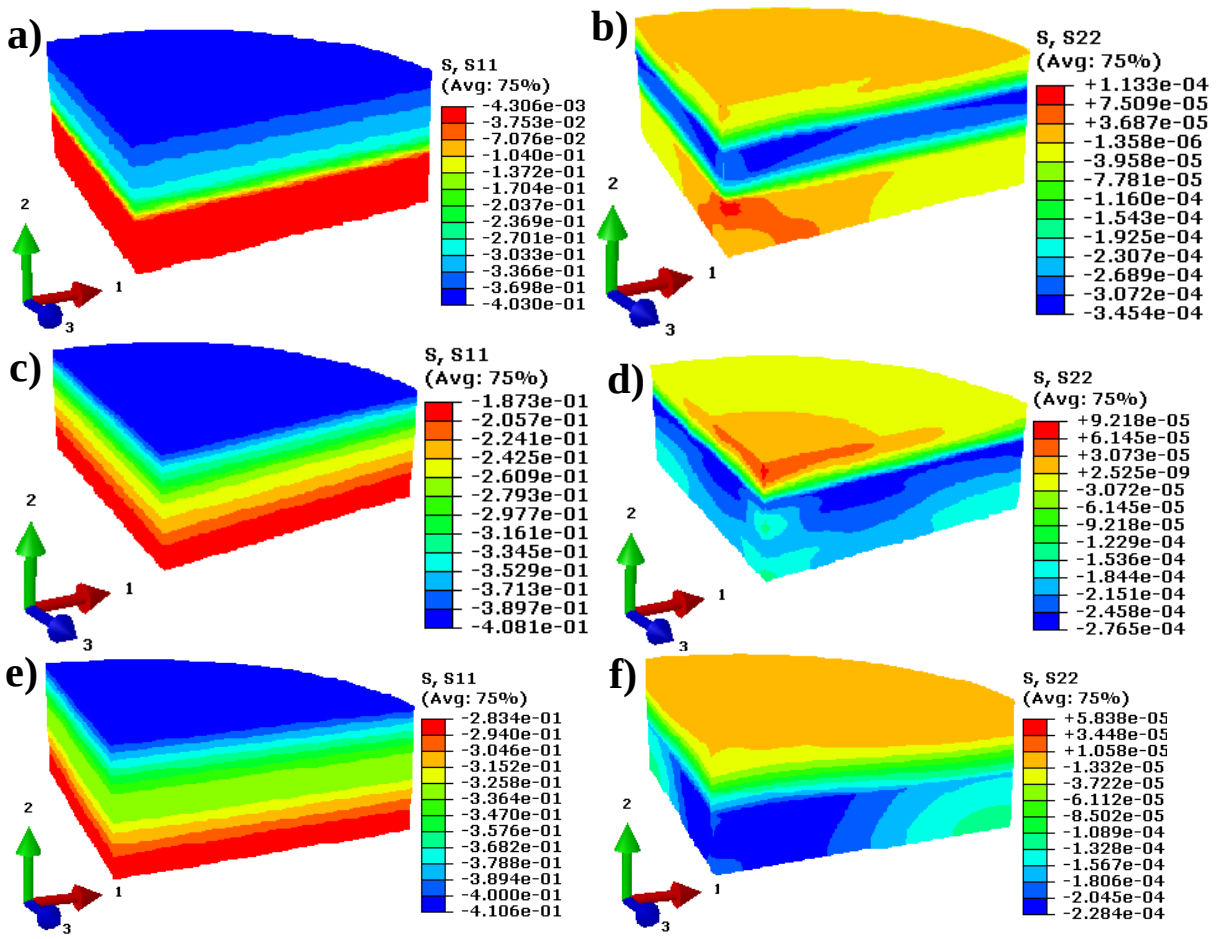

Figure 4.13 Contour of residual stress field by multiple LSS: a), c) and e) radial component of residual stress in GPa by LSS for 1, 3 and 5 shocks; b), d) and f) axial component of residual stress in GPa by LSS for 1, 3 and 5 shocks

Fatigue performance of LSS parts is generally sensitive to radial (compressive) component of residual stress field. Figure 4.14 summarizes the surface and in-depth residual stress fields of the radial component resulting from multiple LSS. It is clear that multiple shocks increase the magnitude of compressive residual stresses on the surface as well as driving them deeper into the nanodiamond compact. With increasing number of shocks, the maximum compressive residual stress remains approximately uniform on the surface of the shocked region. The saturation of the residual stress and plastically affected depth, marked in

Fig.4.14b, indicates that work hardening of the material progressively increased along the depth.

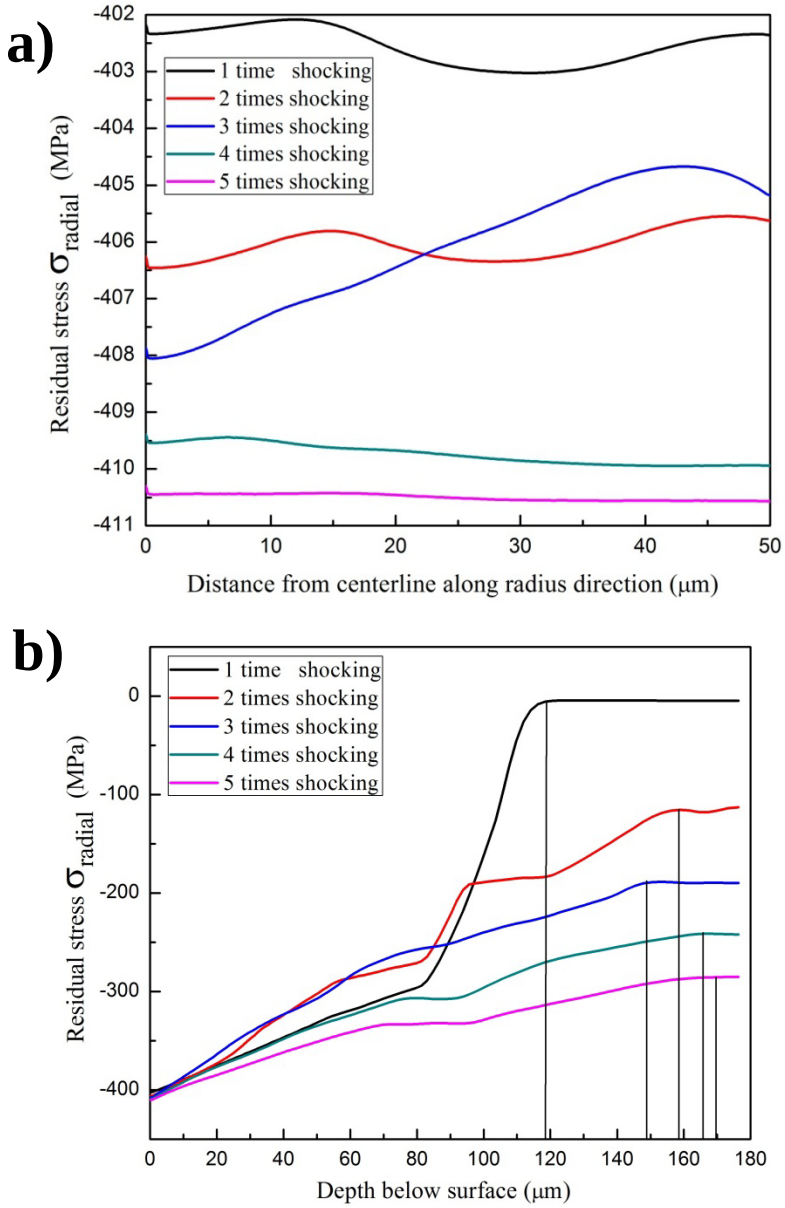

Figure 4.14 Radial component of residual stress distribution after single and multiple LSS. a) Radial component of residual stress distribution on top surface along radial direction. b) Radial component of residual stress distribution along depth after single and multiple LSS

4.2.3 Densification and surface deformation

Figure 4.15 depicts the compression ratio of the powders, given by $k_r=\rho/\rho_a$, where ρ_a is the apparent density of the loose powder and ρ is the apparent density of the compacted powder. The increase in compression ratio is very small (1.04) compared to the traditional powder metallurgical methods where the compression ratio can reach 1.80; this could be explained by the absence of binder, no heating and the short duration of compaction. Figure 4.15 reveals that the compression ratio does not significantly change at the top layers with increasing number of shocks while it increases in the bottom layers. The compaction mechanism in LSS consists of partial aggregation of loose powders, repacking of the powders into a better arrangement and deformation of particles that reduce the pore volume and increase the number of contact points. However there is no crushing, necking and welding of particles. In order to increase the densification substantially, large number of shocks coupled with a suitable binder is deemed necessary.

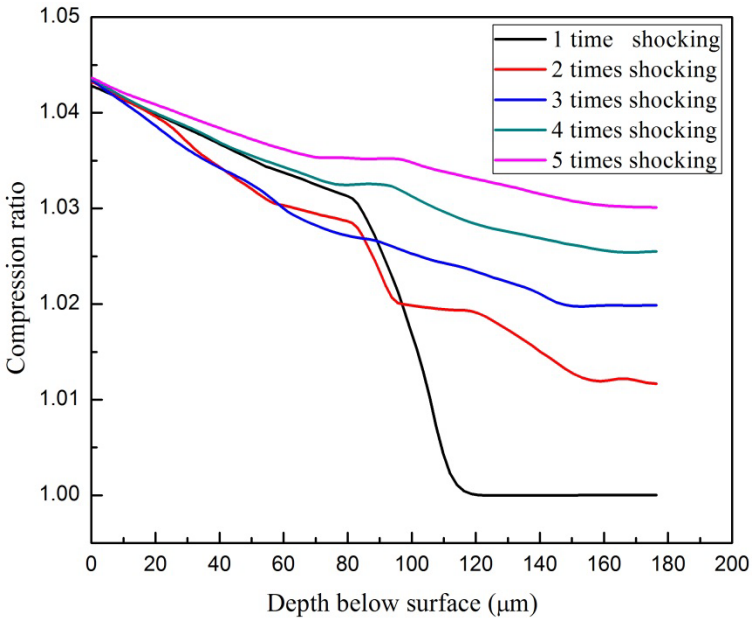

Figure 4.15 Distribution of compression ratio along depth

Figure 16 shows the FEM results of depression depth, a measure of densification. Overall, there is a strong correlation between FEM and experimental results which validates the FEM model. The simulation results for 1 to 3 times LSS agree better with experimental measurements compared to 4 and 5 times LSS; this could be explained by the assumption of frictionless contact in the simulation.

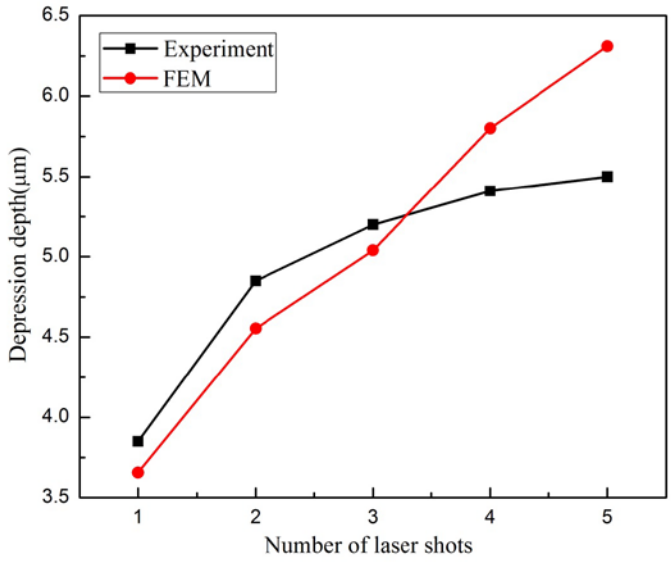

Figure 4.16 Increase of depression depth by multiple LSS

4.2.4 Surface Micro-hardness

The indentation hardness is calculated by the indentation load divided by the actual contact area at the maximum indentation depth. The absolute value of the indentation hardness from the simulation does not agree with the experimental results since the indentation load applied in the simulation cannot be as large as that in experiments due to numerical difficulties in the simulation. The indentation load of 0.0228 N is used. Simulated hardness normalized by the value under a single shot is shown in Fig.4.17, the surface micro-hardness is significantly increased from one to two shots and is gradually saturated by five shots; a rather good similar trend can be found between FEM and experimental results. The

reason can be mainly explained by the great densification as well as the increase in residual stress in the initial stage, while saturation is gradually achieved due to work hardening.

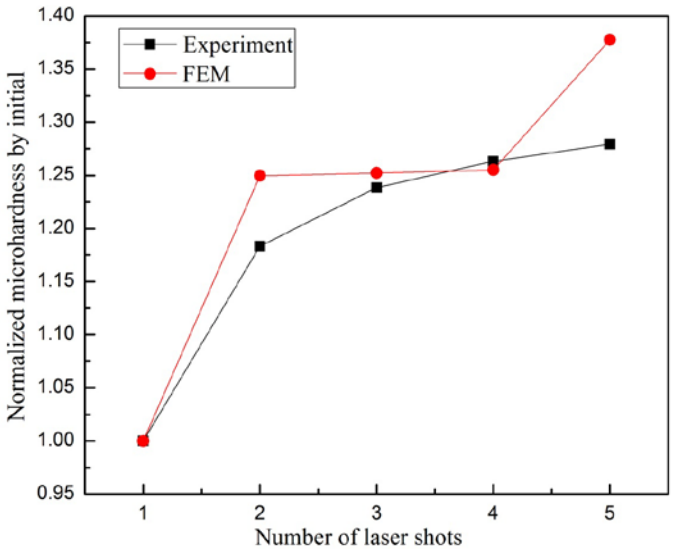

Figure 4.17 Hardness results of experiment and FEM by multiple LSS

5. Conclusions

Laser shock sintering experiments and finite element simulations using ABAQUS were carried out to investigate the compaction of nanodiamond powders. Experimental results showed phase transition, partial densification and increased hardness with multiple shocks. Axisymmetric FEM model calculations of densification correlated well with the experimental results. Residual stress analysis by FEM showed the presence of compressive residual stresses that tends to increase with depth due to multiple shocks.

Acknowledgements

This material is based upon work supported by the National Science Foundation under Grant No. CMMI-1029072.

CHAPTER 5. NANODIAMOND COATED CARBIDE TOOL PERFORMANCE INVESTIGATION

In this chapter, laser shockwave sintering of nanodiamond powders coated in carbide tool inserts was processed using a 1064 nm, 10 ns Q-switched Nd:YAG laser with a peak power density of 6.37 GW/cm^2 ; meanwhile, tool wear and life studies were investigated.

1. Material and experiment details

In layer manufacturing processes on carbide tool inserts, the substrate material, carbide insert of ISO designation SPGN090308 H13A, WC-6%Co, was supplied by Grainger, Inc. The tool geometry is square with a positive rake angle and nose radius of 0.0315 inch. Nanodiamond (ND) powders were doped at the corner of crater and flank faces, as shown in Fig.5.1

Figure 5.1 Schematic of nanodiamond powders doped in carbide insert tool

First, the focused laser beam with an average power of 4 W, spot size of 0.4 mm and pulse repetition rate of 10 Hz was applied to drill blind holes at the corner of carbide insert crater and flank face, which was mounted on a X-Y positioning table and moved at a speed of 0.5 mm/sec (no overlap of holes). Then, the holes in carbide insert were wet filled with ND powders and a defocused laser beam with an average power of 0.5 W, spot size of

approximately 1.0 mm in diameter and pulse repetition rate of 10 Hz was applied for powders doping process, which was repeated 20 times.

In tool wear study, single-point turning tests were conducted. The lathe had the provision to keep the surface speed constant while the diameters are being reduced. The workpiece was a 7068 Aluminum bar with the diameter size approximately 3 inch and length of 12 inch. No coolant was used during the experiments. The speed and feed were kept constant throughout the experiments. The machining parameters are listed in Table 5.1. After each pass the tool was removed from the tool post. Because of the decrease in diameter, the average time taken for each pass varied. The flank wear was measured using Gartner Scientific toolmaker's microscope with a magnification of 30X. Tests were repeated twice. An optical microscope was utilized to characterize the crater wear and flank wear.

Table 5.1 Tool wear machining parameters

Feed	0.0014 in/min
Cutting speed	400 ft/min
Depth of cut	0.03 in
Cutting length	12 in

2. Results and Discussion

Fig.5.2 shows the progression of average flank wears with time for uncoated and coated carbide insert tools. For most wear curves, two regions of constant wear and accelerated wear can be found, which are chiefly determined by interplay among cutting forces, compressive stresses and temperatures. The constant wear region is caused by a reduction in cutting forces and stresses usually observed in the initial stages of cutting and attributed to the geometric conformity of the contacting surfaces. The accelerated wear is

essentially due to the substantial temperature rise in the cutting zone. In this curve, since it was recorded from starting point after 10 minutes, only accelerated wear can be clearly seen. The key result is that the nanodiamond doping enabled a reduction of more than 35% in flank wear, implying a marked improvement in tool life.

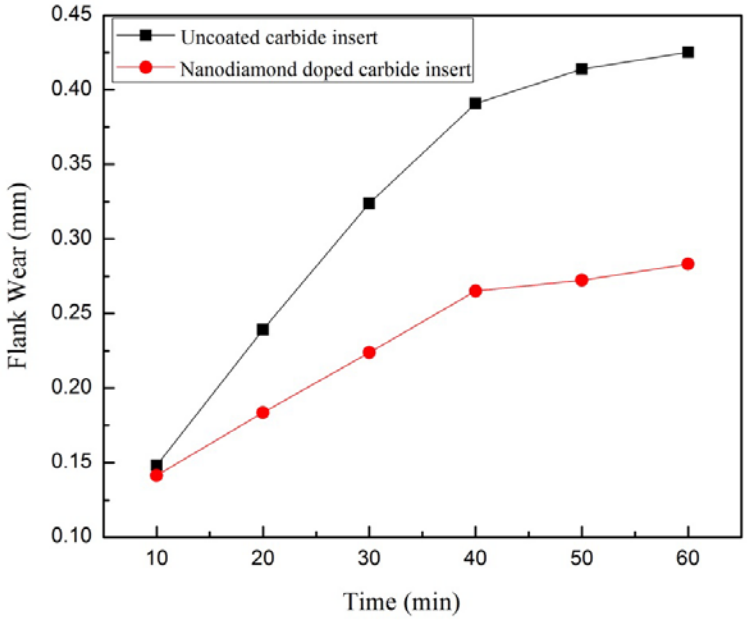

Figure 5.2 Flank wear vs. Time

SEM analysis of worn-tools revealed that different wear mechanisms are associated with coated and uncoated tools. In the case of uncoated tools (Figure 5.3a), large amount of wear debris and deformation are readily seen. The dominated wear mechanism is adhesion and material dissolution, as well as chipping and plastic deformation due to mechanical shock and thermal fatigue, especially the high positive rake angles of this carbide insert can also contribute to chipping. Figure 5.3b shows the ND doped worn-tool, in this case, it is clearly seen that adhesion and material dissolution was stopped by diamond enforcement phase.

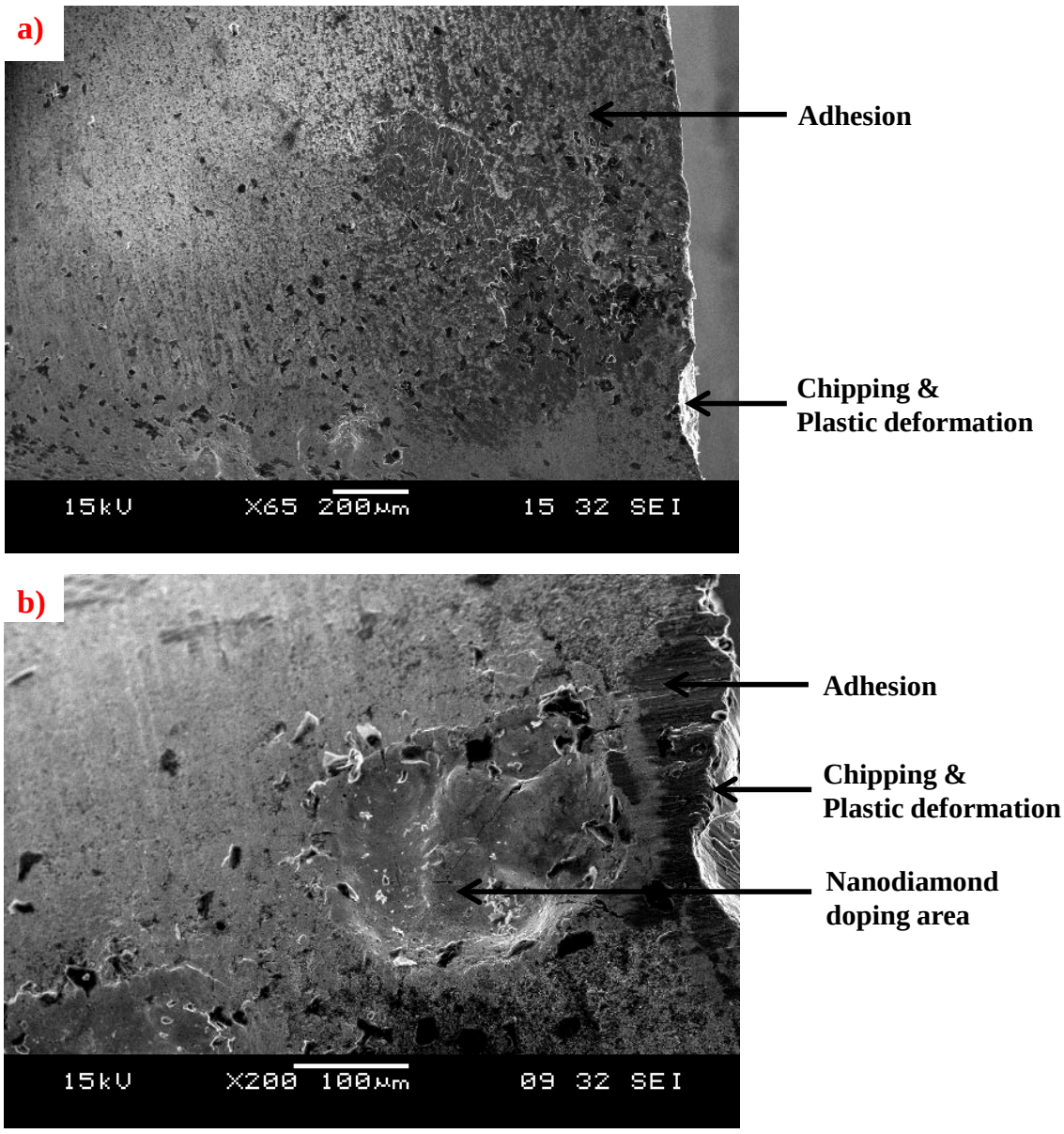

Figure 5.3 SEM image of flank wear on a) uncoated tool and b) nanodiamond doped tool

Microscope images of flank wear and crater wear were shown in Fig. 5.4. It is clearly to see that worn condition is much more serious for uncoated tool, and the flank face is pretty rough due to adhesion and material cold welding. While in the case of ND doped tool, flank wear is low and smooth, which can be explained that the high hardness of diamond withstood the high stresses developed in the cutting zone and rapid heat dissipation of diamond resisted the dissolution of WC in aluminum. The similar phenomenon can be found in crater wear.

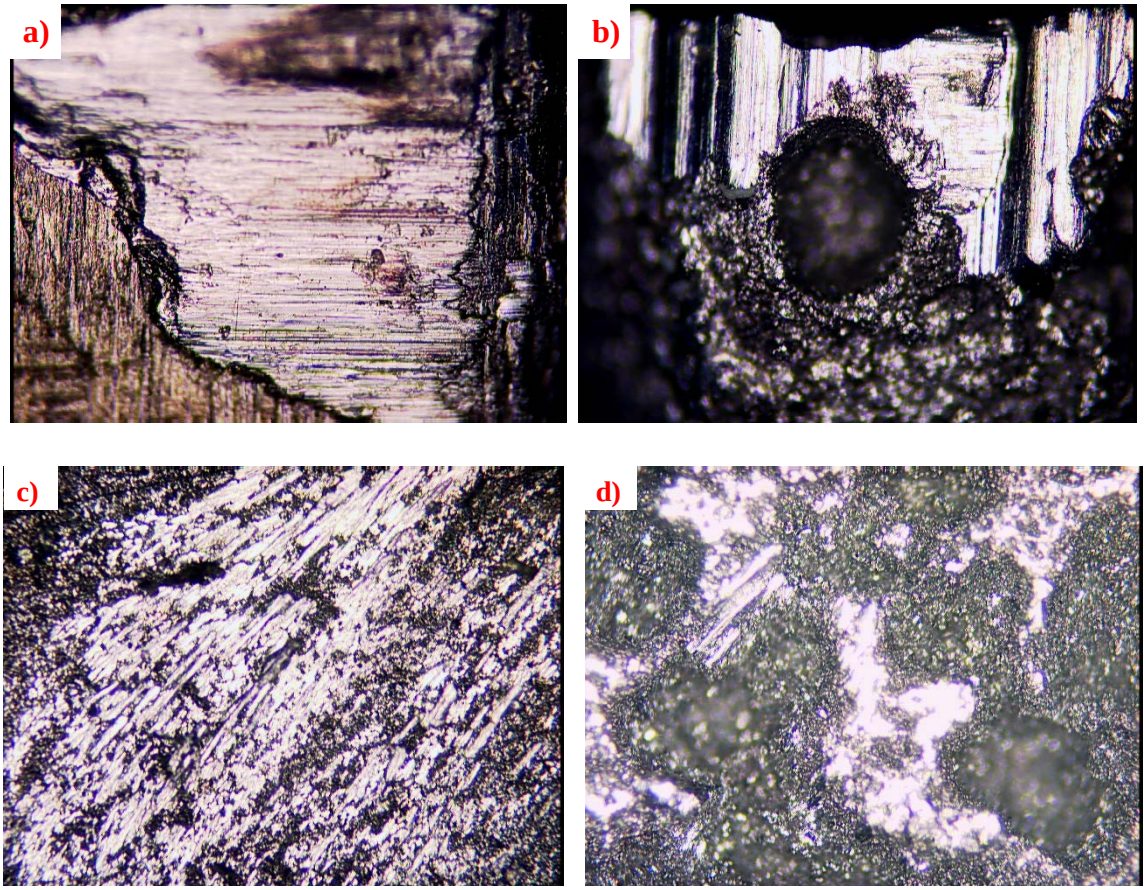

Figure 5.4 Microscope images of flank and crater wear on a) and c) uncoated; b) and d) nanodiamond doped tools

3. Conclusions

Nanodiamond coated carbide insert tools was processed via laser shock wave sintering and tool wear test was carried out to investigate final product performance. Experimental results showed that compared with untreated carbide tools, the wear resistance for nanodiamond coated one improved much better. Upon tool wear test process, the adhesion and material dissolution was stopped by diamond reinforcement phase.

CHAPTER 6. SUMMARY AND DISSCUSSION

In this experimental study, laser shock wave induced freeform technique for sintering high performance and cost-effective diamond micro-tools was investigated. Several analytical tools were utilized including SEM and TEM imaging of the nanodiamond powder and tools product microstructure evolution; XRD and micro-Raman surface analysis to uncover the phase transition during sintering process, hardness and tool wear test to investigate the final performance. Moreover, systematic multi-scale modeling was employed to explore the physics underlying the laser shock wave sintering process and optimize the fabrication process. Based on the result of the parametric study, the following conclusion can be drawn.

1. Nanodiamond micro-tools manufacturing based on laser shock wave can be achieved, both designed additive manufacturing process via layer-by-layer buildup of nanodiamonds in freeform and subtractive manufacturing process by coating nanodiamonds in PcBN or hard carbide tools were verified.

2. Phase purification, refined microstructure and densification, residual stress drive, micro-hardness increase were induced by laser shock wave sintering.

3. Better performance including extreme higher hardness and wear resistance was verified by micro/nano-indentation test and tool wear test.

CHAPTER 7. FUTURE WORK

Laser shock wave induced freeform technique for manufacturing of diamond microtools had proven to be successful. Further investigation of the effect of SWIFT on nanodiamond powders must be conducted to further validate its applications to create high density tools. Listed below is the future work for continuation of this project.

1. Instead of a two-step process that combining thermal process after laser shock wave sintering, redesign a process which can employ CO^2 laser and Nd: YAG laser together to support thermal and mechanical force to sinter nanodiamond powders simultaneously.

2. To minimize porosity and improve densification of final diamond tools, more binders and catalyst can be explored for this sintering process.

3. Stress and strain measurements of the samples to compare with model results.

REFERENCES

1. A. Kobayashi, The Features and Application of UPC Nano-Micro Forming Tools, Industrial Diamond Review (2005) 28-30

2. F. Bruno, C. Friedrich, R.O. Warrington, The Miniturization Technologies: Past, Present, and Future, IEEE Transactions on Industrial Electronics 42 (5) (1995) 423-430

3. R.E. Williams, Y. Huang, S. Melkote, B. Kinsey,W. Sun, D. Yao, Recent Advances in Micro/mesoscale Manufacturing Processes, International Mechanical Engineering Congress and Exposition, Orlando, FL, November 5-11, 2005, ICMECE2005-79889

4. X. Liu, R.E. Devor, S.G. Kapoor, K.F. Ehmann, The Mechanics of Machining at the Microscale:Assessment of the Current State of the Science, Journal of Manufacturing Science and Engineering 126 (4) (2004) 666-678

5. J. Chae, S.S. Park, T. Freiheit, Investigation of micro-cutting operations, International Journal of Machine Tools & Manufacture 46 (2006) 313-332

6. B.N. Damazo, M.A. Davies, B.S. Dutterer, M.D. Kennedy, A Summary of Micro-Milling Studies, 1st International Conference and General Meeting of the European Society of Precision Engineering and Nanotechnology, Bremen, (1999) 322-325

7. C.J. Kim, M. Bono, J. Ni, Experimental Analysis of Chip Formation in Micro-Milling, Technical Paper Society of Manufacturing Engineers MR02-159 (2002)

8. C. Friedrich, P. Coane, J. Goettert, N. Gopinathan, Direct Fabrication of Deep X-Ray Lithography Masks by Micromechanical Milling, Precision Engineering 22 (1998) 164-173

9. Y. Jeon, F.E. Pfefferkorn, Laser-Assisted Machining of Silicon Nitride with Cubic Boron Nitride Tipped Micro End Mill, 2nd International Conference on Micro-Manufacturing USA, Greenville, South Carolina, USA, (2007) 43

10. Q.L. Zhao, G. Yu, T. Sun, S. Dong, Precision Machining of Silicon Carbide with Diamond Micro Tool Array, Key Engineering Materials 364-366 (2007) 321-326

11. C. Chang, Y. Liao, G.Z. Wang, Y.R. Ma, R.C. Fang, CVD Diamond Growth, in: Crystal Growth Technology, Springer, Heidelberg, 2003

12. M.J. Jackson, M.D.H. Gill, H. Sein, W. Ahmed, Manufacture of diamond-coated cutting tools for micromachining applications, Proceedings of I Mech E Part L: Journal of Materials: Design and Applications 217(1) (2003) 77-83

13. H. Sein, W. Ahmed, M. Jackson, R. Woodwards, R. Polini, Performance and characterization of CVD diamond coated, sintered diamond and WC/Co cutting tools for dental and micromachining applications, Thin Solid Films 447-448 (2004) 455-461

14. J. Schwarz, K. Meteva, A. Grigat, A. Schubnov, S. Metev, F. Vollersten, Synthesis of diamond coatings on tungsten carbide with photonplasmatron, Diamond and Related Materials 14(3-7) (2005) 302-307

15. H.Y. Ueng, C.T. Guo, Diamond-like carbon coatings on microdrill using an ECR-CVD system, Applied Surface Science 249 (1-4) (2005) 246-256

16. M.J. Jackson, L.J. Hyde, W. Ahmed, H. Sein, R.P. Flaxman, Diamond-Coated Cutting Tools for Biomedical Applications, Journal of Materials Engineering and Performance 13(4) (2004) 421-430

17. J. Gäbler, Chemical vapour deposition diamond coated microtools for grinding, milling and drilling, Diamond and Related Materials, 9(3-6) (2000) 921-924

18. M.J. Jackson, G.M. Robinson, W. Ahmed, Micromachining selected metals using diamond coated cutting tools, International Journal of Nanomanufacturing 1 (2) (2006) 304-317

19. M. J. Jackson and W. Ahmed, Fabrication and wear of nitrogen-doped diamond microtools, International Journal of Nanomanufacturing, 1(2) (2007) 430-453

20. J. Hu, Y.K. Chou, R.G. Thompson, J. Burgess, S. Street, Characterizations of Nanocrystalline Diamond Coated Cutting Tools, Surface &Coatings Technology 202 (4-7) (2007) 1113-1117

21. V. Vohra, S.A. Catledge, Y.K. Vohra, Effect of surface treatments on the structural and mechanical properties of nanostructured diamond coatings on tungsten carbide cutting tools, Mechanical Propeerties of Nanostructured Materials and Nanocomposites Symposium, Boston, MA, Dec. 1-5 (2003) 277-288

22. O. A. Williams, M. Nesladek, Growth and properties of nanocrystalline diamond films, Physica Status Solidi A 203(13) (2006) 3375-3386

23. J. Hird, J. Field, Diamond polishing, Proceedings of the Royal Society of London, Mathematical, Physical and Engineering Sciences A 460(2052) (2004) 3547-68

24. S.Shabouk and T. Nakamoto, Micromachining of single crystal diamond by utilization of tool wear during cutting process of ferrous material, Journal of Micromechatronics 2(1) (2002) 12-26

25. C. Everson, P. Molian, Fabrication of polycrystalline diamond microtool using a Q-switched Nd:YAG laser, Int J Adv Manuf Technol 45 (2009) 521-530

26. Y. Dong, H. Sakata, P. Molian, Femtosecond pulsed laser ablation of diamond-like carbon films on silicon, Applied Surface Science 252(2) (2005) 352-357

27. D. Ramanathan and P. A. Molian, Micro- and nanomachining of Type IIa single crystal diamond using a Ti:Sapphire femtosecond laser, ASME Journal of Manufacturing Science and Engineering 24(2) (2002) 389-397

28. C. Z. Wang, K.M. Ho, M.D. Shirk and P.A. Molian, Laser-Induced graphitization on a diamond (111) surface, Physical Review 85(19) (2000) 4092-4095

29. A. M. Ozkan, A.P. Malshe, T.A. Railkar, W.D.Brown, M.D. Shirk, and P.A. Molian, Femtosecond laser-induced periodic structure writing on diamond crystals and microclusters, Applied Physics Letters 75(23) (1999) 3716-3718

30. M.D. Shirk, P. A. Molian and A. P. Malshe, Ultrashort pulsed laser ablation of diamond, Journal of Laser Applications 10(2) (1998) 64-70

31. R. Windholz and P. A. Molian, Nanosecond pulsed excimer laser machining of CVD diamond and graphite, Part II: Analysis and Modeling, Journal of Materials Science 33 (1998) 523-528

32. R. Windholz and P. A. Molian, Nanosecond pulsed excimer laser machining of CVD diamond and HOPG graphite, Part I: Experimental Study, Journal of Materials Science 32 (1997) 4295-4301

33. C.J. Morgan, R. Vallance and E. Marsh, Micromachining glass with polycrystalline diamond tools shaped by micro electro discharge machining, Journal of Micromechanics and Microengineering 14 (2004) 1687-1692

34. C. J. Morgan, R. Vallance and E. Marsh, Micro-machining and micro-grinding with tools fabricated by micro electro-discharge machining, International Journal of Nanomanufacturing 1(2) (2006) 242-258

35. J. Hung, S. Lien, J. Lin, F. Huang and B. Yan, Fabrication of a micro-spherical tool in EDM combined with Ni-diamond co-deposition, Journal of Micromechanics and Microengineering 18 (2008)

36. S. N. Bhavsar, S. Aravindan, and P. V. Rao, A Critical Review on Microtools fabrication by focused ion beam (FIB) technology, Proceedings of the World Congress on Engineering 2009,Vol II WCE 2009, London, U.K, July 1-3 (2009)

37. S. J. Zhang, F. Z. Fang, Z. W. Xu, and X. T. Hu, Controlled morphology of microtools shaped using focused ion beam milling technique, Journal of Vacuum Science & Technology B: Microelectronics and Nanometer Structures 27(3) (2009) 1304-1309

38. Y. Picard, D. Adams, M. Vasile and M. Ritchey, Focused ion beam-shaped microtools for ultraprecision machining of cylindrical components, Precision Engineering 27 (2003) 59–69

39. E. Ritzhaupt-Kleissl, C. Mu¨ller, A. Sossalla, S. Ertl, P. Gluche, Fabrication of diamond microtools for ultra precision machining, Microsystem Technologies 11 (2005) 278–279

40. P. Peyre, R. Fabbro, Laser shock processing: a review of the physics and applications, Optical and Quantum Electronics 27 (1995) 1213-1229

41. M. Baidakova and A. Vul', New prospects and frontiers of nanodiamond clusters, Journal of Physics D: Applied Physics 40 (2007) 6300-6311

42. A. Schrand, S.A. Ciftan, S. Olga, Nanodiamond Particles: Properties and perspectives for bioapplications, Critical Reviews in Solid State and Material Sciences 34(1-2) (2009) 18-74

43. S. Osswald, A. Gurga, F. Kellogg, K. Cho, G. Yushin and Y. Gogotsi, Plasma pressure compaction of nanodiamond, Diamond and Related Materials 16 (2007) 1967-1973

44. S. Osswald, G. Yushin, V. Mochalin, S. Kucheyev and Y. Gogotosi, Control of sp2/sp3 carbon ratio and surface chemistry of nanodiamond powders by selective oxidation in air, Journal of American Chemical Society 128 (2006) 11635-11642

45. G.N. Yushin, S. Osswald, V.I. Padalko, G.P. Bogatyreva and Y. Gogotsi, Effect of sintering on structure of nanodiamond, Diamond and Related Materials 14(10) (2005) 1721-1729

46. A.C. Ferrari and J. Robertson, Raman spectroscopy of amorphous, nanostructured, diamond-like carbon, and nanodiamond, Philosophical Transactions of the Royal Society A 362 (2004) 2477-2512

47. P. Regenfuss, L. Hartwig, S. Klötzer, R. Ebert, H. Exner, Microparts by a Novel Modification of Selective Laser Sintering, SME Technical paper TP04PUB185 (2004)

48. P. Regenfuss, A. Streek, L. Hartwig, S. Klotzer, Th. Brabant, M. Horn, R. Ebert, H. Exner, Principles of laser micro sintering, Rapid Prototyping Journal 13 (2007) 204-212

49. H. Exner, M. Horn, A. Streek, F. Ullmann, L. Hartwig, P. Regenfuss, R. Ebert, Laser micro sintering: A new method to generate metal and ceramic parts of high resolution with submicrometer powder, Virtual and Physical Prototyping 3(1) (2008) 3-11

50. J. Chen, Jianhua Yang Tiechuan Zuo, Micro fabrication with selective laser micro Sintering; nano/micro engineered and molecular systems, 2006. NEMS '06. 1st IEEE International Conference on, Publication Date: 18-21 Jan. 2006,On page(s): 426-429

51. M. Boustie, L. Berthe, T. de Resseguier, M. arrigoni, Laser shock waves: fundamentals and applications, 1st International Symposium on Laser Ultrasonics: Science, Technology and Applications, Montreal, Canada ,July 16-18 (2008)

52. C. Montross , T.Wei, L. Ye, G. Clark, Y. Mai, Laser shock processing and its effects on microstructure and properties of metal alloys: a review, International Journal of Fatigue 24 (2002) 1021-1036

53. A.W. Warren, Y.B. Guo, S.C. Chen, Massive parallel laser shock peening: Simulation, analysis, and validation, International Journal of Fatigue 30 (2008) 188-197

54. B. Dubrujeaud and M. Jeandin, Cladding by laser shock processing, Journal of Materials Science Letters 13 (1994) 773-775

55. W. Zhang and L. Yao, Microscale laser shock processing of metallic components, Journal of Manufacturing Science and Engineering 124 (2002) 369-378

56. W. Zhang, L. Yao and I. C. Noyan, Microscale laser shock peening of thin films, part 1: Experiment, Modeling and Simulation, Journal of Manufacturing Science and Engineering 126 (2004) 10-17

57. Harrison PM, Henry M, Brownell M, Laser process of diamond, tungsten carbide and related hard materials, Journal of Laser Applications 18(2) (2006) 117-126

58. Harper CA, Handbook of ceramics, glasses and diamonds, McGraw Hill, New York (2001)

59. Bai Q, Yao Y, Chen S, Research and development of polycrystalline diamond woodworking tools, International Journal of Refractory Metals and Hard Materials 20 (2002) 395-400

60. Shin T, Oh J, Oh K, Lee D, The mechanism of abnormal grain growth in polycrystalline diamond during high pressure high temperature sintering, Diamond and Related Materials 13 (2004) 488-494

61. Yoshikawa M, Raman spectra of diamond-like amorphous carbon films, Materials Science Forum 52-53 (1989) 365-386

62. Nemanich R.J, Solin SA, First- and second-order Raman scattering from finite-size crystals of graphite, Physical Review B 20 (1979) 392-401

63. Yoshikawa M, Katagiri G, Ishida H, Akamatsu T, Optical constants of hard carbon thin films: preparation, properties and application, Journal of Applied Physics 64 (1988) 6464

64. Prawer S, Nugent KW, Jamieson DN, Orwa JO, Bursill LA, Peng JL, The Raman spectrum of nanocrystalline diamond, Chemical physic letters 332 (2000) 93-97

65. Ding K, Ye L, Laser shock peening: performance and process simulation, Boca Raton, FL: CRC Press LLC (2006)

66. R. Fabbro, J. Fournier, P. Ballard, D. Devaux, J. Virmont, Physical study of laser-produced plasma in confined geometry, Journal of Applied Physics 68 (1990) 775-784

67. Peyre P, Fabbro R, Merrien P, Lieurade HP, Laser shock processing of aluminum alloys. Application to high cycle fatigue behavior, Materials Science and Engineering: A 210 (1996) 102-113

68. http://www.inficonthinfilmdeposition.com/en/densityandacousticvalues.html, 5/26/2011

69. Berther L, Fabbro R, Peyre P, Tollier L, Bartnicki E, Shock waves from a water-confined laser-generated plasma, Journal of Applied Physics 82 (1997) 2826-2832

70. Berther L, Fabbro R, Peyre P, Tollier L, Bartnicki E, Wavelength dependent laser shock-wave generation in the water-confinement regime, Applied Physics 85 (1999) 7552-7555

71. Devaux D, Fabbro R, Virmont J, Generation of shock waves by laser-induced plasma in confined geometry, Journal of Applied Physics 74 (1993) 2268-2273

72. Sollier A, Berthe L, Fabbro R, Numerical modeling of the transmission of breakdown plasma generated in water during laser shock processing, European Physical Journal Applied Physics 16 (2001) 131-139

73. http://www.chm.bris.ac.uk/motm/diamond/diamprop.htm, 5/26/2011

74. Zhang GF, Zhang B, Deng ZH, Chen JF, CIRP Annals-Manufacturing Technology 56 (2007) 201-204

75. Murr LE, Staudhammer KP, Materials Science Engineering 20 (1975) 35

76. Haubner R, Wilhelm M, Weissenbacher R, Lux B, Boron Nitrides-Properties, Synthesis and Applications, Structure and Bonding 102 (2002) 1-45

77. Solozhenko V, Thermodynamics of dense boron nitride modifications and a new phase P,T diagram for BN, Thermochimica Acta 218 (1993) 221–227

78. Zhang J, Yu Q, Pang S, Meng S, Wang T, Hu J, Development and application of polycrystal cubic boron nitride cutting tool material, Key Engineering Materials 375-376 (2008) 168-171

79. Kurt A, S_eker U, The effect of chamfer angle of polycrystalline cubic boron nitride cutting tool on the cutting forces and the tool stresses in finishing hard turning of AISI 52100 steel, Materials & Design 26(4) (2005) 351-356

80. Sechi Y, Tsumura T, Nakata K, Dissimilar laser brazing of boron nitride and tungsten carbide, Materials & Design 31(4) (2010) 2071-2077

81. Bhaumil SK, Divakar C, Singh AK, Machining Ti-6Al-4V alloy with a wBN-cBN composite tool, Materials & Design 16(4) (1995) 221-226

82. Jack DH, Ceramic cutting tool materials, Materials & Design 7(5) (1986) 267-273

83. Casanova C, Balzaretti A, Voronin G, Jornada J, Experimental study of plastic deformation during sintering of cubic boron nitride compacts, Diamond and Related Materials 8 (1999) 1451–1454

84. Novikov NV, Bondarenko VP, Kocherzhinskii YA, A study of plastic deformation of cubic boron nitride, Journal of Superhard Materials 2 (1985) 17-20

85. Shulzhenko AA, Bozhko SA, Sokolov AN, Synthesis sintering and properties of cubic boron nitride, Naukova Dumka; Kiev (1993) 255

86. Vel L, Demazeau G, Etourneau J, Cubic boron nitride: synthesis, physicochemical properties and applications, Materials Science and Engineering B 10(2) (1991) 149-164

87. http://www.cuttingtool.americanmachinist.com/guiEdits/Content/bdeee1/bdeee1_1.asp x 2011[accessed 05.08.11]

88. Cook M, Bossom P, Trends and recent developments in the material manufacture and cutting tool application of polycrystalline diamond and polycrystalline cubic boron nitride, International Journal of Refractory Metals and Hard Materials 18 (2000) 147-152

89. Montross S, Wei T, Ye L, Clark G, Mai Y, Laser shock and its effects on microtructure and properties of metal alloys: a review, International Journal of Fatigue 24 (2002) 1021-1036

90. Peyre P, Fabbro R, Berthe L, Dubouchet C, Laser shock processing of materials, physical processes involved and examples of applications, Journal of Laser Applications 8 (1996) 135-141

91. Yucheng Z, Mingzhi W, Preparation of polycrystalline cBN containing nanodiamond, Journal of Materials Processing Technology 198 (2008) 134–138

92. Y.M. Chong, K.L. Ma, K.M. Leung, C.Y. Chen, Q. Ye, I. Bello, W.J. Zhang and S.T. Lee, Synthesis and mechanical properties of cubic born nitride/diamond thin films, Chemical Vapor Deposition 12 (2006) 33-41

93. Benko E, Stanislaw J, Krolicka B, Wyczesany A, Barr T, CBN-TiN, Cbn-TiC composites:chemical equilibria, microstructure and hardness mechanical investigations. Diamond and Related Materials 8 (1999) 1838-1846

94. Ronga X, Tsurumi, Fukunagab O, Yanoa T, High-pressure sintering of cBN-TiN-Al composite for cutting tool application, Diamond and Related Materials 11(2) (2002) 280-286

95. Erasmus R.M, Comins J.D, Fish M.L, Raman and photoluminescence spectra of indented cubic boron nitride and polycrystalline cubic boron nitride, Diamond and Related Materials 9 (2000) 600-604

96. Bergman L, Nemanich R.J, Raman Spectroscopy Characterization of hard, wide-bandgap for Semiconductors: Diamond, GaN, GaAlN, AlN, BN, Annual Review of Materials Research 26 (1996) 551-579

97. Sachdev H, Influence of impurities on the morphology and Raman spectra of cubic boron nitride, Diamond and Related Materials 12 (2003) 1275-1286

98. Zinin P.V, Kudryashov I, Konishi N, Ming L.C, Solozhenko V.L, Sharma S.K, Identification of the diamond-like B-C phase by confocal Raman spectroscopy, Spectrochimica Acta Part A 61 (2005) 2386-2389

99. Olszyna A, Konwerska-Hrabowska J, Lisicki M, Molecular structure of E-BN, Diamond and Related Materials 6 (1997) 617-620

100. Sanjurjo JA, Lopez-Cruz E, Vogal P, Cardona M, Dependence on volume of the phonon frequencies and their effective charges of several III-V semiconductors, Physical Review B 28 (1983) 4579-4584

101. http://www.nanodiamond.com.ua/NANO.HTM; 2011 [accessed 05.08.11]

102. Osipov A, Nauyoks S, Zerda T, Zaporozhets O, Rapid sintering of nano-diamond compacts, Diamond and Related Materials 18 (2009) 1061-1064

103. Sun K.W, Wang J.Y, Ko T.Y, Raman spectroscopy of single nanodiamond: Phonon-confinement effects, Applied Physics Letters 92 (2008) 15-18

104. Zhi C.Y, Bai X.D, Wang E.G, Raman characterization of boron carbonitride nanotubes, Applied Physics Letters 80 (2002) 19-22

105. Ci L, Song L, Jin C, Jariwala D, Wu D, Li Y, Srivastava A, Wang Z, Storr K, Balicas L, Liu F, Ajayan P, Atomic layers of hybridized boron nitride and graphene domains, Nature Materials 9 (2010) 430-435

106. Kuhlmann U, Werheit H, Raman effect of boron carbide (B4.3C to B10.37C), Journal of Alloys and Compounds 205 (1994) 87-91

107. Nistor L, Buschmann V, Ralchenko V, Dinca G, Vlasov I, Van Landuyt J, et al. Microstructure characterization of diamond films deposited on c-BN crystals, Diamond and Related Materials 9 (2000) 269-273

108. T. Irifune, A. Kurio, S. Sakamoto, T. Inoue, H. Sumiya, Materials: Ultrahard polycrystalline diamond from graphite, Nature 421 (2003) 599-600

109. W. Braisted, R. Brockman, Finite element simulation of laser shock peening, Int. J. Fatigue, 21 (1999) 719-724.

110. A.F.M. Arif, Numerical prediction of plastic deformation and residual stresses induced by laser shock processing, Journal of Materials Processing Technology 136 (2003) 120-138

111. K. Ding, L. Ye, Simulation of multiple laser shock peening of a 35CD4 steel alloy, Journal of Materials Processing Technology 178 (2006) 162-169

112. F. Cardarelli, Materials Handbook, Springer, London, New York (1999)

113. J.T. Luxon, D.E. Parker, Industrial lasers and Their Applications, Prentice-Hall, Englewood Cliffs, New Jersey (1992)

114. T. Thorslund, Mathematical models for temperatures, pressures and stresses during shock processing by utilization of a laser source, M. S. Thesis, University of Uppsala, Sweden, 1996

115. K. Kawakita, Some considerations on powder compression equations, Powder Technology 4 (1971) 61-68

116. Dassault systemes, Critical state (clay) plasticity model, in: Abaqus Analysis User's Manual-version 6.11, 2011

117. F. Dimaggio, I. Sandler, Material model for granular soils, Journal of the Engineering Mechanics Division 97 (1971) 935–950

118. I.S. Sandler, D. Rubin, An algorithm and a modular subroutine for the cap model, International Journal for Numerical and Analytical Methods in Geomechanics 3 (1979) 173-186

119. I.C. Sinka, J.C. Cunningham, A. Zavaliangos, The effect of wall friction in the compaction of pharmaceutical tablets with curved faces: a validation study of the Drucker-Prager cap model, Powder Technology 133 (2003) 33-43

120. P.R. Brewin, O. Coube, P. Doremus, J.H. Tweed, Modelling of powder die compaction, London, 2008

121. C.Y. Wu, O.M. Ruddy, A.C. Bentham, B.C. Hancock, S.M. Best, J.A. Elliott, Modelling the mechanical behavior of pharmaceutical powders during compaction, Powder Technology 152 (2005) 107-117

122. A. Michrafy, D. Ringenbacher, P. Techoreloff, Modelling the compaction behavior of powders: application to pharmaceutical powders, Powder Technology 127 (2002) 257-266

123. M. Henke, U. Klemm, D. Sobek, Determination of specific parameters in dry pressing of ceramic powders, Journal of Powder and Bulk Solids Technology 10 (1986) 9-14

124. D. Falgon, E. Vidal-Salle´, J-C Boyer, R. Peczalski, J. Andrieu, Identification procedure of a hardening law for powder compaction, Powder Technology 157 (2005) 183-90

125. J.L. Ocan˜a, M. Morales, C. Molpeceres, J. Torres, Numerical simulation of surface deformation and residual stresses field in laser shock processing experiments, Applied Surface Science 238 (2004) 242-248

126. P. Peyre, A. Sollier, I. Chaieb, L. Berthe, E. Bartnicki, C. Braham and R. Fabbro, FEM simulation of residual stresses induced by laser peening, The European Physical Journal Applied Physics 23 (2003) 83-88

127. K. McLaughlin, I.I. Oleynik, S.V. Zybin, M.L. Elert, C.T. White, Molecular dynamics simulations of an anomalous response of diamond to shock compression, Shock Compression of Condensed Materials CP955 (2007) 321-324

128. V.V. Danilenko, Shock-induced melting of diamond powders, Combustion Explosion and Shock Waves 45 (2009) 744-751

129. I. Aydin, B.J. Briscoe, N. O¨zkan, Modelling of powder compaction: a review, MRS Bulletin 22 (1997) 45-51

130. F. Li, V.M. Puri, Mechanical behaviour of powders using a medium pressure flexible boundary cubical triaxial tester, Journal of Process Mechanical Engineering 217 (2003) 233-241

131. H. Chtourou, M. Guillot and A. Gakwaya, Modeling of the metal powder compaction process using the cap model Part I Experimental material characterization and validation, International Journal of Solids and Structures 39 (2002) 1059-1075

132. L. Xiao, Numerical Computation of Stress Waves in Solids, Berlin (1996)

133. I. Varghese, D. Zhou, M.D. Murthy Peri and C. Cetinkaya, Thermal loading of laser induced plasma shockwaves on thin films in nanoparticle removal, Journal of Applied Physics 101, 113106 (2007)

134. M.D. Murthy Peri, D. Zhou, I. Varghese and C. Cetinkaya, Transient Thermo-Elastic response of nanofilms under radiation heating from pulsed laser induced plasma, IEEE Transactions on Semiconductor Manufacturing 21(1) (2008)

135. Z. Shi, X.Feng, Y. Huang, J. Xiao and K.C. Hwang, The equivalent axisymmetric model for Berkovich indenters in power-law hardening materials, International Journal of Plasticity 26 (2010) 141-148

136. A.C. Ferrari, J. Robertson, Raman spectroscopy of amorphous, nanostructured, diamond-like carbon, and nanodiamond, Philosophical Transactions of the Royal Society of London 362 (2004) 2477-2512

137. S. K. Jerng et al. Nanocrystalline Graphite Growth on Sapphire by Carbon Molecular Beam Epitaxy, Journal of Physical Chemistry C 115 (2011) 4491-4494